



Technische Universität München

Fakultät für Mathematik
Lehrstuhl M2 - Fachgebiet Numerische Mathematik (Prof. Wohlmuth)

Non-isothermal, Multi-phase, Multi-component Flows through Deformable Methane Hydrate Reservoirs

Shubhangi Gupta

Vollständiger Abdruck der von der Fakultät für Mathematik der Technischen Universität München zur Erlangung des akademischen Grades eines

Doktors der Naturwissenschaften (Dr. rer. nat.)

genehmigten Dissertation.

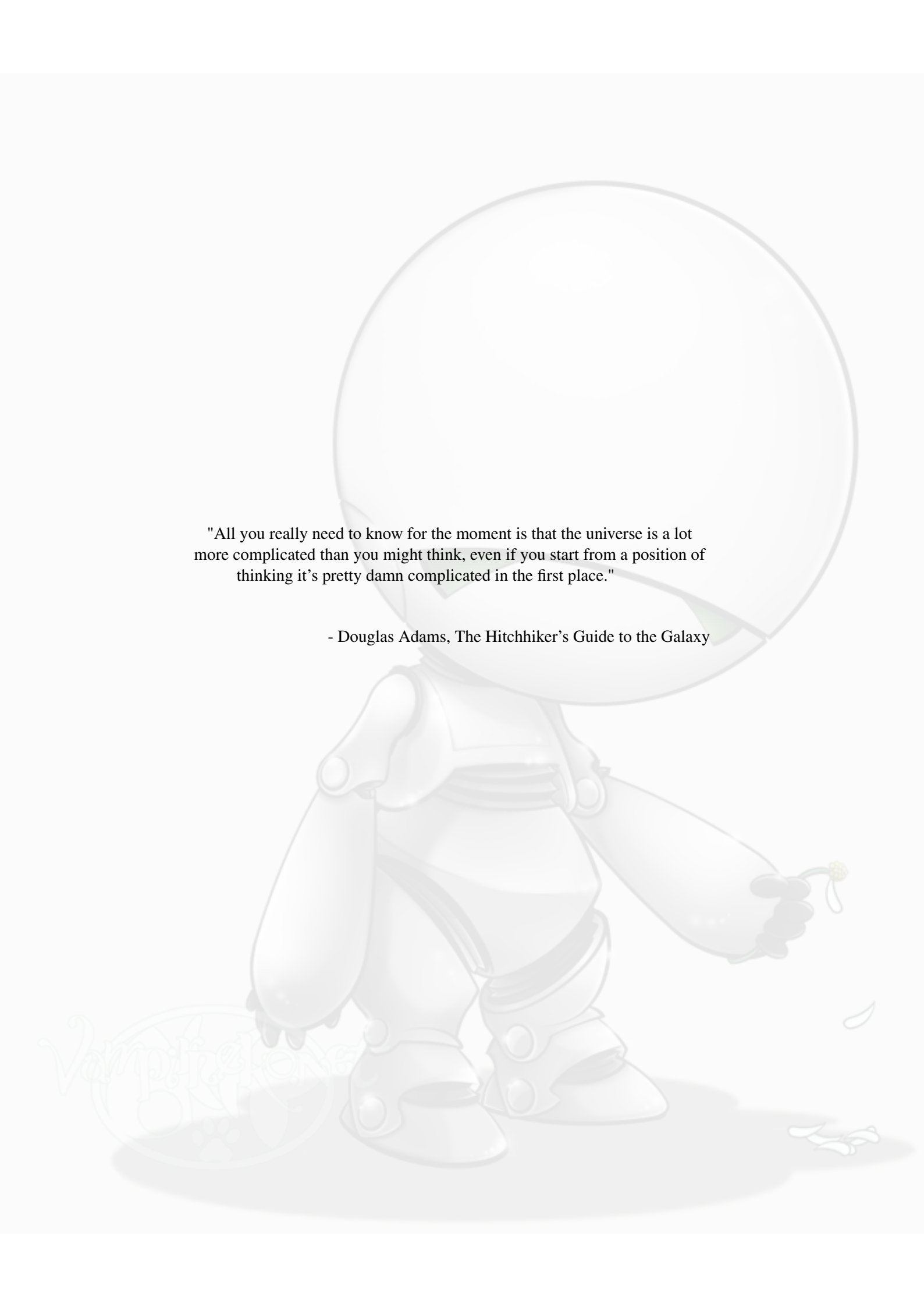
Vorsitzender: Univ.-Prof. Dr. Martin Brokate

Prüfer der Dissertation:

1. Univ.-Prof. Dr. Barbara Wohlmuth
2. Univ.-Prof. Dr. Iuliu Sorin Pop, Universiteit Hasselt, Belgien

Die Dissertation wurde am 20 · 01 · 2016 bei der Technischen Universität München eingereicht und durch die Fakultät für Mathematik am 14 · 04 · 2016 angenommen.

Dedicated to my husband, Stefan Karpinski



"All you really need to know for the moment is that the universe is a lot more complicated than you might think, even if you start from a position of thinking it's pretty damn complicated in the first place."

- Douglas Adams, *The Hitchhiker's Guide to the Galaxy*

Acknowledgements

I am extremely grateful to my PhD. advisors, Prof. Dr. Barbara Wohlmuth and Prof. Dr. Rainer Helmig, for taking me under their wings. Their expert guidance, support, and constant encouragement throughout my doctoral research gave me the confidence to complete this thesis successfully.

I am ever grateful to Dr. Christian Deusner from GEOMAR, Kiel, for his support with the experimental data, and for his insightful suggestions and countless discussions which have gone a long way in shaping my understanding of the methane hydrate systems. I look forward to our continued collaboration. I also remain grateful to Prof. Dr. Matthias Haeckel for giving me critical modelling and engineering advices from time to time, which have greatly advanced my understanding of the subject.

I thank Mrs. Lydia Weber for her help with the administrative issues related with my thesis.

I thank my husband for being my pillar of strength, and for giving me the courage to face the monsters of insecurity and self doubt, which come attached with the open-ended nature of any academic problem. Every time the going got tough, I found him by my side. I am certain that I would not have made it this far without his love and support.

I take this opportunity to also thank my father for being my first mathematics and physics teacher. I can proudly claim that I owe my love for science and the drive to pursue academics to the countless hours he has devoted to my education. The older I grow, the more I realise the sacrifices he has made in terms of time and resources for my education. Thanks also to my mother for teaching me the virtues of humility in the pursuit of excellence. Thanks to my brother, Ritank, for teaching me how to bounce back and turn set backs into stepping stones. I have learnt many things growing up with him. *Resilience* is one of them.

Abstract

In this thesis, we present a multiphysics model and numerical solution framework for subsurface methane hydrate systems. The focus of the model development is laid on application to natural gas production through depressurization and thermal stimulation methods. The model considers kinetic hydrate phase change and non-isothermal, multi-phase, multi-component flow in linear-elastically deforming soils, and accounts for the dynamic effects on the mechanical and the fluid-solid interaction properties occurring due to the chemo-hydro-geo-mechanical coupling. We develop numerical solution strategies for this model and validate against several benchmark tests, analytical solutions, and experimental data.

Zusammenfassung

Wir präsentieren ein Multiphysik-Modell und eine numerische Lösungsmethode für unterirdische Methanhydrat Systeme. Der Fokus des Modells liegt auf Erdgasförderung durch Reduktion des Druck oder thermische Stimulation. Das Modell berücksichtigt kinetische Phasenänderung des Hydrats und nicht-isotherme Mehrphasen-Mehrkomponenten-Strömung in linearelastisch verformbaren Böden. Die dynamischen Auswirkungen der chemo-hydro-geo-mechanische Kopplung auf die mechanischen und hydraulischen Eigenschaften des Hydrats werden ebenso mit einbezogen. Wir entwickeln numerische Lösungsstrategien für dieses Modell, und validieren diese gegen verschiedene Standardtests, analytische Lösungen, und experimentell ermittelte Messungen.

Contents

1	Introduction	1
2	Mathematical model	7
2.1	Macroscopic continuum	7
2.2	Model concept	10
2.3	Governing equations	11
2.4	Constitutive relationships	13
2.4.1	Vapor-liquid equilibrium	13
2.4.2	Fick’s law for diffusive mass-transfer flux	14
2.4.3	Properties of the fluid-matrix interaction	14
2.4.4	Hydrate phase change kinetics	16
2.4.5	Poro-elasticity	18
3	Numerical solution strategy	21
3.1	Discretization schemes	23
3.1.1	Space discretization: Finite volume method	23
3.1.2	Space discretization: Finite element method	28
3.1.3	Time discretization: Implicit Euler method	32
3.2	Iterative block Gauss-Seidel scheme	33
3.3	Multi-rate time stepping scheme	35
4	Model verification	39
4.1	Test 1: Dissociation kinetics model	40
4.1.1	1D experiment	40
4.1.2	2D experiment	42
4.2	Test 2: Coupled three-phase hydrate model	45
4.3	Test 3: Poroelasticity coupling	49
4.4	Test 4: Kinetics-poroelasticity coupling	52

5	Performance evaluation of the MRT methods	61
5.1	Test problem	61
5.2	Numerical simulation	63
5.3	Results	64
5.3.1	Semi-implicit MRT method	64
5.3.2	Compound-fast MRT method	68
5.4	Discussion	69
5.4.1	Semi-implicit MRT method	69
5.4.2	Compound-fast MRT method	71
6	Numerical study of a 3D hydrate reservoir problem	73
6.1	Test setting	73
6.2	Numerical simulation and results	76
6.3	Numerical solution using multirate time stepping	77
7	Model verification using triaxial compression lab experiments	79
7.1	Materials and methods	80
7.1.1	Experimental set-up and components	80
7.1.2	Sample preparation and mounting	80
7.1.3	Experimental procedure	81
7.2	Numerical simulation	82
7.2.1	Computational domain and test-setting	82
7.2.2	Simulation results	88
7.3	Discussion	92
8	Outlook	95
	Appendices	99
A	Derivation of storage Eqn. (4.6)	99
B	Analytical solution for the Initial-Boundary-Value Problem (4.13)	103
	List of Figures	105
	List of Tables	107
	Bibliography	109

Introduction

Methane hydrates are crystalline solids formed when water molecules form a cage-like structure and trap a large number of methane molecules within. Methane hydrates are thermodynamically stable under conditions of low temperature and high pressure and occur naturally in permafrost regions or sub-seafloor soils. If warmed or depressurized, methane hydrates destabilize and dissociate into water and methane gas. Natural gas hydrates are considered to be a promising energy resource. It is widely believed that the energy content of methane occurring in hydrate form is immense, possibly even exceeding the combined energy content of all other conventional fossil fuels (Pinero 2013 [74], Burwicz et al. 2011 [17], Archer et al. 2009 [6], Milkov 2004 [57], Kvenfolden 1993 [51]).

Several methods have been proposed for production of natural gas from gas hydrate reservoirs through thermal stimulation, depressurization or chemical activation (Moridis et al. 2009, 2011 [61, 62], Park et al. 2006 [71], Lee et al. 2003 [52]). Refer Fig. 1.1. Currently, depressurization is considered as the most mature approach, and therefore, there is a strong focus on evaluating the potential for using depressurization as the essential driving force for releasing gas from natural gas hydrate reservoirs. Recent field trials, onshore in the Alaska permafrost and in the Nankai Trough offshore Japan, were essentially depressurization tests; the Japanese test used only depressurization (Yamamoto 2013, 2015 [114, 115], David 2013 [23]), while, the Alaska test was combined with $N_2:CO_2$ injection and CH_4-CO_2 -hydrate exchange (Anderson et al. 2014 [4], Schoderbek et al. 2013 [93]).

Several mathematical models have been proposed (e.g. Tsypkin [105], Ahmadi et al. [2], Yousif et al. [117], Sun and Mohanty [101], Liu and Flemmings [55], Moridis [60, 63]) and different numerical simulators have been developed (e.g. MH21-HYDRES [49], STOMP-HYD [111], UMSICHT HyRes [42], TOUGH-HYDRATE [64]) for simulating hydrate reservoirs and evaluating the performance of the various gas production methods. These models and simulators consider mainly hydrate phase change and fluid flow while neglecting the geomechanical effects.

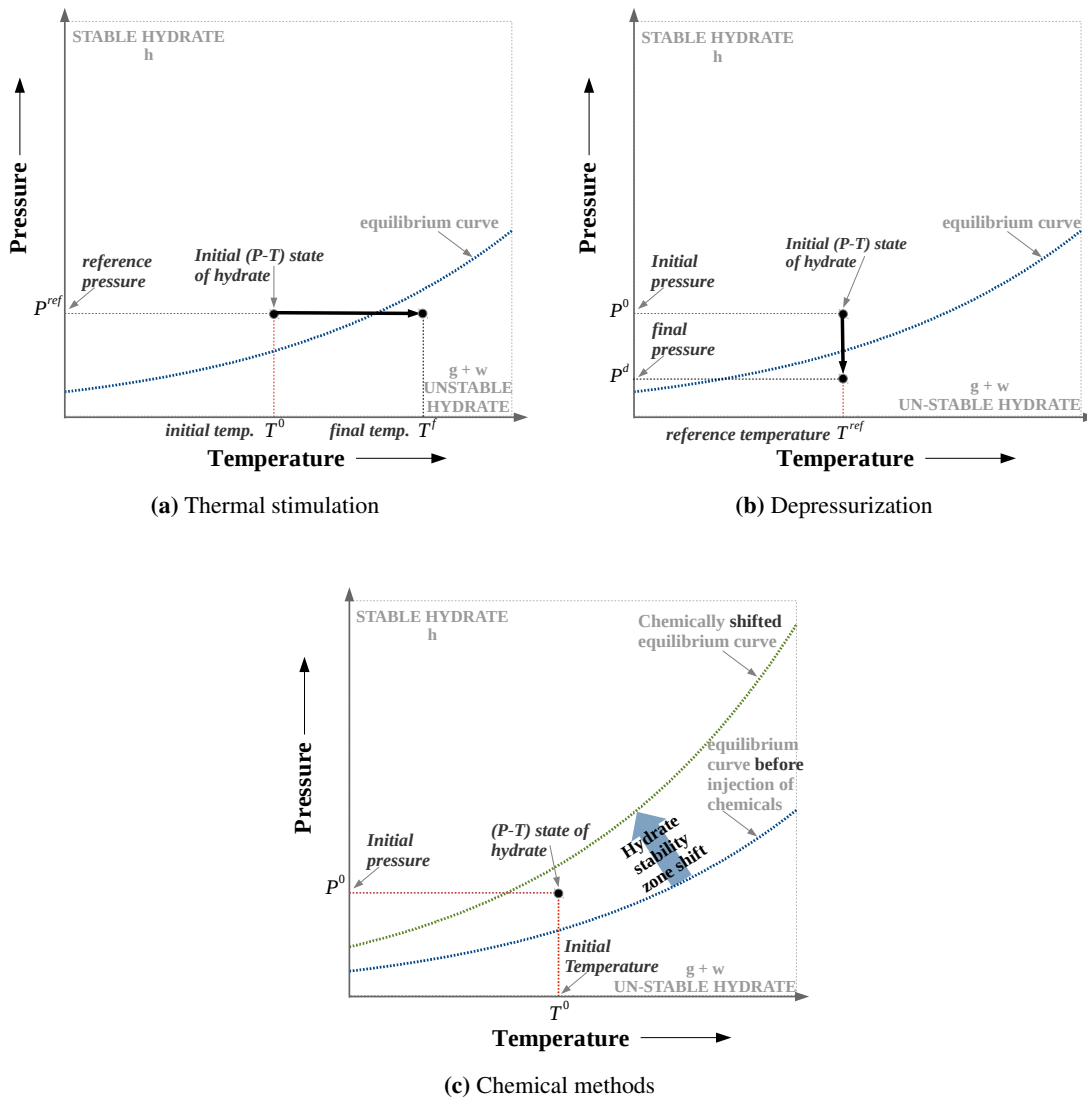


Figure 1.1: Gas production methods from methane hydrates.

a) *Thermal Stimulation*: Hydrate formation is heated at constant pressure through the injection of hot fluid or potentially, through direct heating of the formation. Thermal stimulation is energy intensive and leads to relatively slow, conduction-limited dissociation of the gas hydrates unless warmer pore fluids become mobilized and increase the volume of the formation exposed to higher temperature. The endothermic nature of hydrate dissociation presents additional challenge to thermal stimulation.

b) *Depressurization*: The hydrate formation is exposed to low pressure while maintaining the formation temperature constant, usually by pumping out the free gas. This method is inherently less energy intensive as no heating is involved.

c) *Chemical methods*: Injection of certain chemical compounds can shift the hydrate equilibrium curve and destabilize the methane hydrates present in the formation. *Chemical Inhibition* exploits the fact that methane hydrate stability is inhibited in the presence of certain organic (e.g., glycol) or ionic (e.g., seawater or brine) compounds. *Chemical substitution* involves the substitution of methane gas in the hydrate lattice by another gas (e.g., carbon dioxide), whose hydrate is energetically more favourable as compared to methane hydrate. In laboratory, injected carbon dioxide has been shown to replace the methane in the gas hydrate lattice without measurable dissociation of the gas hydrate [28, 52].

It has been widely recognized in the hydrate community that the destabilization of hydrates can cause significant consolidation, ground deformation, and other soil stability issues. Several mathematical models have also been proposed to extend the above mentioned hydrate-reservoir model concepts to include geo-mechanics (e.g. Rutqvist and Moridis [82], Kimoto et al. [46]). Rutqvist and Moridis [82] have coupled TOUGH-HYDRATE with the commercial geomechanical code FLAC^{3D} [34] to investigate the hydro-geomechanical behaviour of hydrate reservoirs. Kimoto et al. [46] have developed their own chemo-thermo-hydro-mechanical simulator. Their simulator uses an elasto viscoplastic model to simulate deformation. Several simulation studies have been performed to predict the effect of gas hydrate dissociation and fluid flow on the soil stability (e.g., Ning et al. 2012 [68], Rutqvist et al. 2009, 2012 [83, 84], Klar et al. 2010 [47], Hyodo et al. 2014 [39]). However, the nature and extent of the geotechnical problems actually observed during the field trials were beyond predictions, and the sediment destabilization and sand production could not be sufficiently controlled. Because of these apparent process management and safety concerns it is important to carefully evaluate future technologies for gas extraction from gas hydrate reservoirs and to include detailed risk quantification from inherent geohazards in the particular situation and setting.

Multiphysics models and numerical codes for strongly coupled hydro-thermo-chemo-geo-mechanical processes have, over the years, become a very powerful and indispensable tool for making such performance evaluations at relatively low costs, although computing power necessary for detailed field scale modeling can be huge (Reagan 2015 [77]). The predictive value of numerical models depends on their ability to capture the influence of important variables such as gas hydrate saturation and distribution in relation to soil characteristics, as well as to describe how this behavior changes when gas hydrate-soil fabrics are dynamically altered during and after gas production. Thus, to be able to make any predictions with confidence, the numerical models need to be thoroughly validated against experimental data.

Numerous experimental studies on mechanical behavior of gas hydrate-bearing soils have been carried out in the past. Small-strain mechanical properties such as P- and S-wave velocities of gas hydrate bearing soils with various soil types and gas hydrate saturations have been evaluated to calibrate field geophysical exploration procedures, and to allow prediction of small strain strength and stiffness, volume yield behavior and subsidence upon changes in gas hydrate saturation and gas hydrate-soil fabrics under defined stress conditions (Winters et al. 2007 [112], Lee et al. 2010 1/2 [54], Priest et al. 2005, 2009 [75, 76]). It is generally agreed on that the distribution of gas hydrates and the gas hydrate-soil skeleton has marked influence on strength and stiffness behavior, such that cementing gas hydrates increase stiffness and strength already at low gas hydrate saturations whereas pore filling gas hydrates only become effective at higher gas hydrate saturations ($\approx 0.4 - 0.5$) (Waite et al. 2009 [110]). Material models were frequently obtained using THF to allow for fast and controlled gas hydrate formation in the laboratory without necessity of having a free gas phase and more complicated volume change behavior (Lee et al. 2010 [54], Yun et al. 2007 [119]). Large-strain and dynamic strength and stiffness behavior during depressurization or thermal stimulation was studied in triaxial experiments (Hyodo et al. 2013, 2014 [40, 39], Song 2014 [96], Ghiassian and Grozic 2013 [33]). In the recent past there

has also been a marked transition towards carrying out studies on undisturbed pressure cores, which will clearly advance the field towards a much better understanding of the mechanics of the gas hydrate-bearing soils (Inada and Yamamoto 2015 [41], Yun 2006 [118], Santamarina 2015 [88], Yoneda et al. 2015 [116]).

Experimental results and micro-mechanical considerations have led to the development of different formulations for elastic yielding parameters (Young's modulus, Poisson ratio). For example, Sultan and Garziglia 2011 [99] assume a linear relationship between gas hydrate stiffness and gas hydrate saturation, which is supported by experimental results reported by Soga et al. 2006 [95] and Waite et al. 2009 [110], while Miyazaki et al. 2010 [58] relate gas hydrate stiffness and peak strength with the strain-rate, besides considering a non-linear relationship between the stiffness and the hydrate saturation. The formulation in this study is based on the earlier findings reported in Santamarina and Ruppel 2010 [87], who propose that the effective-stress-dependent soil stiffness and the gas-hydrate stiffness contribute additively to the stiffness of the gas-hydrate-bearing sediment. The stiffness contribution from gas hydrates is considered as varying non-linearly with the gas hydrate saturation and is, thus, much more pronounced at high gas hydrate saturations.

The focus of this thesis is laid on building a consistent mathematical and numerical framework for simulating hydrate systems using a multi-physics approach. The scope of the model is limited to *gas production* from thermally stimulated or de-pressurized reservoirs, and the mechanical behaviour of the hydrate-bearing soil is modelled under the assumption of linear poro-elasticity. The primary objective is to capture the dynamic coupling between the transport, chemical, and geo-mechanical processes observed at macroscopic scales during methane hydrate formation and dissociation in sandy soil.

Layout of the thesis

In Chapter 2, we present the thermo-chemo-hydro-geo-mechanical model for the simulation of methane gas production from gas hydrate reservoirs.

In Chapter 3, we present the numerical solution strategy. In particular, we discuss a 'cause-effect' based decoupling strategy, where the system of governing PDEs comprising the mathematical model is decoupled into two sub-models (or *blocks*), the flow model and the geomechanical model, with the porosity equation acting as the *glue* between them. In Section 3.1, we summarize the methods used for spatial and temporal discretization of the governing PDEs. In Section 3.2, we present a *block Gauss-Seidel* scheme for iteratively introducing the coupling between the sub-models, and in Section 3.3, we present two multirate time stepping (MRT) schemes based on implicit-explicit (IMEX) approach.

In Chapter 4, the important couplings present in the multi-physics model are identified, and test problems are presented through which we 1) verify each of the model components making up

the hydrate simulator, and 2) show the versatility of the model in the variety of hydrate reservoir related problems it can handle.

In Chapter 5, we evaluate the performance of the MRT schemes presented in Section 3.3 in terms of speed up and accuracy as compared to the iterative block Gauss-Seidel scheme.

In Chapter 6, we present a complex $3D$ example problem, where a typical subsurface hydrate reservoir is destabilized by depressurization. We qualitatively show the capabilities of the model through this example. We also use this example to show the advantage of using multirate time stepping for performing computations in $3D$.

Finally, in Chapter 7, we verify the developed hydrate reservoir model against experimental data. We numerically simulate the results of a controlled triaxial volumetric strain test on a soil sample in which methane hydrate is first formed in situ under controlled isotropic effective stress and then dissociated via depressurization under controlled total stress. The main focus of this work is laid on testing how well our hydro-geomechanical gas hydrate reservoir model captures the coupling between transport, reaction, and mechanical processes during methane hydrate formation and dissociation in sandy soil.

We conclude this thesis with a discussion in Chapter 8 on the current limitations of the developed model, and propose possible extensions and improvements to the model and the numerical solution schemes.

Mathematical model

Methane hydrate formations are a fairly complex subsurface system characterized by a large number of highly interdependent physical phenomena. The typical physical processes occurring in a stimulated hydrate reservoir include 1) hydrate phase change, 2) non-isothermal multi-phase, multi-component flow, 3) geomechanical deformation of the hydrate bearing sediment, and 4) change in the hydraulic as well as the mechanical properties of the hydrate bearing soil. To describe these processes mathematically and to account for their interdependencies in an effective manner, we use a multi-physics approach, which is described in the subsequent sections.

2.1 Macroscopic continuum

We describe the conservation laws for the phases comprising the porous medium using a continuum approach on a macro-scale.

By averaging over all molecules contained in a small volume whose length is greater than the mean free path of the molecules, the substance can be considered as a particle continuum on the micro-scale [11]. Further averaging over an elementary volume which includes several of these microscopic particles leads to a continuum on the macro-scale. Each averaging step involves new quantities characterizing the continuum. The values of these quantities vary with the volume over which they are averaged. If the averaging volume is too small, the quantity will exhibit fluctuations caused by micro-scale effects. If the averaging volume is large enough, the values of the quantities will remain constant with the increasing averaging volume. For very large volumes though, the value of the quantity will increase or decrease if the macro-scale is not completely homogeneous. (See Fig. 2.1.) Bear [11] called the minimum volume needed for a consistent value as the *representative elementary volume*, abbreviated as REV.

Fig. 2.2 illustrates how the porous medium in a particle continuum with specific geometry of the solid matrix, and with a particular distribution of the pore fluids, i.e., water and gas, and solid constituents, i.e., soil and hydrate, is averaged over an REV on a macro-scale. All detailed

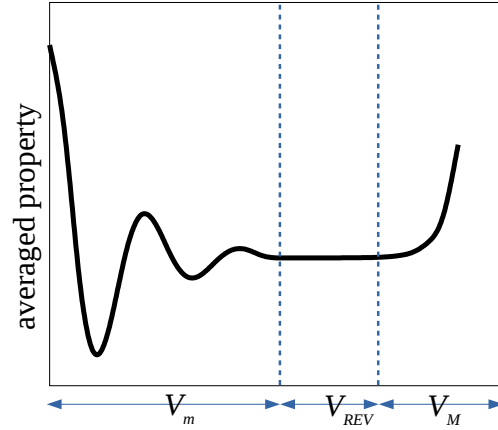


Figure 2.1: A generic property characterizing the porous medium averaged over different volumes. V_m is a micro-scale volume, V_M is a macro-scale volume, and V_{REV} is the elementary volume over which the averaging value is representative for the property it describes.

information is lost. Instead, the composition of the porous medium is characterized by the volume fractions of each phase, the description of the geometry is lumped into averaged variables such as porosity and intrinsic permeability, and the interaction between the fluids, described by interfacial tensions and contact angles on the micro-scale, are lumped into averaged properties such as capillary pressure and relative permeabilities [37].

The basic quantities that characterize the porous medium on macro-scale and the related terminology are introduced below:

- *Phases* are defined as the independent material continua present in the REV, separated by sharp interfaces across which discontinuities in properties exist. A phase can be fluid or solid, and may be composed of a single or several chemical species.
- *Components* are defined as the independent chemical species (e.g., elements, like hydrogen, methane, etc., or compounds, like salt, water, hydrates, etc.) that are necessary for the complete description of the structure of all the phases present in an REV.
- The porous medium, on a macro-scale, is conceptualized as being composed of two distinct parts, 1) a *solid matrix*, composed of the soil continuum, and 2) the *pore spaces*, which are the voids in the matrix which are occupied by the other phases, both fluids and solids.
- *Porosity*, denoted by ϕ , is indicative of packing fraction of the soil particles comprising the solid matrix. It is expressed as the ratio of the pore volume in the REV to the total volume of the REV, i.e., $\phi = \frac{V_p}{V_t}$. The higher the porosity, the more loosely packed the soil is, and the more space there is for the reactive transport of the other phases.

- *Saturation* of any phase γ , denoted by S_γ , is a property which is defined only for those phases which occupy the pore-spaces. Saturation is indicative of the material composition of the porous medium. It is expressed as the ratio of the volume of phase γ within the REV to the volume of the pore spaces in the REV, i.e., $S_\gamma = \frac{V_\gamma}{V_p}$. By definition, the saturation of all pore-filling phases sums up to 1, i.e., $\sum_\gamma S_\gamma = 1$.
- *Mole-fraction*, denoted by χ_γ^κ , quantifies the composition of a phase γ in terms of its constituent components κ . It is expressed as the ratio of number of moles of component κ present in the γ to the number of moles of *all* components present in γ , i.e., $\chi_\gamma^\kappa = \frac{n_\gamma^\kappa}{\sum_\kappa n_\gamma^\kappa}$.
- *Intrinsic permeability*, denoted by $\tilde{\mathbf{K}}_0$, is the measure of the capacity of a porous material to transmit fluid through it. It is a property of the solid matrix, and depends on the geometry, size, and number of interconnected pores, capillaries and fractures composing the solid matrix, or in other words, the microstructure of the soil. For most geological porous materials, the intrinsic permeability is directly proportional to some power of porosity. The soil texture, sorting, and mineralogy also affect the magnitude of permeability by increasing or decreasing the cross-sectional area of open pore space. These factors affect the geometry of the pore space and are independent of fluid types occupying the pores. Permeability, in general, is a tensorial quantity. However, for an isotropic material, permeability can be considered a scalar, i.e., $\tilde{\mathbf{K}}_0 = K_0 \tilde{\mathbf{I}}$.
- *Tortuosity*, denoted by τ , is the ratio of the true or total length L_t of the diffusion path of a fluid particle diffusing through the porous matrix and the straight line distance L between the starting and finishing points of the particle's diffusion, i.e., $\tau = \frac{L_t}{L}$.
- *Capillary pressure*, denoted by P_{c0} , is the pressure difference that occurs across the gaseous and aqueous phase interface due to balancing of cohesive forces within the wetting phase and the adhesive forces between the wetting phase and the soil-matrix.
- *Relative permeabilities* of any fluid phase γ , denoted by $k_{r,\gamma}$, indicate the factor by which the permeability of phase γ is hindered due to the presence of the other phases. Relative permeabilities depend on the saturation of the respective phases. If the porous medium is fully saturated by one phase, its relative permeability is 1, and it approaches 0 as the saturation of the phase tends towards an irreducible (also called *residual*) value.

Additionally, for a deforming solid matrix, the microstructure, in general, changes during the course of deformation. The properties of the micro-structure and the mechanical response of the micro-constituents that comprise the material points are lumped to get an average stress and strain state for the macroscopic continuum bounded by an REV [66]. The mechanical state of the REV is, thus, characterized by equivalent (or average) *displacement*, *strain*, and *total stress* fields, denoted by $\mathbf{u} = \mathbf{u}(\mathbf{x})$, $\tilde{\boldsymbol{\epsilon}} = \tilde{\boldsymbol{\epsilon}}(\mathbf{x})$, and $\tilde{\boldsymbol{\sigma}} = \tilde{\boldsymbol{\sigma}}(\mathbf{x})$, respectively, where, \mathbf{x} is the position vector of a typical point in V_{REV} . The REV must be in equilibrium, and its overall deformation must be compatible. The prescribed surface tensions must be self-equilibrating. The prescribed surface

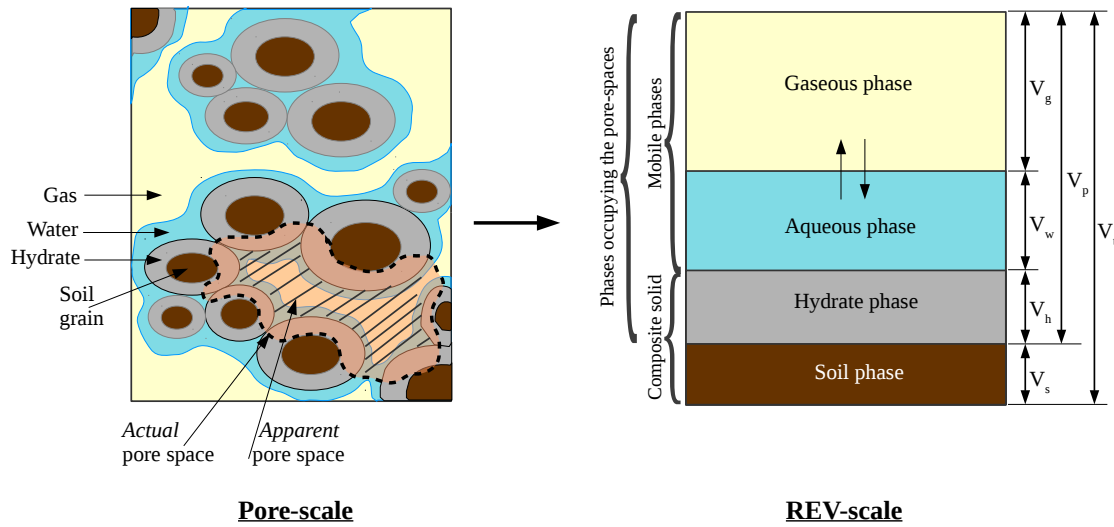


Figure 2.2: Pore-scale to REV-scale

displacements must also be self compatible so that they do not include rigid-body translations and rotations [66].

2.2 Model concept

We consider four *molecular components*: CH_4 , H_2O , $CH_4 \cdot (H_2O)_{N_h}$ (Hydrate), and soil grains, which are present in four distinct *phases*: gaseous, aqueous, hydrate, and soil. The gaseous phase comprises of molecular methane and molecular water in vapour form. The aqueous phase comprises of molecular water and dissolved molecular methane. At this stage the adsorption of methane gas on the surfaces of the solid matrix and the hydrate is not considered. Therefore, the hydrate phase comprises purely of $CH_4 \cdot (H_2O)_{N_h}$, and the soil phase comprises purely of the soil grains. The soil phase is assumed to form the *solid-matrix*, which provides the skeletal structure to the porous medium. The aqueous, gaseous, and hydrate phases exist in the void spaces of this solid matrix (See Fig. 2.2).

At the pore-scale, we make a distinction between the *actual pore-space*, which is the void space outside the soil-grains, and the *apparent pore-space* which is that part of the void space that is not occupied by hydrate and is, thus, available for flow of water and gas. At the REV-scale, this translates to *actual* or *total porosity* $\phi = \frac{V_p}{V_t}$, and *apparent* or *effective porosity* $\phi_{eff} = \frac{V_p - V_h}{V_t}$ (See Fig. 2.2). This distinction is important as it gives us a conceptual advantage in isolating the effects of deformation and hydrate melting on the hydraulic properties of the porous medium. (See Section 2.4.3)

To describe the hydraulic properties in Section 2.4.3 and the effect of hydrate melting on these properties, we make an additional assumption that, at the pore-scale, the hydrate coats the soil grain perfectly, and the water phase forms a film over the hydrate.

In the subsequent discussion, the phases occupying the pore space (gaseous, aqueous, hydrate) will be denoted by ' β ' = g, w, h respectively, the mobile phases (gaseous and aqueous) will be denoted by ' α ' = g, w , and the molecular components making up the fluid phases will be denoted by ' κ ' = CH_4, H_2O . The molecular hydrate, i.e., $CH_4 \cdot (H_2O)_{N_h}$, will be denoted by superscript ' h ', while the phase hydrate will be denoted by subscript ' h '. The soil matrix will be denoted with the subscript ' s '. The soil+hydrate composite matrix will be denoted with the subscript ' sh '. ' γ ' will be used to denote all phases, i.e., $\gamma = g, w, h$, and s .

Assumptions The definition of the mathematical model is based on the following set of assumptions.

- Gas hydrate reservoir is of SI type, i.e., the gas caged in the hydrate is purely methane.
- Ice formation is neglected.
- Aqueous phase is free of any salinity.
- Local thermal equilibrium (LTE) condition prevails in a representative control volume (REV) so that the solid and the neighboring fluid are at the same temperature.
- Gaseous and aqueous phases are treated as ideal mixtures. It is further assumed that the chemical species in the fluid phases attain chemical equilibrium instantaneously. It is important to emphasize that the chemical equilibrium exists only between the fluid phases, not between the fluids and hydrate. The hydrate phase change is a relatively slower process compared with the methane dissolution and water evaporation processes.
- Flow velocities of mobile gaseous and aqueous phases belong to Darcy's Law regime.
- Hydrate is of *grain-coating* type and remains perfectly adhered to the pore walls in the soil matrix.
- Soil and hydrate form a composite material. This material (composite-solid-matrix) is treated as a continuum phase, and the stresses are considered to be acting on this composite-solid-matrix as a whole (and not on the soil matrix alone). The mechanical behaviour of this composite material is described using a linear elastic stress-strain constitutive law. The mechanical properties of this composite material are assumed to vary with the composition and stress-state of the composite-solid-matrix.

2.3 Governing equations

The transport processes characterizing the gas production from a typical sub-surface methane hydrate reservoir can be described by invoking the conservation laws for mass, momentum, and energy described for the macroscale properties of the porous medium [37].

Mass conservation The mass conservation for water and gas is written componentwise, i.e., for each component $\kappa = CH_4, H_2O$, we get,

$$\begin{aligned} & \sum_{\alpha} [\partial_t (\phi \rho_{\alpha} \chi_{\alpha}^{\kappa} S_{\alpha})] + \sum_{\alpha} [\nabla \cdot (\phi \rho_{\alpha} \chi_{\alpha}^{\kappa} S_{\alpha} \mathbf{v}_{\alpha,t})] \\ &= \sum_{\alpha} [\nabla \cdot (\phi S_{\alpha} \mathbf{J}_{\alpha}^{\kappa})] + \dot{g}^{\kappa} + \sum_{\alpha} \dot{q}_{m\alpha}^{\kappa}. \end{aligned} \quad (2.1)$$

The mass conservation for the hydrate phase is given by,

$$\partial_t (\phi \rho_h S_h) + \nabla \cdot (\phi \rho_h S_h \mathbf{v}_{h,t}) = \dot{g}^h. \quad (2.2)$$

The mass conservation for the soil phase is given by,

$$\partial_t [(1 - \phi) \rho_s] + \nabla \cdot ((1 - \phi) \rho_s \mathbf{v}_s) = 0. \quad (2.3)$$

Momentum conservation For mobile phases in porous medium, under certain simplifying assumptions, the momentum conservation can be reduced to Darcy's Law [36], which is stated as,

$$\mathbf{v}_{\alpha} = -K \frac{k_{r\alpha}}{\mu_{\alpha}} (\nabla P_{\alpha} - \rho_{\alpha} \mathbf{g}). \quad (2.4)$$

Here, K is the intrinsic permeability of the *composite* matrix, $k_{r,\alpha}$ and μ_{α} are the relative permeability and the dynamic viscosity of the phase α , respectively.

\mathbf{v}_{α} is the velocity of the mobile phase relative to the soil matrix. The hydrate phase is immobile relative to the soil-matrix, i.e., $\mathbf{v}_h = 0$. The total velocity of any phase β occupying the pores is given by $\phi S_{\beta} \mathbf{v}_{\beta,t} = \mathbf{v}_{\beta} + \phi S_{\beta} \mathbf{v}_s$. The soil phase velocity is the rate of deformation of the soil matrix, and is given by $\mathbf{v}_s = \partial_t \mathbf{u}$.

Momentum conservation for the composite solid matrix is given by,

$$\nabla \cdot \tilde{\sigma} + \rho_{sh} \mathbf{g} = 0. \quad (2.5)$$

Energy conservation For describing the energy conservation in the porous medium, one energy balance equation is sufficient since local thermal equilibrium has been assumed [37]. The energy balance equation is, thus, given by,

$$\begin{aligned} & \partial_t \left[(1 - \phi) \rho_s u_s + \sum_{\beta} (\phi S_{\beta} \rho_{\beta} u_{\beta}) \right] + \sum_{\alpha} [\nabla \cdot (\phi \rho_{\alpha} \chi_{\alpha}^{\kappa} S_{\alpha} \mathbf{v}_{\alpha,t} h_{\alpha})] \\ &= \nabla \cdot k_{eff}^c \nabla T + \dot{Q}_h + \sum_{\alpha} (\dot{q}_{m\alpha}^{\kappa} h_{\alpha}) \end{aligned} \quad (2.6)$$

where, u_γ is the specific internal energy of phase γ , and h_α is the specific enthalpy of a mobile phase α , given by,

$$h_\alpha = \int_{T_{ref}}^T C p_\alpha dT \quad \text{and} \quad u_\gamma = \int_{T_{ref}}^T C v_\gamma dT .$$

Additionally, k_{eff}^c is the effective (or lumped) thermal conductivity of the porous medium, given by,

$$k_{eff}^c = (1 - \phi) k_s^c + \sum_{\alpha} \sum_{\kappa} (\phi \chi_{\alpha}^{\kappa} S_{\alpha} k_{\alpha}^c) + \phi S_h k_h^c .$$

Closure relations The saturations of the phases occupying the pores satisfy the summation condition $\sum_{\beta} S_{\beta} = 1$.

Additionally, for each mobile phase α , the constituting component mole-fractions also satisfy the summation condition $\sum_{\kappa} \chi_{\alpha}^{\kappa} = 1$.

Furthermore, the pressures of the fluid phases are related through a capillary pressure P_c as $P_g - P_w = P_c(S_w)$. The parametrization used for approximating P_c is further elaborated upon in Section 2.4.3.

2.4 Constitutive relationships

In the mathematical model described in Section 2.3 following variables can be identified,

$$S_{\beta} , \chi_{\alpha}^{\kappa} , P_{\alpha} , P_c , T , \phi , \tilde{\sigma} , \mathbf{u} , \mathbf{J}_{\alpha}^{\kappa} , \mathbf{v}_{\alpha} , \dot{g}^{\kappa,h} , \dot{Q}_h \quad (2.7)$$

i.e., the total number of variables is 24. (The vectors and tensors are considered as single variables.) However, the number of governing equations add up to only 12. To close this system 12 additional constitutive relationships are defined for χ_g^{κ} , P_c , $\tilde{\sigma}$, $\mathbf{J}_{\alpha}^{\kappa}$, $\dot{g}^{\kappa,h}$, and \dot{Q}_h in this section. Some other properties which are important for modelling hydrate reservoirs are also discussed.

2.4.1 Vapor-liquid equilibrium

The two-phase CH_4-H_2O fluid system is assumed to be in a state of vapor-liquid-equilibrium. To calculate the concentrations of CH_4 and H_2O in both gaseous and aqueous phases Henry's Law [7] and Raoult's Law [7] for ideal gas-liquid solutions are invoked:

$$\text{For dissolved methane,} \quad \chi_w^{CH_4} = H(T) \chi_g^{CH_4} P_g \quad (2.8)$$

$$\text{For water vapor,} \quad \chi_g^{H_2O} = \chi_w^{H_2O} \frac{P_{H_2O}^{sat}(T)}{P_g} \quad (2.9)$$

Using Eqn. (2.8), Eqn. (2.9), and the summation conditions for each α , $\sum_{\kappa} \chi_{\alpha}^{\kappa} = 1$, the mole fractions can be calculated explicitly.

In Eqn. (2.8), H is Henry's constant for methane gas dissolved in water and is calculated in our model using the empirical relation from NIST standard reference database [86]. In Eqn. (2.9), $P_{H_2O}^{sat}$ is the saturated vapour pressure for water in contact with methane gas. We use Antoine's equation [7] to calculate $P_{H_2O}^{sat}$.

2.4.2 Fick's law for diffusive mass-transfer flux

The diffusive solute flux through sediment \mathbf{J}_α^κ is calculated using Fick's Law [36], as stated below

$$\mathbf{J}_\alpha^\kappa = -\tau D^\alpha (\rho_\alpha \nabla \chi_\alpha^\kappa) . \quad (2.10)$$

where, D^α is the binary diffusion coefficient in the mobile phases $\alpha = g, w$. The gas-phase binary diffusion coefficient for low density binary $CH_4 - H_2O$ system is estimated using the empirical relationship proposed by Statter and Bird [97]. For the aqueous phase binary diffusion coefficient, Wilke-Chang correlation [38] for dilute associated liquid mixtures is used.

2.4.3 Properties of the fluid-matrix interaction

Capillary pressure On the macro scale, the capillary pressure in a porous medium is an average pressure depending on the pore-size distribution and the aqueous phase saturation. Several parameterizations exist which relate the capillary pressure and effective aqueous phase saturation using soil specific parameters. Our model uses one of the most common parameterizations proposed by Brooks and Corey [14].

For an un-deformed, un-hydrated soil matrix the capillary pressure is expressed as a function of effective (or normalized) aqueous phase saturation, as given below,

$$P_{c0} = P_{entry} S_{we}^{-1/\lambda_{BC}} \quad (2.11)$$

where, P_{entry} is the gas entry pressure, λ_{BC} is the soil specific parameter depending on the pore-size distribution, and S_{we} is the normalized aqueous phase saturation given by,

$$S_{we} = \frac{S_w - (S_{wr} + S_{gr})}{1 - S_h - (S_{wr} + S_{gr})} ,$$

where, S_{wr} and S_{gr} are the irreducible water and gas phase saturations, respectively.

The effect of presence of hydrate in the soil matrix and the changing hydrate saturation on the capillary pressure P_c is modelled by scaling P_{c0} with a scaling-factor $f_{S_h}^{P_c}$ which is a function of S_h [20, 79]. Also, the effect of changing porosity due to deformation of the porous matrix is accounted for by scaling P_{c0} with a scaling-factor $f_\phi^{P_c}$ which is a function of ϕ using Civan's power-law correlation [19]. Thus, the capillary pressure is given by,

$$P_c = P_{c0} \cdot f_{S_h}^{P_c}(S_h) \cdot f_{\phi}^{P_c}(\phi) \quad (2.12)$$

where,

$$f_{S_h}^{P_c} = (1 - S_h)^{-\frac{m\lambda_{BC}-1}{m\lambda_{BC}}}, \text{ and } f_{\phi}^{P_c} = \frac{\phi_0}{\phi} \left(\frac{1 - \phi}{1 - \phi_0} \right)^a$$

where m and a are model parameters.

Intrinsic permeability The intrinsic permeability, K , is related to the *connectivity of the pore spaces* and the *grain size* of the soil. An estimate of the intrinsic permeability can be made using mathematical expressions such as those proposed by Bear [11], or Mualem [65]. Usually, however, the intrinsic permeability is evaluated experimentally as part of the characterization of the soil sample.

The effect of changing hydrate saturation on the intrinsic permeability is modelled by scaling the initial or reference intrinsic permeability of the sediment K_0 with a scaling-factor $f_{S_h}^K$ which is a function of S_h [20, 79], and, the effect of changing porosity due to deformation of the porous matrix is accounted for by scaling K_0 with a scaling-factor f_{ϕ}^K which is a function of ϕ using Civan's power-law correlation [19]. Thus, the intrinsic permeability for the hydrate sample is modelled as,

$$K = K_0 \cdot f_{S_h}^K(S_h) \cdot f_{\phi}^K(\phi) \quad (2.13)$$

where,

$$f_{S_h}^K = (1 - S_h)^{\frac{5m+4}{2m}}, \text{ and } f_{\phi}^K = \frac{\phi}{\phi_0} (f_{\phi}^{P_c})^{-2}.$$

These scaling factors (for both, P_c and κ) are derived based on the assumption that hydrate phase sticks uniformly at the pore surface. For the ideal case of a spherical pore geometry, $m = 3$.

Relative permeabilities The relative permeability factors for both mobile phases are evaluated using the Brooks-Corey model in conjunction with the Burdine theorem [16], as,

$$k_{rw} = S_{we}^{\frac{2+3\lambda_{BC}}{\lambda_{BC}}}, \text{ and } k_{rg} = (1 - S_{we})^2 \left(1 - S_{we}^{\frac{2+\lambda_{BC}}{\lambda_{BC}}} \right). \quad (2.14)$$

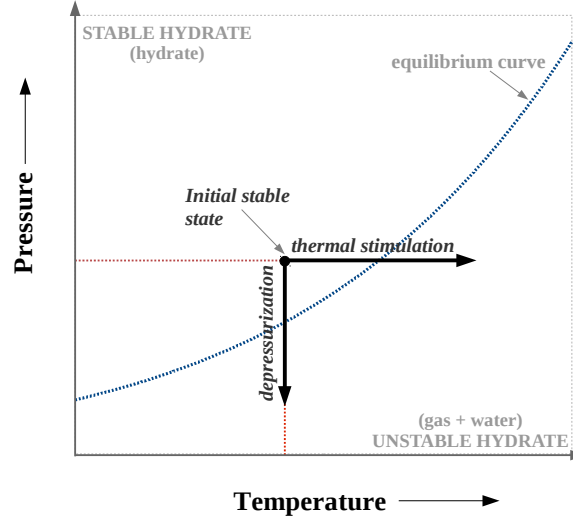


Figure 2.3: Methane hydrate P-T phase curve

Specific surface area An important property of the porous matrix is its specific surface area, A_s , which is defined as the ratio of the total internal surface area of the pores enclosed within an REV to the total volume of the REV. The correlation proposed by Yousif [117] is used for estimating the specific surface area of the porous matrix,

$$A_s = \sqrt{\frac{\phi_{eff}^3}{2K}} \quad \text{where,} \quad \phi_{eff} = \phi(1 - S_h) . \quad (2.15)$$

Hydraulic tortuosity Tortuosity is empirically related to porosity, as,

$$\tau = \phi^n \quad \text{where,} \quad 1 \leq n \leq 3 . \quad (2.16)$$

2.4.4 Hydrate phase change kinetics

Methane hydrates, upon heating or depressurization, decompose to produce methane gas and water as shown in Fig. 2.3. Chemically, this phase change process can be expressed as $CH_4 \cdot (H_2O)_{N_h} \rightleftharpoons CH_4 + N_h \cdot H_2O$, where, N_h is the hydration number.

This non-equilibrium phase change of methane hydrate is modeled by the Kim-Bishnoi kinetic model [45]. The rate of gas generated or consumed on hydrate decomposition or reformation is given by,

$$\dot{g}^{CH_4} = k_{reac} M_{CH_4} A_{rs} (P_e - f_g) . \quad (2.17)$$

Correspondingly, the rates of water and methane hydrate generated/consumed are given by,

$$\dot{g}^{H_2O} = \dot{g}^{CH_4} N_h \frac{M_{H_2O}}{M_{CH_4}}, \text{ and } \dot{g}^h = -\dot{g}^{CH_4} \frac{M_h}{M_{CH_4}}. \quad (2.18)$$

In Eqn. (2.17), k_{reac} is the kinetic rate constant given by,

$$k_{reac} = k_{reac}^0 \exp\left(-\frac{\Delta E_a}{R T}\right) \quad (2.19)$$

where, E_{act} is the activation energy, and k_{reac} is the intrinsic rate constant for the kinetic phase change.

A_{rs} is the specific reaction area, and is a measure of the actual surface available for the kinetic-reaction to occur. It puts a limit on the mass transfer during hydrate formation and dissociation. As the hydrate saturation in the pore-space increases, the availability of free surface for the hydrate formation to occur decreases, and vice versa. Additionally, for hydrate formation to occur, availability of both gas and water in sufficient quantities in the pore space is a necessary condition. This behaviour of A_{rs} is modelled as,

$$A_{rs} = \Gamma_r A_s \quad (2.20)$$

$$\text{s.t., } \Gamma_r = \begin{cases} \phi S_h & \text{for } (P_e - f_g) > 0 \\ (S_g S_w S_h)^{\frac{2}{3}} & \text{for } (P_e - f_g) \leq 0. \end{cases}$$

where, Γ_r is the fraction of the pore surface area that is active in hydrate kinetics [100].

The methane gas fugacity f_g in the kinetic model is computed based on the Peng-Robinson's thermodynamic equation of state for methane [73]. The equilibrium pressure for the methane hydrate P_e is determine using the Kamath and Holder correlation [43] as given below,

$$P_e = A_1 \exp\left(A_2 - \frac{A_3}{T [\text{K}]}\right). \quad (2.21)$$

Methane hydrate dissociation reaction is an endothermic process. Conversely, methane hydrate re-formation is an exothermic reaction. The heat of reaction for hydrate phase change is modelled by,

$$\dot{Q}_h = \frac{\dot{g}^h}{M_h} \left(B_1 - \frac{B_2}{T [\text{K}]}\right). \quad (2.22)$$

2.4.5 Poro-elasticity

Principle of effective stress When a porous fluid-filled soil encounters an external load, the stress is partly supported by the soil matrix and partly by the pore-fluids. The deformation of the porous medium is effected by only that part of the total stress that is supported by the soil matrix. This stress, introduced by Terzaghi [104], is called the effective stress. Using this concept, the total stress $\tilde{\sigma}$ appearing in Eqn. (2.5) can be decomposed as,

$$\tilde{\sigma} = \tilde{\sigma}' + \alpha_{biot} P_{eff} \tilde{I} \quad (2.23)$$

where, $\tilde{\sigma}$ is the total stress acting on the bulk porous medium, $\tilde{\sigma}'$ is the effective stress acting on the composite skeleton, and P_{eff} is the effective pore-pressure exerted by the mobile phases, given by,

$$P_{eff} = \frac{S_w}{S_w + S_g} P_w + \frac{S_g}{S_w + S_g} P_g.$$

The parameter α_{biot} is Biot's constant. One of the generally accepted expressions for α_{biot} in rock-mechanics applications is $\alpha_{biot} = 1 - \frac{B_m}{B_{sh}}$ [13]. Here, B_{sh} is the bulk modulus of the composite matrix, and B_m is the bulk modulus of the porous medium.

Stress-strain behaviour The deviatoric stress vs. axial strain response obtained from tri-axial tests of distributed hydrate-bearing sands reported by Masui et al. [56] and Miyazaki et al. [59] show that the hydrate-sand specimens are not elastic bodies, but it is possible to consider the stress-strain relationship to be elastic if the range of application is sufficiently limited to small-strain cases far away from the critical state.

In our model, we use the linear-elastic constitutive law to describe the stress-strain response of the hydrate-soil composite matrix, given as,

$$\tilde{\sigma}' = 2 G_{sh} \tilde{\epsilon} + \lambda_{sh} (tr \tilde{\epsilon}) \tilde{I} \quad (2.24)$$

where, G_{sh} and λ_{sh} are the Lamé's parameters for the elastic composite-matrix and can be defined in terms of the *apparent* elastic mechanical properties (e.g. Young's modulus E_{sh} , and Poisson's ratio ν_{sh}) as,

$$G_{sh} = \frac{E_{sh}}{2(1 + \nu_{sh})}, \quad \lambda_{sh} = \frac{E_{sh} \nu_{sh}}{(1 + \nu_{sh})(1 - 2\nu_{sh})}. \quad (2.25)$$

$\tilde{\epsilon}$ is the linearized strain, given by $\tilde{\epsilon} = \frac{1}{2} (\nabla \mathbf{u} + \nabla^T \mathbf{u})$.

Elastic properties From the tri-axial tests it is observed that the presence of methane hydrate, in general, increases stiffness and leads to higher strength. Also, the effect of methane hydrate saturation on the Poisson ratio appears to be small. Further details on the general trends of mechanical properties of methane hydrates can be found in Waite et al. [110], and Soga et al. [95].

To make the model consistent with these observations, we assume the Poisson ratio ν_{sh} to be a constant, and we define the Young's modulus using the expression proposed by Santamarina and Ruppel [87], given as,

$$E_{sh} = E_{s0} \left(\frac{\sigma_c}{\sigma_{c0}} \right)^b + c E_h (S_h)^d \quad (2.26)$$

where, E_{s0} is the isothermal Young's modulus of hydrate-free sand at the reference confining stress of $\sigma_{c0} = 1$ kPa, b is the sensitivity of the Young's modulus of hydrate-free sand to confining stress σ_c , c is the contribution of the isothermal Young's modulus of hydrate for a given pore habit, i.e., pore filling, cemented (grain-coating), or patchy, and d is the nonlinear effect of hydrate saturation.

Compressibility The grains of the composite material are assumed to be incompressible, but the bulk material as a whole is compressible. This compressibility can be attributed to the fact that due to the pore pressure variations or isotropic loading the grains redistribute, which, on macro scale, manifests as change in density of the solid material. This change in density can be modelled as,

$$\frac{\partial}{\partial t} \rho_{sh} = \frac{\rho_{sh}}{G_{sh} (1 - \phi_{eff})} \left(\frac{\partial}{\partial t} \sigma - \phi \frac{\partial}{\partial t} P_{eff} \right) \quad (2.27)$$

where, σ is the isotropic stress.

Numerical solution strategy

The mathematical model describing the hydromechanical processes in a hydrate system actually contains two sub-classes of models, the *flow and transport model* comprising of the mass, momentum, and energy balance equations for the phases occupying the pore spaces in the hydrate formation, i.e., equations (2.1), (2.2), (2.4), and (2.6), and the *geomechanical model*, comprising of momentum balance equation (2.5). The soil phase mass balance, Eqn (2.3), can be seen as a *mortar* between these two sub-models (Fig. 3.1).

The interaction between these two models manifests physically in the form of, a) changes in the hydraulic properties (total porosity and permeability) due to deformation of the solid matrix structure, b) shift in the seepage velocity of the pore fluids due to the rate of deformation of the solid matrix, and, c) changes in the mechanical properties of the solid matrix (strength, bulk modulus, density, etc.) resulting from the flow dynamics of the pore-fluids and the loss in cementation due to melting of the hydrate phase. In other words, each model affects the other model by altering its *properties*. Thus, the nature of the coupling between these two models is dynamic, but weak.

We use this observation to devise a decoupled solution strategy. Broadly speaking, we first decouple the flow model and the geomechanical model, and solve them separately for a given time-step. Then, we iteratively re-introduce the coupling through a block Gauss-Seidel solution scheme, which is summarized in Sec. 3.2. This iteratively coupled solution scheme greatly reduces the computational effort as compared to a monolithic fully implicit scheme.

However, the dynamics of the flow and the geomechanical models evolve at very different time scales. We know a priori that the ground deformations manifest at a much slower rate as compared to the flow and transport processes. Since the refinement of the time-mesh is controlled by the dynamics of active (or the fast) components, solving the latent (or the slow) components at this fine time-mesh results in redundant computational work. The computation can be made more efficient if the slow components are solved on a coarse time-mesh and the fast components

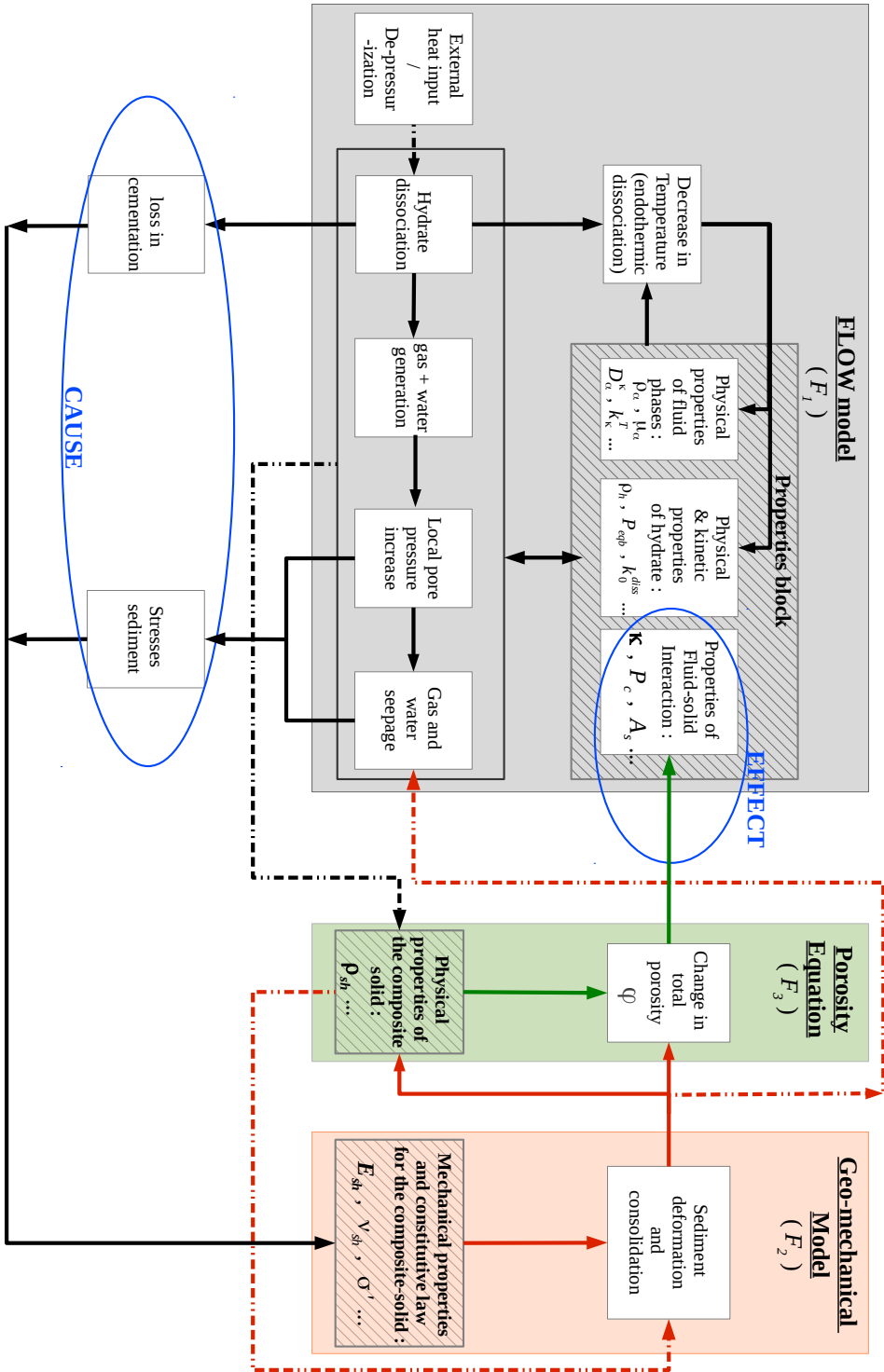


Figure 3.1: 'Cause-effect' based interaction between flow and geomechanical models. The bold arrows represent the direct forward coupling, (e.g. $F_1 - F_1$ or $F_1 - F_2, F_2 - F_3, F_3 - F_1$). The dashed arrows represent indirect coupling (e.g. $F_1 - F_3$) or backward coupling (e.g. $F_2 - F_1, F_3 - F_2$).

on a fine time-mesh. Such time stepping methods are called the *Multi-Rate Time-stepping (MRT) methods*. We present, in Sec. 3.3, two MRT algorithms which we use for speeding up our hydro-geomechanical hydrate reservoir model. The first MRT algorithm is based on a *semi-implicit* approach and the second is based on a *compound-fast* approach.

We chose the following set of variables as the primary variables: the gas phase pressure P_g , the aqueous phase saturation S_w , the hydrate phase saturation S_h , the temperature T , the total-porosity ϕ , and, the composite-matrix displacement \mathbf{u} . All other variables can be derived (explicitly or implicitly) from this set of variables.

The methods used for the spatial and temporal discretization of the PDE-systems comprising the sub-models are summarized in Sec. 3.1. The strong non-linearities in each of the sub-models are dealt with using a damped Newton-Raphson linearization. Each of the resulting linear sub-systems are solved using the SuperLU linear solver [25]. Both the numerical schemes, block Gauss-Seidel and MRT, are implemented in the C++ based DUNE-PDELab framework [10]. The numerical code is capable of solving problems in $1D$, $2D$, and $3D$ spatial domains. Furthermore, the *block* structure of the decoupling scheme makes the code modular, and gives the flexibility to solve either the flow model alone or the full geo-mechanical model, depending on the problem at hand.

3.1 Discretization schemes

The system of PDEs comprising the flow-system are solved fully implicitly for the variables P_g , S_w , S_h , and T . The spatial discretization is done using the fully up-winded classical cell centered finite volume method, which is summarized in Sec. 3.1.1. Orthogonal grids aligned with the principal axes are defined and a control-volume formulation with two-point flux approximation (TPFA) is used. For time-stepping, an implicit Euler method is used, which is summarized in Sec. 3.1.3.

The geomechanical system is solved for the primary variable \mathbf{u} . The soil momentum balance equation comprising the geomechanical model is spatially discretized using the standard Galerkin finite element (FEM) scheme defined on $Q1$ elements. The FEM formulation is summarized in Sec. 3.1.2.

The soil-phase mass-balance equation is solved separately for ϕ . It is also spatially discretized using the cell centered finite-volume method, and is marched forward in time using the implicit Euler method.

3.1.1 Space discretization: Finite volume method

The conservation law for a generic conserved quantity F s.t., $F = \rho f$, can be expressed as,

$$\partial_t \rho f + \nabla \cdot \rho f \mathbf{v}_t = \nabla \cdot \rho d \nabla f + q \quad (3.1)$$

where, the quantity $\rho f \mathbf{v}_t$ is the total convective flux, the quantity $\rho d \nabla f$ is the diffusive flux, and the quantity q is the volumetric source of F .

For fluid flow through a deformable porous medium, $\mathbf{v}_t = \mathbf{v}_f + \mathbf{v}_s$, where, \mathbf{v}_f is the interstitial velocity with which the property F is convected and \mathbf{v}_s is the velocity of the solid matrix. The divergence of the convective flux in Eqn. (3.1) can be expanded as,

$$\nabla \cdot \rho f \mathbf{v}_t = \nabla \cdot \rho f \mathbf{v}_f + \rho f \nabla \cdot \mathbf{v}_s + \mathbf{v}_s \cdot \nabla \rho f .$$

For the case of rapidly changing effective stress relative to the fluid mobility together with the small-strain assumption, the term $\mathbf{v}_s \cdot \nabla \rho f$ can be neglected [81]. In addition, the divergence of the solid velocity, i.e. $\nabla \cdot \mathbf{v}_s$, can be expressed in terms of the volumetric strain ϵ_v of the solid-matrix [12], as,

$$\nabla \cdot \mathbf{v}_s = \frac{D \epsilon_v}{Dt} \approx \partial_t \epsilon_v$$

where, $\partial_t \epsilon_v$ is the volumetric strain rate.

Therefore, the conservation law for F , Eqn. (3.1), can be approximated as,

$$\partial_t \rho f + \nabla \cdot \rho f \mathbf{v}_f + \rho f \partial_t \epsilon_v = \nabla \cdot \rho d \nabla f + q \quad (3.2)$$

The Table 3.1 gives an overview of the mass and energy conservation laws expressed in terms of the generic conservation law, Eqn. (3.2).

The finite volume based spatial discretization of Eqn. (3.2) is based on a balance approach: 1) the problem domain is subdivided into local closed entities called the *control volumes*, and a local balance is written on each control volume; 2) using the divergence theorem, an integral formulation of the fluxes on the boundary of a control volume is obtained; and finally, 3) the integral formulation is discretized in space with respect to the discrete unknowns. We now elaborate on the steps involved in the finite volume discretization process.

Cell centered grid

A cell centered grid of a spatial domain $\mathcal{D} \subset \mathbb{R}^d$ consists of a set of closed control volumes $\mathcal{V} = \{\mathcal{V}_i \subset \mathcal{D} : i = 1, \dots, I\}$ and a set of storage locations $\mathcal{X} = \{\mathbf{x}_i \in \mathcal{D} : i = 1, \dots, I\}$, s.t.,

- \mathbf{x}_i is at the center of mass of \mathcal{V}_i .
- The volumes cover the entire spatial domain: $\mathcal{D} = \bigcup_{i=1}^I \mathcal{V}_i$.
- The volumes do not overlap, i.e., for all $i \neq j$, either,

$$\mathcal{V}_i \cap \mathcal{V}_j = \emptyset$$

or, if the volumes are adjacent,

$$\mathcal{V}_i \cap \mathcal{V}_j = \partial \mathcal{V}_i \cap \partial \mathcal{V}_j$$

where, $\partial \mathcal{V}_i$ denotes the boundary of \mathcal{V}_i .

Table 3.1: Mass and Energy balance equations in terms of the generic conservation law, Eqn. (3.2)

	conserved quantity	convective flux	diffusive flux	volumetric source
Mass conservation for components $\kappa = CH_4, H_2O$	$F \quad \sum_{\alpha=g,w} \phi \rho_{\alpha} S_{\alpha} \chi_{\kappa}^{\alpha}$	$F \mathbf{v}_f \quad \sum_{\alpha=g,w} \phi \rho_{\alpha} S_{\alpha} \chi_{\kappa}^{\alpha} \mathbf{v}_{\alpha}$ where, $\mathbf{v}_{\alpha} = -\frac{K^{k_{r\alpha}}}{\mu_{\alpha} \phi S_{\alpha}} (\nabla P_{\alpha} - \rho_{\alpha} \mathbf{g})$	$\rho d \nabla f \quad \sum_{\alpha=g,w} \phi \rho_{\alpha} S_{\alpha} \mathbf{j}_{\alpha}^{\kappa}$ where, $\mathbf{j}_{\alpha}^{\kappa} = -\tau D^{\alpha} \nabla \chi_{\alpha}^{\kappa}$	$q \quad \dot{g}^{\kappa}$
Mass conservation for hydrate phase	$\phi \rho_h S_h$	0.	0.	\dot{g}^h
Mass conservation for soil phase	$(1 - \phi) \rho_s$	0.	0.	0.
Energy conservation	$\sum_{\beta=g,w,h} (\phi \rho_{\beta} S_{\beta} \overline{C_{\beta}} \Big _v T) + (1 - \phi) \rho_s \overline{C_s} \Big _v T$	$\sum_{\alpha=g,w} (\phi \rho_{\alpha} S_{\alpha} \overline{C_{\alpha}} \Big _p T \mathbf{v}_{\alpha})$	$\sum_{\beta=g,w,h} (\phi \rho_{\beta} S_{\beta} \overline{C_{\alpha}} \Big _p \mathbf{j}_{\beta}^{th}) + (1 - \phi) \rho_s \overline{C_{\alpha}} \Big _p \mathbf{j}_s^{th}$ where, $\mathbf{j}_{\gamma}^{th} = -\frac{k_{\gamma}^c}{\overline{C_{\alpha}} \Big _p} \nabla T$	$\dot{Q}_h + \sum_{\alpha=g,w} (\dot{q}_{m_{\alpha}}^{\kappa} h_{\alpha})$

$\overline{C_{\gamma}} \Big|_v$ is the specific heat capacity at constant volume. $\overline{C_{\gamma}} \Big|_p$ is the specific heat capacity at constant pressure.

For immobile phases, i.e. $\gamma = s, h$, $\overline{C_{\gamma}} \Big|_v = \overline{C_{\gamma}} \Big|_p$. For mobile phases, i.e. $\gamma = g, w$, $\overline{C_{\gamma}} \Big|_v = \overline{C_{\gamma}} \Big|_p - R_{\gamma}$.

The grid is denoted as $\mathcal{G} = (\mathcal{V}, \mathcal{X})$. The control volumes \mathcal{V} , also called *cells*, are chosen to be quadrilateral in shape for $\mathcal{D} \subset \mathbb{R}^2$ and hexahedral for $\mathcal{D} \subset \mathbb{R}^3$.

Integral form

Given the cell centered grid \mathcal{G} for the space domain \mathcal{D} , if K grid cells are adjacent to the open boundary $\partial\mathcal{D}$, introduce K adjacent virtual cells $\mathcal{V}_{I+1}, \dots, \mathcal{V}_{I+K}$. Let \mathcal{J}_i contain the indices of the neighbours of grid cell \mathcal{V}_i , s.t.,

$$\mathcal{J}_i = \{j \in \{1, \dots, I+K\} : \mathcal{V}_i \cap \mathcal{V}_j \neq \emptyset\}.$$

Further, let S_{ij} denote the joint boundary of the neighbouring grid cells \mathcal{V}_i and \mathcal{V}_j , s.t.,

$$S_{ij} = \partial\mathcal{V}_i \cap \partial\mathcal{V}_j.$$

Also, let \mathbf{n}_{ij} be the unit normal vector on S_{ij} directed towards \mathcal{V}_j .

Then, the integral form of the conservation law, which results from integrating Eqn. (3.2) over the cell volume and using the Gauss' divergence theorem to convert the volume integral of the divergence of a flux of F to the surface integral of the flux of F , can be expressed as,

$$\begin{aligned} & \partial_t \int_{\mathcal{V}_i} \rho f \, d\mathbf{x} + \sum_{j \in \mathcal{J}_i} \int_{S_{ij}} \rho f \mathbf{v}_f \cdot \mathbf{n}_{ij} \, d\mathbf{x} + \int_{\mathcal{V}_i} \rho f \, \partial_t \epsilon_v \, d\mathbf{x} \\ &= \sum_{j \in \mathcal{J}_i} \int_{S_{ij}} \rho d \nabla f \cdot \mathbf{n}_{ij} \, d\mathbf{x} + \int_{\mathcal{V}_i} q \, d\mathbf{x} \end{aligned} \quad (3.3)$$

We define the following volume and boundary averages for any quantity φ :

$$\bar{\varphi}_i(t) = \begin{cases} \frac{1}{|\mathcal{V}_i|} \int_{\mathcal{V}_i} \varphi(\mathbf{x}, t) \, d\mathbf{x}, & i = 1, \dots, I, \text{ and } \mathbf{x} \in \mathcal{V}_i, \\ \frac{1}{|\mathcal{V}_i \cap \partial\mathcal{D}|} \int_{\mathcal{V}_i \cap \partial\mathcal{D}} \varphi(\mathbf{x}, t) \, d\mathbf{x}, & i = I+1, \dots, I+K, \text{ and } \mathbf{x} \in \mathcal{V}_i. \end{cases} \quad (3.4)$$

and,

$$\bar{\varphi}_{ij}(t) = \frac{1}{|S_{ij}|} \int_{S_{ij}} \varphi(\mathbf{x}, t) \, d\mathbf{x}, \quad \mathbf{x} \in S_{ij} \quad (3.5)$$

where, $|\mathcal{V}_i|$ denotes the volume of \mathcal{V}_i , and $|S_{ij}|$ denotes the surface area of S_{ij} .

Using definitions 3.4 and 3.5, we can re-write the integral form of the conservation law in Eqn. (3.3) as,

$$\begin{aligned} & \partial_t \bar{F}_i |\mathcal{V}_i| + \sum_{j \in \mathcal{J}_i} |S_{ij}| \bar{F}_{ij} \bar{\mathbf{v}}_{f_{ij}} \cdot \mathbf{n}_{ij} + \bar{F}_i \partial_t \bar{\epsilon}_v |\mathcal{V}_i| \\ &= \sum_{j \in \mathcal{J}_i} |S_{ij}| \bar{\rho}_{ij} \bar{d}_{ij} \nabla f \cdot \mathbf{n}_{ij} + \bar{q}_i |\mathcal{V}_i|. \end{aligned} \quad (3.6)$$

The terms $\mathcal{F}_{Cij} := \bar{F}_{ij} \bar{\mathbf{v}}_{f_{ij}} \cdot \mathbf{n}_{ij}$ are the convective fluxes, and the terms $\mathcal{F}_{Dij} := \bar{\rho}_{ij} \bar{d}_{ij} \nabla f \cdot \mathbf{n}_{ij}$ are the diffusive fluxes across the cell interfaces.

Finite volume approximation

If φ is the quantity being solved for (i.e. the primary variable), and the quantities f , ρ , d and q in the generic conservation law (3.1) are functions of φ , then the finite volume method approximates φ over the domain \mathcal{D} using a piecewise constant function defined over the cell centered grid \mathcal{G} , s.t.,

$$\varphi(\mathbf{x}, t) \approx \varphi_a(\mathbf{x}, t) = \sum_{i=1}^I \tilde{\varphi}_i(t) \omega_i(\mathbf{x}) \quad (3.7)$$

$$\text{where, } \omega_i(\mathbf{x}) = \begin{cases} 1 & \mathbf{x} \in \mathcal{V}_i \\ 0 & \mathbf{x} \notin \mathcal{V}_i \end{cases}$$

$$\text{and, } \tilde{\varphi}_i(t) = \bar{\varphi}_i(t)$$

The gradient of the finite volume solution φ_a across the cell interfaces is approximated using a finite difference two-point flux method [], as,

$$\nabla \varphi_a(\mathbf{x}, t) \cdot \mathbf{n}_{ij} = \frac{\bar{\varphi}_j(t) - \bar{\varphi}_i(t)}{\|\mathbf{x}_j - \mathbf{x}_i\|_2} \quad (3.8)$$

Since the finite volume solution φ_a is discontinuous across the cell interfaces, the value $\bar{\varphi}_{ij}$ is not uniquely defined. Therefore, the convective fluxes and the diffusive fluxes across the cell interfaces are approximated through the numerical flux functions $\Phi_{Cij}(\bar{\varphi}_i, \bar{\varphi}_j)$ and $\Phi_{Dij}(\bar{\varphi}_i, \bar{\varphi}_j)$, respectively.

Numerical convective flux function: The convective flux \mathcal{F}_C has a hyperbolic characteristic. Therefore, Φ_C is approximated using a first order upwind-biased discretization of the convection terms, as,

$$\Phi_{Cij} = \theta \bar{F}_i \bar{\lambda}_i \zeta_{ij} + (1 - \theta) \bar{F}_j \bar{\lambda}_j \zeta_{ij} \quad (3.9)$$

$$\text{where, } \zeta_{ij} = \left(\nabla P - \frac{\bar{\rho}_i + \bar{\rho}_j}{2} \mathbf{g} \right) \cdot \mathbf{n}_{ij}$$

$$\text{and, } \theta = \begin{cases} 1 & \text{if, } \zeta_{ij} \leq 0 \\ 0 & \text{if, } \zeta_{ij} > 0. \end{cases}$$

Numerical diffusive flux function: The diffusive flux \mathcal{F}_D has a parabolic characteristic. Therefore, Φ_D is approximated using a central difference discretization of the diffusion terms,

as,

$$\Phi_{Dij} = \left(\frac{\bar{\rho}_i \bar{d}_i + \bar{\rho}_j \bar{d}_j}{2} \right) \nabla f \cdot \mathbf{n}_{ij} \quad (3.10)$$

Therefore, the cell-wise spatial discretization of the conservation law (3.2) in a domain \mathcal{D} using a cell centered finite volume method is given as,

$$\partial_t \bar{F}_i |\mathcal{V}_i| = \sum_{j \in \mathcal{J}_i} (\Phi_{Dij} - \Phi_{Cij}) |S_{ij}| + (\bar{q}_i - \bar{F}_i \partial_t \bar{\epsilon}_{vi}) |\mathcal{V}_i|. \quad (3.11)$$

3.1.2 Space discretization: Finite element method

The governing field equations for the linear poroelasticity problem consist of,

$$\text{solid-phase momentum balance: } -\nabla \cdot (\tilde{\sigma}' + P\tilde{\mathbf{I}}) = \rho \mathbf{g}, \quad (3.12)$$

$$\text{strain-displacement relationship: } \tilde{\epsilon} = \frac{1}{2} (\nabla \mathbf{u} + \nabla \mathbf{u}^T), \quad (3.13)$$

$$\text{and, stress strain constitutive law: } \tilde{\sigma}' = 2G\tilde{\epsilon} + \lambda (\text{tr}\tilde{\epsilon}) \tilde{\mathbf{I}}, \quad (3.14)$$

where, $\tilde{\sigma}'$ is the Cauchy stress acting on the solid matrix, $\tilde{\epsilon}$ is the linear stress tensor, G and λ are the Lamé's parameters, ρ is the density of the solid matrix, and P is the effective pressure given by,

$$P = \frac{\alpha_{biot} \sum_{\alpha=g,w} S_\alpha P_\alpha}{\sum_{\alpha=g,w} S_\alpha}.$$

The displacement form (or the irreducible form) of the momentum balance Eqn. (3.12) can, thus, be expressed as,

$$-\nabla \cdot \left[G (\nabla \mathbf{u} + \nabla \mathbf{u}^T) + \lambda (\nabla \cdot \mathbf{u}) \tilde{\mathbf{I}} \right] = \nabla P + \rho \mathbf{g} \quad (3.15)$$

where, $\mathbf{f}_b := \nabla P + \rho \mathbf{g}$ represents the body forces acting on the solid matrix.

The linear (poro)-elasticity problem can be stated as:

Problem: Given the problem domain $\mathcal{D} \subset \mathbb{R}^d$, and time domain $t \in \mathbb{R}, t \geq 0$, find \mathbf{u} , s.t.,

$$\text{for } t = 0 : \quad \mathbf{u} = \bar{\mathbf{u}}_0 \quad (3.16)$$

$$\text{and, for } t > 0 : \quad -\nabla \cdot \tilde{\sigma}' - \mathbf{f}_b = 0 \quad \text{in } \mathcal{D} \quad (3.17)$$

$$\mathbf{u} = \bar{\mathbf{u}} \quad \text{on } \partial\mathcal{D}_D \quad \text{and} \quad \mathbf{t} := \tilde{\sigma}' \mathbf{n} = \bar{\mathbf{t}} \quad \text{on } \partial\mathcal{D}_N. \quad (3.18)$$

Eqn. (3.17) is called the *strong form* of the linear (poro)-elasticity problem. Also, note that the boundary of the domain \mathcal{D} is divided into two distinct and complementary parts, $\partial\mathcal{D}_D$ and $\partial\mathcal{D}_N$, such that,

$$\begin{aligned}\partial\mathcal{D}_D \cup \partial\mathcal{D}_N &= \partial\mathcal{D}, \\ \partial\mathcal{D}_D \cap \partial\mathcal{D}_N &= \emptyset.\end{aligned}$$

The part $\partial\mathcal{D}_D$ is associated with the Dirichlet boundary condition, where the prescribed displacement values are enforced. The part $\partial\mathcal{D}_N$ is associated with the Neumann boundary condition, where the prescribed traction values are enforced.

We now present a finite element discretization procedure for the linear (poro)-elasticity problem given by Eqns. (3.16)-(3.18).

Finite element grid

Given the spatial domain $\mathcal{D} \subset \mathbb{R}^d$ and the cell centered grid $\mathcal{G} = \{\mathcal{V}, \mathcal{X}\}$, we now define a finite element grid $\mathcal{E} = \{\Omega, \mathcal{Y}\}$ consisting of closed elements $\Omega = \{\Omega^i \subset \mathcal{D} : i = 1, \dots, I\}$ s.t.,

$$\mathcal{D} = \bigcup_{i=1}^I \Omega^i \quad \text{and} \quad \Omega^i = \mathcal{V}_i \quad \forall i = 1, \dots, I,$$

and, a set of storage locations $\mathcal{Y} = \{\mathbf{y}_k^i \in \mathcal{D} : i = 1, \dots, I; k = 1, \dots, n\}$, where, \mathbf{y}_k^i represents the location of the nodes in each element Ω^i , and n denotes the total number of nodes present in Ω^i . We chose Lagrangian elements where the nodes are defined as the points of intersection of the interfaces S_{ij} for $j \in \mathcal{J}_i$. We also define a set \mathcal{L}_k^i containing the indices of all elements sharing the k^{th} node associated with the i^{th} element, i.e.,

$$\mathcal{L}_k^i = \left\{ l := 0 \text{ for } \Omega^i, l \in \{0, 1, \dots, L-1\} : \bigcap_{l=0}^{L-1} \Omega_l = \mathbf{y}_k^i \right\}$$

where, L is the total number of elements sharing the node at \mathbf{y}_k^i . In our case, if $\mathcal{D} \subset \mathbb{R}^2$, then $L = 4$, and if $\mathcal{D} \subset \mathbb{R}^3$, then $L = 8$.

The finite element solution is stored at the nodes \mathbf{y}_k^i and the finite volume solution is stored at the center of mass \mathbf{x}_i of the coincident elements Ω^i and volumes \mathcal{V}_i .

Weak form

Let \mathcal{U} be the space of vector field $\mathbf{u} = \mathbf{u}(\mathbf{x}, t)$, representing the displacement at any time $t \geq 0$, $t \in \mathbb{R}$, such that,

$$\mathcal{U} = \left\{ \mathbf{u} : \mathcal{D} \rightarrow \mathbb{R}^d \mid \mathbf{u} \in \mathbf{H}^1(\mathcal{D}), \mathbf{u} = \bar{\mathbf{u}}(\mathbf{x}, t) \text{ for } \mathbf{x} \in \partial\mathcal{D}_D \right\},$$

and, let \mathcal{W} be the space of vector valued weighting functions \mathbf{w} , such that,

$$\mathcal{W} = \left\{ \mathbf{w} : \mathcal{D} \rightarrow \mathbb{R}^d \mid \mathbf{w} \in \mathbf{H}^1(\mathcal{D}), \mathbf{w} = 0 \text{ for } \mathbf{x} \in \partial\mathcal{D}_D \right\},$$

where, $\mathbf{H}^1(\mathcal{D})$ is the Sobolev space, representing the space containing all vector valued functions defined in the problem domain \mathcal{D} such that the function values and their weak first derivatives are square integrable.

We use the method of weighted residuals (or the Galerkin procedure) to construct a variational or weak form of our linear elasticity problem. We multiply the strong form (3.17) by a vectorial weight function $\mathbf{w} \in \mathcal{W}$, and integrate over the problem domain \mathcal{D} , as,

$$\int_{\mathcal{D}} \mathbf{w} \cdot (-\nabla \cdot \tilde{\boldsymbol{\sigma}}' - \mathbf{f}_b) \partial\mathbf{x} = 0.$$

Using Green's formula, we get,

$$\int_{\mathcal{D}} \nabla \mathbf{w} \cdot \tilde{\boldsymbol{\sigma}}' \partial\mathbf{x} = \int_{\mathcal{D}} \mathbf{w} \cdot \mathbf{f}_b \partial\mathbf{x} + \int_{\partial\mathcal{D}} \mathbf{w} \cdot \tilde{\boldsymbol{\sigma}}' \mathbf{n} \partial\mathbf{x}.$$

By virtue of the property of definite integrals requiring that the total be the sum of the parts, we can rewrite the above integral as a sum over the element domains, as,

$$\sum_i \int_{\Omega^i} \nabla \mathbf{w} \cdot \tilde{\boldsymbol{\sigma}}' \partial\mathbf{x} = \sum_i \int_{\Omega^i} \mathbf{w} \cdot \mathbf{f}_b \partial\mathbf{x} + \sum_i \int_{\partial\Omega^i \cap \partial\mathcal{D}} \mathbf{w} \cdot \tilde{\boldsymbol{\sigma}}' \mathbf{n} \partial\mathbf{x}.$$

Substituting the body forces, the constitutive law for stress, and imposing the boundary conditions, the weak form of the linear elasticity problem can now be stated as,

Problem: Given the domain \mathcal{D} and the finite element grid $\mathcal{E}(\Omega, \mathcal{Y})$,

find $\mathbf{u} \in \mathcal{U}$, such that,

$$\begin{aligned} & \sum_i \int_{\Omega^i} \frac{G}{2} (\nabla \mathbf{w} + \nabla^T \mathbf{w}) \cdot (\nabla \mathbf{u} + \nabla^T \mathbf{u}) \partial\mathbf{x} + \sum_i \int_{\Omega^i} \lambda (\nabla \cdot \mathbf{w}) (\nabla \cdot \mathbf{u}) \partial\mathbf{x} \\ &= \sum_i \int_{\Omega^i} \mathbf{w} \cdot \nabla P \partial\mathbf{x} + \sum_i \int_{\Omega^i} \mathbf{w} \cdot \rho \mathbf{g} \partial\mathbf{x} + \sum_i \int_{\partial\Omega^i \cap \partial\mathcal{D}_N} \mathbf{w} \cdot \bar{\mathbf{t}}_N \partial\mathbf{x} \end{aligned}$$

holds for all $\mathbf{w} \in \mathcal{W}$.

(3.19)

Finite element approximation

We approximate the displacement field \mathbf{u} over the domain \mathcal{D} using a piecewise linear $C^0(\mathcal{D})$ function defined over the finite element grid \mathcal{E} , s.t.,

$$\begin{aligned} \mathbf{u}(\mathbf{x}, t) &\approx \check{\mathbf{u}}(\mathbf{x}, t) = \sum_{i=1}^I \omega^i(\mathbf{x}) \check{\mathbf{u}}^i(\mathbf{x}, t) \\ \text{where, } \omega^i(\mathbf{x}) &= \begin{cases} 1 & \mathbf{x} \in \Omega^i \\ 0 & \mathbf{x} \notin \Omega^i \end{cases} \\ \text{and, } \check{\mathbf{u}}^i(\mathbf{x}, t) &= \sum_{k=1}^n \mathbf{N}_k(\mathbf{x}) \hat{\mathbf{u}}_k^i(t) = \mathbf{N}(\mathbf{x}) \hat{\mathbf{u}}^i(t), \end{aligned} \quad (3.20)$$

such that, $\hat{\mathbf{u}}_k^i(t)$ gives the displacement at the nodes located at position \mathbf{y}_k^i , and, the functions $\mathbf{N}_k(\mathbf{x})$ are $Q1$ -polynomial based *local shape functions* (or interpolation functions), with the following property,

$$\mathbf{N}_k(\mathbf{y}_l^i) = N_k(\mathbf{y}_l^i) \mathbf{I} = \begin{cases} \mathbf{I} & \text{if, } l = k, \\ \mathbf{0} & \text{if, } l \neq k, \end{cases} \quad \forall i.$$

It is clear that $\check{\mathbf{u}}^i(\mathbf{x}, t)$ denotes the approximate solution of the displacement field within the element Ω^i . The shape functions are defined such that the displacement field is continuous throughout the problem domain.

Note that in the weak form (3.19) we have to approximate the first derivative of P . For that we construct a C^0 -continuous approximation $\check{P}(\mathbf{x}, t) \in \mathcal{U}_p$ of P over the domain \mathcal{D} with

$$\mathcal{U}_p = \{p : \mathcal{D} \rightarrow \mathbb{R} \mid p \in H^1(\mathcal{D})\},$$

We approximate the effective pressure at a node \mathbf{y}_k^i , $i = 1, \dots, I; k = 1, \dots, n$, as a volume-weighted average of the finite volume solution for each cell associated with the node \mathbf{y}_k^i , i.e.,

$$\begin{aligned} \check{P}(\mathbf{x}, t) &= \sum_{i=1}^I \omega^i(\mathbf{x}) \check{P}^i(\mathbf{x}, t) \\ \text{where, } \check{P}^i(\mathbf{x}, t) &= \sum_{k=1}^n N_k(\mathbf{x}) \hat{P}_k^i(t) = N(\mathbf{x}) \hat{P}^i(t) \\ \text{and, } \hat{P}_k^i(t) &= \frac{\sum_{l=0}^{L-1} \bar{P}_i(t) |\mathcal{V}_l|}{\sum_{l=0}^{L-1} |\mathcal{V}_l|}, \quad \text{for } l \in \mathcal{L}_k^i. \end{aligned} \quad (3.21)$$

The values of the Lamé's parameters G and λ can, in principle, be discontinuous. Therefore, we directly use the values at the cell centers \mathbf{x}_i calculated using the finite volume solution at time t .

We use the standard Galerkin method (also called the Bubnov-Galerkin method), where, the weighting function is chosen the same as the basis function, i.e.,

$$\mathbf{w}(\mathbf{x}) = \sum_{i=1}^I \sum_{k=1}^n \omega^i(\mathbf{x}) \mathbf{N}_k(\mathbf{x}) \quad (3.22)$$

Substituting the approximate displacement field (3.20), the approximate effective pressure field (3.21), and the weight function (3.22) in the weak form (3.19), we get,

$$\begin{aligned} & \sum_i \int_{\Omega^i} \frac{G(\mathbf{x}_i, t)}{2} (\nabla \mathbf{N}(\mathbf{x}) + \nabla^T \mathbf{N}(\mathbf{x})) \cdot (\nabla \mathbf{N}(\mathbf{x}) + \nabla^T \mathbf{N}(\mathbf{x})) \hat{\mathbf{u}}^i(t) \partial \mathbf{x} \\ & + \sum_i \int_{\Omega^i} \lambda(\mathbf{x}_i, t) (\nabla \cdot \mathbf{N}(\mathbf{x})) (\nabla \cdot \mathbf{N}(\mathbf{x})) \hat{\mathbf{u}}^i(t) \partial \mathbf{x} - \sum_i \int_{\Omega^i} \mathbf{N}(\mathbf{x}) \cdot \nabla N(\mathbf{x}) \hat{P}^i(t) \partial \mathbf{x} \\ & = \sum_i \int_{\Omega^i} \mathbf{N}(\mathbf{x}) \cdot \rho(\mathbf{x}_i, t) \mathbf{g} \partial \mathbf{x} + \sum_i \int_{\partial \Omega^i \cap \partial \mathcal{D}_N} \mathbf{N}(\mathbf{x}) \cdot \bar{\mathbf{t}}_N \partial \mathbf{x}. \end{aligned} \quad (3.23)$$

Thus, we obtain a discrete-in-space problem given by the set of algebraic equations,

$$\boxed{\mathbf{K}_u(\mathbf{x}, t) \hat{\mathbf{u}}(t) - \mathbf{K}_p(\mathbf{x}, t) \hat{P}(t) = \mathbf{F}(\mathbf{x}, t)} \quad (3.24)$$

where, $\mathbf{K}_u(\mathbf{x}, t)$ and $\mathbf{K}_p(\mathbf{x}, t)$ are global stiffness matrices, and $\mathbf{F}(\mathbf{x}, t)$ is the global force vector given as,

$$\begin{aligned} \mathbf{K}_u(\mathbf{x}, t) &= \sum_i \int_{\Omega^i} \frac{G(\mathbf{x}_i, t)}{2} (\nabla \mathbf{N}(\mathbf{x}) + \nabla^T \mathbf{N}(\mathbf{x})) \cdot (\nabla \mathbf{N}(\mathbf{x}) + \nabla^T \mathbf{N}(\mathbf{x})) \partial \mathbf{x} \\ &+ \sum_i \int_{\Omega^i} \lambda(\mathbf{x}_i, t) (\nabla \cdot \mathbf{N}(\mathbf{x})) (\nabla \cdot \mathbf{N}(\mathbf{x})) \partial \mathbf{x} \\ \mathbf{K}_p(\mathbf{x}, t) &= \sum_i \int_{\Omega^i} \mathbf{N}(\mathbf{x}) \cdot \nabla N(\mathbf{x}) \partial \mathbf{x} \\ \text{and, } \mathbf{F}(\mathbf{x}, t) &= \sum_i \int_{\Omega^i} \mathbf{N}(\mathbf{x}) \cdot \rho(\mathbf{x}_i, t) \mathbf{g} \partial \mathbf{x} + \sum_i \int_{\partial \Omega^i \cap \partial \mathcal{D}_N} \mathbf{N}(\mathbf{x}) \cdot \bar{\mathbf{t}}_N \partial \mathbf{x}. \end{aligned}$$

The vectors $\hat{\mathbf{u}}(t)$ and $\hat{P}(t)$ contain all the nodal values of \mathbf{u} and P (with nodes numbered globally).

3.1.3 Time discretization: Implicit Euler method

We divide the time domain into N intervals, with t_n as the time at the n^{th} step, where $n \in \mathbb{N}$, $n = 0, \dots, N$, and $h_{n+1} = t_{n+1} - t_n$ as the time-step sizes. Let φ^n be the solution computed at time t_n .

We approximate the time derivative of variable φ using an implicit (or backward) Euler method. The implicit Euler method is a finite difference approximation based on a truncated Taylor series expansion of φ in the neighborhood of $t = t_{n+1}$, i.e.,

$$\varphi(t_{n+1} - h_{n+1}) \equiv \varphi^{n+1} = \varphi^n - h_{n+1} \left. \frac{\partial \varphi}{\partial t} \right|_{t_{n+1}} + O(h_{n+1}^2),$$

where, $O(h_{n+1}^2)$ is the order of the local truncation error (LTE) of the method. The implicit Euler method is a *first order technique*.

Using the above Taylor series expansion, we can now approximate the time derivatives appearing in the semi discrete form of the conservation laws, Eqn. (3.11), as,

$$\left. \frac{\partial \varphi}{\partial t} \right|_{t_{n+1}} = \frac{\varphi^{n+1} - \varphi^n}{h_{n+1}}. \quad (3.25)$$

Note that if the semi discrete form is expressed as, $\frac{\partial \varphi}{\partial t} = F(\varphi)$, then, in Eqn. (3.25),

$$\left. \frac{\partial \varphi}{\partial t} \right|_{t_{n+1}} = F(\varphi^{n+1}). \quad (3.26)$$

3.2 Iterative block Gauss-Seidel scheme

The space-time discrete model can be represented as a system of algebraic equations, as,

Flow block:

$$\mathbf{F}_1 : \mathbf{A}_1(\mathbf{X}^{n+1}, \mathbf{X}^n) \mathbf{X}_1^{n+1} - \mathbf{B}_1(\mathbf{X}^{n+1}, \mathbf{X}^n) = 0,$$

Geomechanical block:

$$\mathbf{F}_2 : \mathbf{A}_2(\mathbf{X}^{n+1}, \mathbf{X}^n) \mathbf{X}_2^{n+1} - \mathbf{B}_2(\mathbf{X}^{n+1}, \mathbf{X}^n) = 0,$$

Total-porosity block:

$$\mathbf{F}_3 : \mathbf{A}_3(\mathbf{X}^{n+1}, \mathbf{X}^n) \mathbf{X}_3^{n+1} - \mathbf{B}_3(\mathbf{X}^{n+1}, \mathbf{X}^n) = 0, \quad (3.27)$$

where, the vectors $\mathbf{X}_1 : \mathbb{R} \rightarrow \mathbb{R}^{d_f}$, $\mathbf{X}_2 : \mathbb{R} \rightarrow \mathbb{R}^{d_g}$ and $\mathbf{X}_3 : \mathbb{R} \rightarrow \mathbb{R}^{d_\phi}$ denote the discrete in space approximations at any given time step to the primary variables of the flow model (i.e. P_g, S_w, S_h, T), the geomechanical model (i.e. \mathbf{u}) and the total-porosity equation (i.e., ϕ), respectively. \mathbf{X} is the solution vector given as $\mathbf{X} = [\mathbf{X}_1 \ \mathbf{X}_2 \ \mathbf{X}_3]^T$. The indices n and $n + 1$ denote the solution at time t_n and t_{n+1} respectively.

We solve the discrete system (3.27) for \mathbf{X}^{n+1} in a *block-wise* manner.

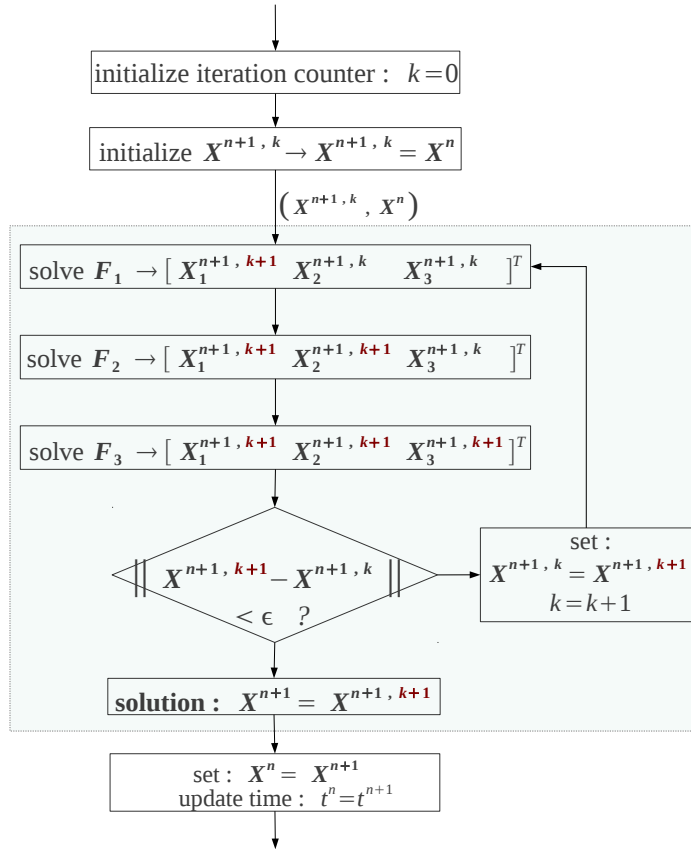


Figure 3.2: Block Gauss-Seidel *outer* iterative solution loop

The blocks \mathbf{F}_1 , \mathbf{F}_2 , and \mathbf{F}_3 are solved separately. Solution of the flow block \mathbf{F}_1 and the total-porosity block \mathbf{F}_3 requires, 1) linearization step using the Newton-Raphson method, and 2) solution of the linearized system using the SuperLU linear solver. These steps are repeated until convergence is achieved for \mathbf{X}_1^{n+1} and \mathbf{X}_3^{n+1} . This forms the *inner iterative loops*. The geomechanical block \mathbf{F}_2 is a linear system and is, therefore, solved directly.

The coupling between the blocks is introduced through a Gauss-Seidel scheme operating blockwise. This forms the *outer iterative loop*, as shown in Fig. 3.2. First, the flow block is solved and the solution vector \mathbf{X}^{n+1} is updated with the improved approximation of \mathbf{X}_1^{n+1} . Then, the geomechanical block is solved and the solution vector \mathbf{X}^{n+1} is updated with the improved approximation of \mathbf{X}_2^{n+1} , following which, the porosity block is solved and the solution vector \mathbf{X}^{n+1} is updated with the improved approximation of \mathbf{X}_3^{n+1} . These steps are repeated until convergence is achieved for \mathbf{X}^{n+1} .

In our algorithm, we generally control the number of iterations in the outer loop heuristically with the number of newton steps required for convergence of the flow block.

3.3 Multi-rate time stepping scheme

The concept of MRT methods was introduced for systems of differential equations (ODEs and DAEs) in such studies as [32, 35, 78], and some recent results are presented in [9, 22, 27, 50, 90]. MRT methods for conservative laws are developed in [21, 24, 102] and for parabolic equations in [89, 91]. A review of the MRT methods developed over the last two decades can be found in [31]. The application of MRT methods, especially the Implicit-Explicit methods (ImEx), is becoming increasingly popular in the PDE community. Some of the recent extensions of these methods to application areas of coupled free and porous media flows, air pollution modelling, multi-scale fluid-solid interaction, besides others, can be found in [85, 92, 113, 120, 106].

In our hydro-geomechanical hydrate reservoir model, we use two different ImEx based MRT algorithms to speed up our calculations. The first MRT algorithm is based on a *semi-implicit* approach and the second is based on a *compound-fast* approach. To understand the stability of these and related MRT methods in general, the reader is referred to [107].

We now summarize our MRT algorithms.

Let the vectors $\mathbf{X}_F(t) : \mathbb{R} \rightarrow \mathbb{R}^{d_f}$ and $\mathbf{X}_G(t) : \mathbb{R} \rightarrow \mathbb{R}^{d_g}$ denote the time-dependent discrete in space approximations to the primary variables of the **Flow** model (i.e. P_g, S_w, S_h, T) and the **Geomechanical** model (i.e. \mathbf{u}) respectively. We will refer to \mathbf{X}_F as the active components and \mathbf{X}_G as the latent components. Since changes in porosity are very small and depend predominantly on soil deformation, for simplicity, we chose to eliminate the soil-phase mass balance, PDE (2.3), by approximating the total porosity ϕ as a function of the volumetric strain ϵ_v , which is then solved only as a post process.

Further, let $\mathbf{F} : \mathbb{R} \times \mathbb{R}^d \times \mathbb{R}^{d_f} \times \mathbb{R}^{d_g} \rightarrow \mathbb{R}^{d_f}$ and $\mathbf{G} : \mathbb{R} \times \mathbb{R}^d \times \mathbb{R}^{d_f} \times \mathbb{R}^{d_g} \rightarrow \mathbb{R}^{d_g}$ denote the spatial discretization operators for the **Flow** and the **Geomechanical** models respectively. Here, d is the dimension of the space domain. In our numerical scheme, the operator \mathbf{F} is obtained by assembling the spatially discretized conservation laws, Eqn. (3.11), for the flow model, and the operator \mathbf{G} is given by Eqn. (3.24).

The spatial discretization of the PDEs governing our hydro-geomechanical model leads to a semi-discrete problem of the following form:

Problem: For $t \in [0, T]$, given the initial conditions

$$\mathbf{X}_F(t=0) = \mathbf{X}_F^0 \text{ and } \mathbf{X}_G(t=0) = \mathbf{X}_G^0,$$

find solutions for \mathbf{X}_F and \mathbf{X}_G which satisfy

$$\partial_t \mathbf{X}_F = \mathbf{F}(t, \mathbf{x}, \mathbf{X}_F, \mathbf{X}_G) \tag{3.28}$$

$$\mathbf{0} = \mathbf{G}(t, \mathbf{x}, \mathbf{X}_F, \mathbf{X}_G) \tag{3.29}$$

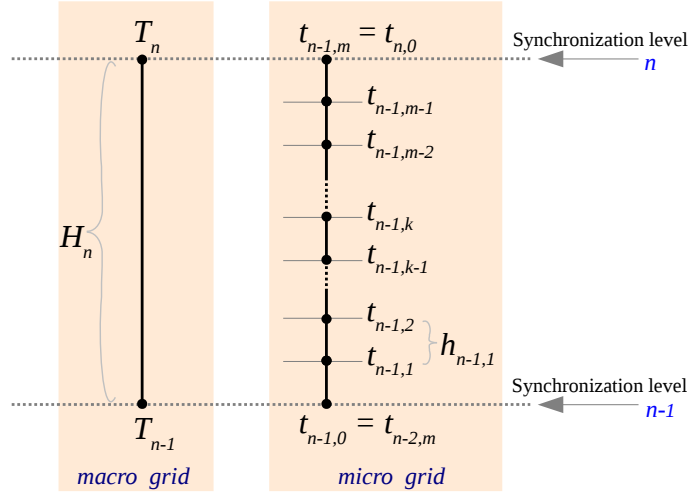


Figure 3.3: Time-mesh for active and latent components

Eqn.(3.28) is the active ODE (Ordinary Differential Equation) system and Eqn.(3.29) is the latent AE (Algebraic Equations) system. Together, they form a naturally partitioned multi-scale DAE (Differential Algebraic Equations) system.

Each part of the partitioned DAE system is marched in time on an independent time-mesh which depends on its own activity. We assume that the activity of the components does not vary in space. For the latent system, we define a coarse time-mesh $\{T_n, 0 \leq n \leq N\}$ with time step sizes $\{H_n = T_n - T_{n-1}, 0 < n \leq N\}$. We will refer to this as the macro-grid, and the time step from T_{n-1} to T_n as the macro-step. For the active system, we define a refined time-mesh $\{t_{n,k}, 0 \leq n < N, 0 \leq k \leq m\}$ with time step sizes $\{h_{n,k} = t_{n,k} - t_{n,k-1}, 0 \leq n < N, 0 < k \leq m\}$ and multirate factor m . We will refer to this as the micro-grid, and the time step from $t_{n-1,k-1}$ to $t_{n-1,k}$ for each $k = [1, \dots, m]$ as the micro-steps. The two time-meshes are synchronized, which implies that for all n , $T_n = t_{n,0} = t_{n-1,m}$ (See Fig. 3.3).

All MRT methods have the basic property that the time integration can proceed from synchronization level n to $n+1$ only when all the components, slow and fast, have made their respective macro and micro steps and have synchronized at the level n .

For marching the DAE system (3.28,3.29) forward in time from T_{n-1} to T_n , the active ODE (3.28) is integrated on the micro grid $t_{n-1,k}$ using the implicit Euler method for each micro step, while the latent AE (3.29) is evaluated directly at the macro grid point T_n using the solution of the active ODE at $t_{n-1,m}$. The two MRT algorithms that we will discuss differ in how the latent components are approximated on the micro grid for solving the active ODE.

In the semi-implicit MRT method (**Algorithm 1**), we first make the m micro steps for the active components from $t_{n-1,0}$ to $t_{n-1,m}$. The values of the latent components needed on the micro

grid, i.e. $\mathbf{X}_{G_{n-1,k}}$, for making the micro steps are approximated by means of extrapolation. In our scheme, we construct a polynomial function of order p for extrapolation using the values of \mathbf{X}_G evaluated at $p + 1$ previous macro grid points, i.e., $T_{n-1}, \dots, T_{n-(p+1)}$. We then make the final macro step to evaluate the latent component at T_n .

For $m = 1$, this method essentially becomes a decoupled sequential solution scheme, which by itself is faster than the iteratively coupled solution scheme. For $m \geq 1$, all systems are solved only once on their respective time-meshes, and the coefficients of the extrapolation function also need evaluation only once per macro step, thus requiring very little computational effort.

ALGORITHM 1: Semi-implicit MRT method.

STEP 1: Extrapolation macro step

Extrapolate $\mathbf{X}_{G_{n-1,k}}$ at each $k = [1, \dots, m]$ on the fine time-mesh using the $p + 1$ old step values of \mathbf{X}_G computed at $T_{n-1}, \dots, T_{n-(p+1)}$:

$$\tilde{\mathbf{X}}_{G_{n-1,k}} = \mathbf{X}_{G_{n-1}} + \sum_{j=1}^p A_j (t_{n-1,k} - T_{n-1})^j \quad (3.30)$$

STEP 2: Micro-steps

Solve for $\mathbf{X}_{F_{n-1,k}}$ at each $k = [1, \dots, m]$ on the fine time-mesh using the implicit Euler method:

$$\begin{aligned} \mathbf{X}_{F_{n-1,k}} &= \mathbf{X}_{F_{n-1,k-1}} \\ &+ h_{n-1,k} \mathbf{F} \left(t_{n-1,k}, \mathbf{x}, \mathbf{X}_{F_{n-1,k}}, \tilde{\mathbf{X}}_{G_{n-1,k}} \right) \end{aligned} \quad (3.31)$$

STEP 3: Macro-step

Solve for \mathbf{X}_{G_n} :

$$\mathbf{G} (T_n, \mathbf{x}, \mathbf{X}_{F_{n-1,m}}, \mathbf{X}_{G_n}) = 0. \quad (3.32)$$

In the compound-fast MRT method (**Algorithm 2**), we first make a predictor macro step to get an approximate value of the latent component at T_n . In this step, we integrate the active ODE on the macro grid from T_{n-1} to T_n with a relaxed stopping criteria for the Newton solver. This gives a rough approximation of \mathbf{X}_F at T_n (denoted by $\tilde{\mathbf{X}}_{F_n}$), which is then used to solve the latent AE to get an approximate value of \mathbf{X}_G at T_n (denoted by $\tilde{\mathbf{X}}_{G_n}$). We then make the micro steps to integrate the active ODE from $t_{n-1,0}$ to $t_{n-1,m}$. The values of the latent components needed on the micro grid, i.e. $\mathbf{X}_{G_{n-1,k}}$, for making the micro steps are approximated by means of linear interpolation (refer Eqn.(3.36)). In the final step, called the corrector macro step, we solve the latent AE once more at the macro grid point T_n to correct (improve) the solution from the predictor step.

If the ODE becomes unsolvable on the macro grid and the predictor step fails, then, in our simulator we reduce the value of H_n by half and attempt the predictor step once again.

ALGORITHM 2: Compound-fast MRT method

STEP 1: Predictor macro step (or compound step)

Integrate active ODE (3.28) with large step size H_n . Relax the stopping criteria for the Newton solver to get a rough approximation at T_n , $\tilde{\mathbf{X}}_{F_n}$:

$$\tilde{\mathbf{X}}_{F_n} = \mathbf{X}_{F_{n-1}} + H_n \cdot \mathbf{F} \left(T_n, \mathbf{x}, \tilde{\mathbf{X}}_{F_n}, \mathbf{X}_{G_{n-1}} \right) \quad (3.33)$$

Use $\tilde{\mathbf{X}}_{F_n}$ to predict $\tilde{\mathbf{X}}_{G_n}$:

$$\mathbf{G} \left(T_n, \mathbf{x}, \tilde{\mathbf{X}}_{F_n}, \tilde{\mathbf{X}}_{G_n} \right) = 0. \quad (3.34)$$

STEP 2: Micro-steps

Solve for $\mathbf{X}_{F_{n-1,k}}$ at each $k = [1, \dots, m]$ on the fine time-mesh using implicit Euler method:

$$\begin{aligned} \mathbf{X}_{F_{n-1,k}} &= \mathbf{X}_{F_{n-1,k-1}} \\ &+ h_{n-1,k} \mathbf{F} \left(t_{n-1,k}, \mathbf{x}, \mathbf{X}_{F_{n-1,k}}, \tilde{\mathbf{X}}_{G_{n-1,k}} \right) \end{aligned} \quad (3.35)$$

where, $\tilde{\mathbf{X}}_{G_{n-1,k}}$ are the linearly interpolated values of \mathbf{X}_G at $t_{n-1,k}$:

$$\tilde{\mathbf{X}}_{G_{n-1,k}} = \mathbf{X}_{G_{n-1}} + \left(\tilde{\mathbf{X}}_{G_n} - \mathbf{X}_{G_{n-1}} \right) \sum_{i=1}^k \frac{h_{n-1,i}}{H_n} \quad (3.36)$$

STEP 3: Corrector macro step

Solve for \mathbf{X}_{G_n} :

$$\mathbf{G} \left(T_n, \mathbf{x}, \mathbf{X}_{F_{n-1,m}}, \tilde{\mathbf{X}}_{G_n} + \Delta \mathbf{X}_{G_n} \right) = 0. \quad (3.37)$$

The performance of the presented MRT schemes, in terms of accuracy and speed-up, is evaluated in Chapter 5 through a 1D consolidation test problem. The advantage of these MRT schemes in terms of speed-up for performing 3D calculations is shown in Section 6.3.

Model verification

The mathematical model described in Chapter 2 consists of three important parts that are specific to the gas-production from stimulated gas hydrate reservoirs. These are the methane hydrate *dissociation kinetics*, the *poroelasticity coupling*, and the *kinetics-poroelasticity coupling*. In this chapter, we present numerical tests where we isolate these model components and couplings in our hydrate reservoir model, and verify them one by one.

In *Test 1*, Section 4.1, we verify the dissociation kinetics model. We simulate the methane gas production in $1D$ and $2D$ lab-scale experiments on hydrate dissociation via depressurization by Tang et al. (2007) [103] and Yuhu et al. (2009) [8], respectively. In these experiments, the geo-mechanical effects are negligible and reaction kinetics dominates over fluid flow, thus, effectively isolating dissociation kinetics from the other processes. Through this test, we ensure that our hydrate kinetics model can effectively capture the gas production behaviour and the pressure profiles.

In *Test 2*, Section 4.2, we verify the coupling between the hydrate kinetics model and the two-phase fluid flow in the porous media. We simulate an artificial setting similar to the five-spot problem in a diagonal flow configuration, with the addition of a gas source in the form of a dissociating block of hydrate located in the center of a unit square domain which is initially saturated with water. The domain is depressurized using a *water outflux* boundary condition prescribed at the *gas well* located at lower left corner of the domain. The diagonally opposite end is held at a constant pressure. The water outflow is expected to destabilize the hydrate block, causing it to dissociate. The released gas must then get drawn towards the low pressure zone created by the gas well. Through this test, we ensure a correct implementation of the convection, diffusion, and the reaction terms in our numerical scheme.

In *Test 3*, Section 4.3, we verify the poro-elasticity coupling. We ignore the hydrates in the porous medium, thus reducing the model to a simple two phase hydro-mechanical system. We consider a classical $1D$ consolidation problem by Terzaghi (1925) [104] to test the fluid pressure

response generated by the mechanical compression of the soil. For benchmarking, we simulate the problem setting described by Kolditz et al. (2012) [48], and compare our numerical results with the analytical solution. Through this test we ensure a correct implementation of the poroelastic coupling in our hydrate reservoir model.

Finally, in *Test 4*, Section 4.4, we verify the kinetics-poroelasticity coupling, which is essentially the most important coupling for capturing the hydro-chemo-geomechanical response of a hydrate reservoir. We extend Terzaghi's $1D$ consolidation problem to include hydrate kinetics in the poroelastic coupling. We simulate a test problem where an axially loaded hydrate bearing sand sample experiences a spontaneous shift in the hydrate stability curve causing the hydrate to melt. For this problem, we present an analytical solution for pore-pressure response, which we subsequently use to test the accuracy of our numerical results.

4.1 Test 1: Verification of dissociation kinetics model

We consider $1D$ and $2D$ experiments on hydrate dissociation by depressurization by Tang et al. (2007) [103] and Yuhu et al. (2009) [8], respectively.

4.1.1 1D experiment

Experimental set-up

A cylindrical, stainless steel cell with internal diameter of 38 mm and length of 500 mm was used as the main pressure vessel. The cell was jacketed with an insulating, impermeable layer and was immersed in an air-bath. During each experimental run, the dry sands were sieved into size range of $300 - 450 \mu m$ and were pushed tightly into the vessel, resulting in a sediment with porosity of 33% and a permeability of 300 mdarcy.

The sediment was saturated with distilled water, and the methane hydrate was formed in-situ by slowly injecting methane gas at a pressure higher than the equilibrium pressure. The hydrate was formed in two stages to obtain a homogeneous distribution.

To perform the dissociation experiment, the back pressure regulator was set to a pressure lower than the hydrate equilibrium pressure at the working temperature, and the outlet valve was opened quickly. The gas released through the outlet valve was continuously recorded and a *cumulative gas-production curve* was plotted.

Numerical simulation

A schematic of the test domain for this experiment is shown in Fig. 4.1. The domain is discretized into 100 cells along the X -axis and the simulation is performed in $1D$. The geo-mechanical block is switched off and only the flow-transport block is solved. Gravity is neglected. The *depressurization* (i.e. back pressure regulation) is considered at the left boundary. The left

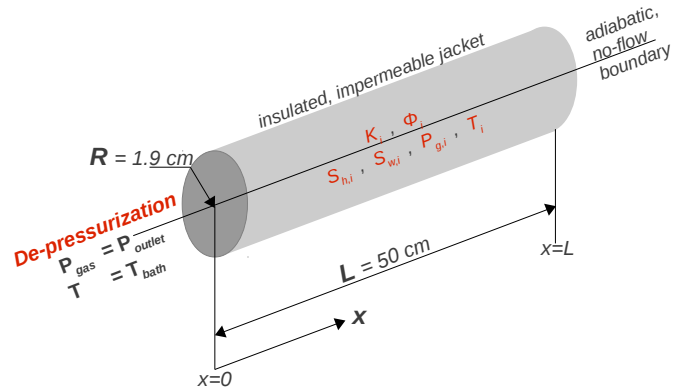


Figure 4.1: Test 1 - Test setting for 1D experiment

Table 4.1: Test 1 - Initial conditions for 1D experiment

ICs	Run 2	Run 3
$P_{g,i}$ [MPa]	3.535	3.584
T_i [$^{\circ}C$]	1.54	2.08
$S_{w,i}$ [%]	29.61	19.25
$S_{h,i}$ [%]	21.83	25.44
K_i [mD]	300	300
ϕ_i [%]	30.8	30.8

Table 4.2: Test 1 - Boundary conditions for 1D experiment

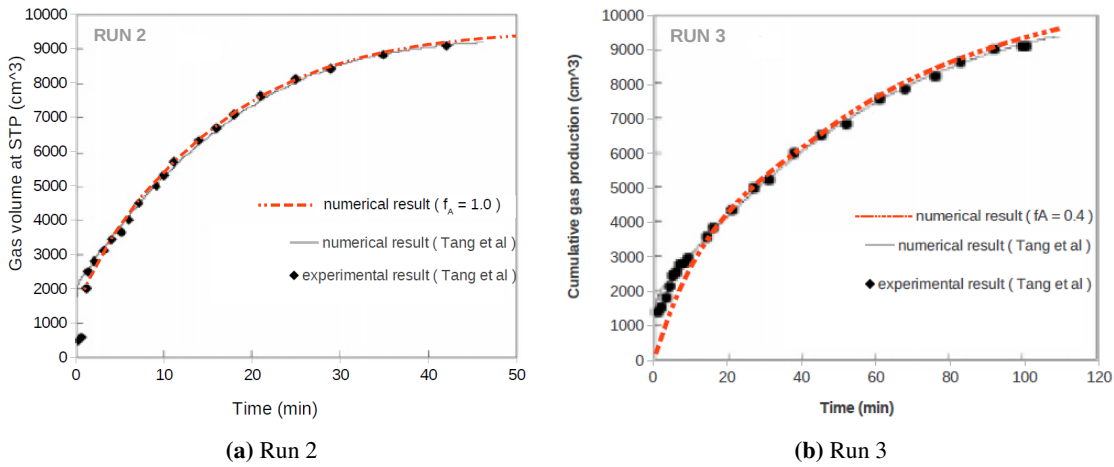
at $x = 0, t > 0$	Run 2	Run 3
P_{outlet} [MPa]	0.93	1.94
T_{bath} [$^{\circ}C$]	1.54	2.08
at $x = L, t > 0$		
$\dot{m}_g = 0$		
$\dot{m}_w = 0$		
$\nabla T = 0$		

boundary also serves as the *gas outlet*. Two depressurization modes have been considered for this test. In the first (*Test-ID:Run2*), the pressure is decreased from 3.535 MPa to 0.93 MPa at $T_{bath} = 1.54^{\circ}C$. In the second (*Test-ID:Run3*), the pressure is decreased from 3.584 MPa to 1.94 MPa at $T_{bath} = 2.08^{\circ}C$. The total dissociation process for *Run2* and *Run3* was reported by Tang et al. to last 40 and 110 minutes respectively. So, the t_{end} for the numerical simulations was chosen accordingly. The initial and boundary conditions are listed in Table 4.1 and Table 4.2, respectively.

Tang et al. (2007) used TOUGH-Fx/Hydrate to simulate the experimental data. The value of the intrinsic rate constant k_d^0 , as reported by Tang et al., was back calculated to fit the experimental data. We have used the same method to calibrate our model and obtain the best value of k_d^0 for each depressurization mode (*Run2* and *Run3*). The resulting values for kinetic-parameters $\Delta E_a/R$ and k_d^0 are listed and compared in Table 4.3. "reported" refers to the values reported by Tang, and "fitted" refers to the values obtained from our calculations. Also, since the parameterization for P_{eqb} was not reported by Tang et al., we have used the standard relationship proposed by Kamath and Holder [43] for pure methane dissolved in distilled water.

Table 4.3: Test 1 - Kinetic parameters for 1D experiment

	$\Delta E_a/R$	k_d^0
	[K]	$\left[\frac{\text{mol}}{\text{m}^2 \cdot \text{Pa} \cdot \text{s}} \right]$
Run 2 (reported)	9400	1.7×10^4
Run 2 (fitted)	9400	1.7×10^4
Run 3 (reported)	9400	1.4×10^4
Run 3 (fitted)	9400	0.8×10^4

**Figure 4.2:** Test 1 - Cumulative gas production curves for 1D experiment (comparison with Tang et al. (2007)). Here, $f_A = \frac{\text{fitted } k_d^0}{\text{reported } k_d^0}$.

Results

Fig. 4.2a and Fig. 4.2b show the comparison between cumulative gas volume curves obtained experimentally and numerically for *Run2* and *Run3*, respectively. Our numerical results show that the kinetics hydrate phase change model in our hydrate reservoir model is capable of capturing the gas production behaviour of a dissociating gas hydrate sample.

4.1.2 2D experiment

The experimental set-up for hydrate formation and dissociation processes used in this experiment are very similar to the 1D experiment by Tang et al. described above. The main difference is the *sample geometry*, which is cylindrical in the 1D case and square wafer-like in this case. Reaction kinetics is essentially only a time dependent process, and the number of spatial dimensions do not directly affect the kinetics. However, testing the kinetics model in both 1D and

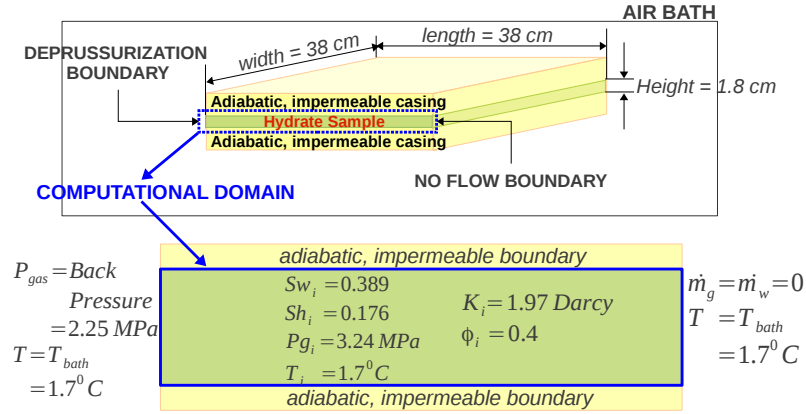


Figure 4.3: Test 1 - Test setting for 2D experiment

Table 4.4: Test 1 - Kinetic parameters for 2D experiment

$\frac{\Delta E_a}{R}$	[K]	9752.73
k_d^0	$\left[\frac{\text{mol}}{\text{m}^2 \cdot \text{Pa} \cdot \text{s}} \right]$	3.6×10^4
\dot{Q}_h	$\left[\frac{\text{J}}{\text{kg}} \right]$	$-1050 T + 3527000$

2D geometries ensures that the spatial coupling between the different model components are correctly resolved, and that no spurious spatial effects manifest in the simulation of dissociation process.

Experimental set-up

The hydrate formation and dissociation unit was a stainless steel vessel with length, width, and thickness of 380 mm, 380 mm, and 18 mm respectively, and was immersed in an air-bath. The procedure for sand sample preparation and in-situ hydrate formation were similar to that described in Sec. 4.1.1. The resulting sediment porosity and permeability were 40% and 1.97 Darcy, respectively, and the hydrate saturation was 17.6%.

To perform the dissociation experiment, the back pressure was reduced from an initial pressure of 3.24 MPa to 2.25 MPa, and the outlet valve was opened quickly. The bath temperature was maintained at 1.7^0C . The gas released through the outlet valve was continuously recorded and a gas production rate was plotted.

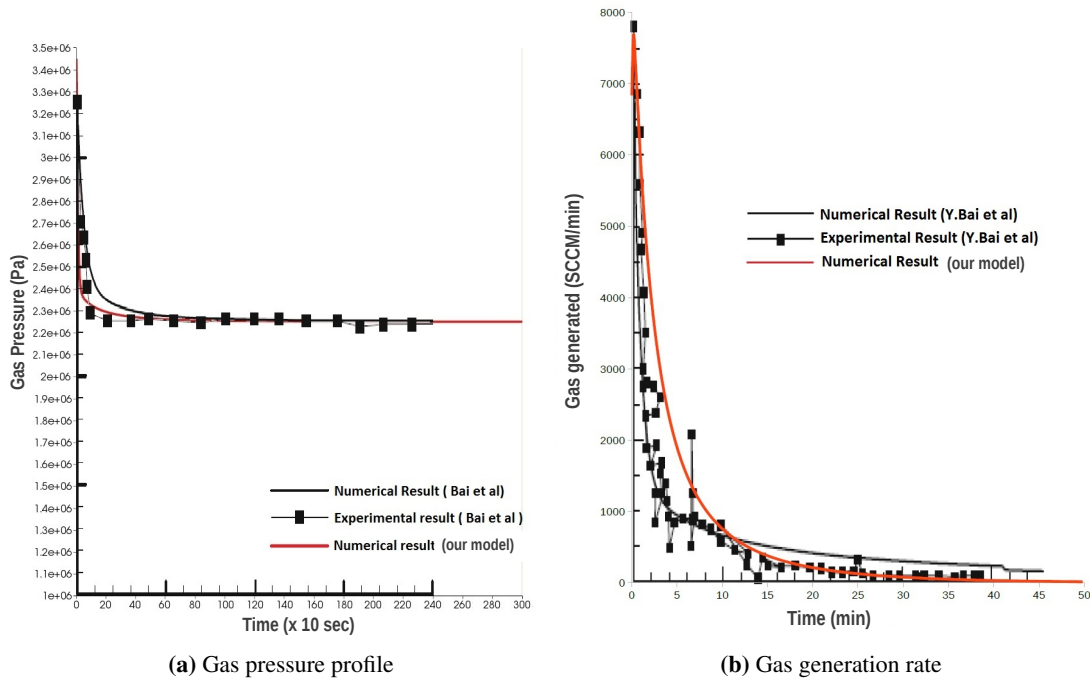


Figure 4.4: Test 1 - Results for 2D experiment (comparison with Yuhu et al. (2009))

Numerical simulation

A schematic of the test domain for this experimental set up along with the initial and boundary conditions are shown in Fig. 4.3. The domain is discretized in 10×100 cells, and the simulations are performed in 2D. The geo-mechanical block is switched off and only the flow-transport block is solved. Gravity is neglected. Depressurization and gas outlet are prescribed at the left boundary. The reaction-kinetics parameters are listed in Table 4.4.

Results

Fig. 4.4b and Fig. 4.4a show the experimental and numerical comparisons of the gas generation rate and the gas pressure for this setting. Our numerical results are in good agreement with the experimentally recorded values and show that the kinetics model in our hydrate reservoir model is capable of reproducing the hydrate dissociation and gas production behaviour observed in the experiments, especially towards steady state.

4.2 Test 2: Verification of three-phase hydrate model

In this section, we test the coupling between the kinetics model and the two phase flow model in our numerical scheme.

For this, we use an artificial setting similar to the five-spot problem, with the addition of a gas source in the domain in the form of a dissociating block of hydrate. This test ensures a correct implementation of the convection, diffusion, and the reaction terms in the 2D numerical scheme. It also ensures that the numerical scheme does not produce any spurious grid-based effects.

Problem set-up

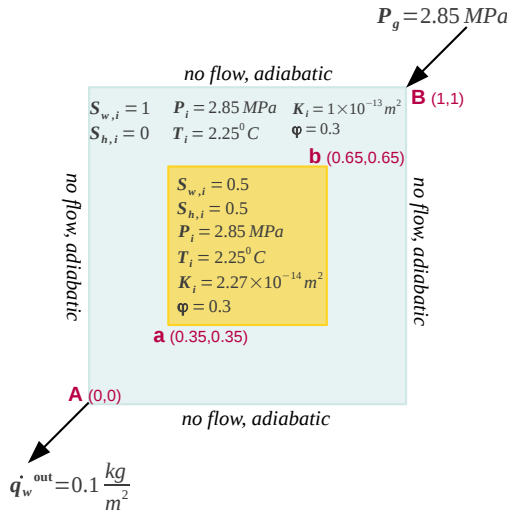


Figure 4.5: Test 2 - Test setting

A schematic of the test domain is shown in Fig. 4.5. The domain is a unit square with a $0.3\text{m} \times 0.3\text{m}$ hydrate block located in the center. The domain is initially saturated with water. The hydrate saturation in the block is 50%. Point A at $(0, 0)$ is the gas well. *Neumann water-outflux* B.C. is prescribed at A. The diagonally opposite point B at $(1, 1)$ is held constant at initial pressure. The rest of the domain boundaries are closed and adiabatic. The depressurization caused by water outflow at A is expected to destabilize the hydrate block causing it to dissociate. The released gas must then get drawn towards the low pressure in the gas well at point A.

Numerical simulation

For this problem, the geomechanical block is switched off and only the flow-transport block is solved. The initial and the boundary conditions for the problem are specified in Fig. 4.5. The hydraulic properties, hydrate stability curve parameters, and the dissociation kinetics parameters used in the numerical simulation are listed in Table 4.5. The end-time for this problem is chosen as $t_{end} = 500$ minutes. For the base test (*run0*), the domain is discretized uniformly into 20×20 cells. The time-step size is kept constant at 120 seconds. To check the mesh dependency of the numerical scheme, the mesh is successively halved, i.e. $(\Delta x)_{run1} = \frac{1}{2} (\Delta x)_{run0}$, $(\Delta x)_{run2} = \frac{1}{2} (\Delta x)_{run1}$, and $(\Delta x)_{run3} = \frac{1}{2} (\Delta x)_{run2}$. The time-step size is also successively halved so that $\Delta x / \Delta t$ ratio remains constant for each of the test-runs.

Results

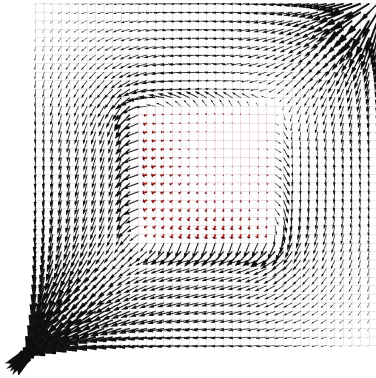
The gas plume takes about 300 minutes to reach the gas well at A. Fig. 4.6 shows the screenshots of gas saturation in the domain at 100, 200, and 300 minutes. Fig. 4.7 shows the line-plot

Table 4.5: Test 2 - Model parameters

Brooks-Corey parameters	
P_{entry} [Pa]	5000
λ_{BC}	1.5
Hydrate stability curve	
P_{eqb} [Pa]	$A_1 = 1000, A_2 = 38.980, A_3 = 8533.80$ if $T > 273.15$
	$A_1 = 1000, A_2 = 14.717, A_3 = 1886.79$ if $T \leq 273.15$
Dissociation kinetics parameters	
$\Delta E_a/R$ [K]	9400
k_d^0	3.6×10^4
	$\left[\frac{\text{mol}}{\text{m}^2 \cdot \text{Pa} \cdot \text{s}} \right]$

of S_g at 200 and 300 minutes along the diagonal aligned with flow direction, i.e. line $X - Y = 0$.

In Fig. 4.7a the solution shows convergence with mesh-refinement. The flow in the right half of the domain (i.e. $Y + X - 1 > 0$) is diffusion dominated, whereas, that in left half (i.e. $Y + X - 1 < 0$) is convection dominated being strongly influenced by the low pressure in the gas well. The gas front is more diffusive on a coarse mesh, but gets sharper as refinement is increased. Fig. 4.7b shows the saturation of the gas plume that reaches the gas well at 300 minutes.

**Figure 4.9:** Test 2 - \mathbf{v}_g profile (at $t = 30$ minutes)

Red vectors represent \mathbf{v}_g in the hydrate zone
Black vectors represent \mathbf{v}_g in hydrate free zone.

Clearly visible in Fig. 4.8a and Fig. 4.8b which show the S_g profiles along X-axis (at $Y = 0.5$ m) at times $t = 300$ min and $t = 500$ min respectively. The pressure in the right half along the X-axis is higher than that in the left half, causing \dot{g}^{CH_4} to be lower in the right half. Therefore, the extent of gas depletion is higher in the right half of the hydrate zone.

Note that in Fig. 4.7a and Fig. 4.7b, what appears to be a *kink* in gas saturation at the corner of the hydrate zone is *not* a numerical artifact. This *kink* is caused because of the following physical effects: the gas velocity in the hydrate free zone is higher than that in the hydrate zone (due to difference of almost an order of magnitude in the permeabilities) (See Fig. 4.9). This causes the gas to be sucked out of the hydrate zone faster than the time required by gas to equilibrate inside the hydrate zone. So, the gas begins to *deplete* along the edges of the hydrate zone. Further, the extent of the depletion is higher where \dot{g}^{CH_4} is lower (i.e., where P_g is higher). This effect is more

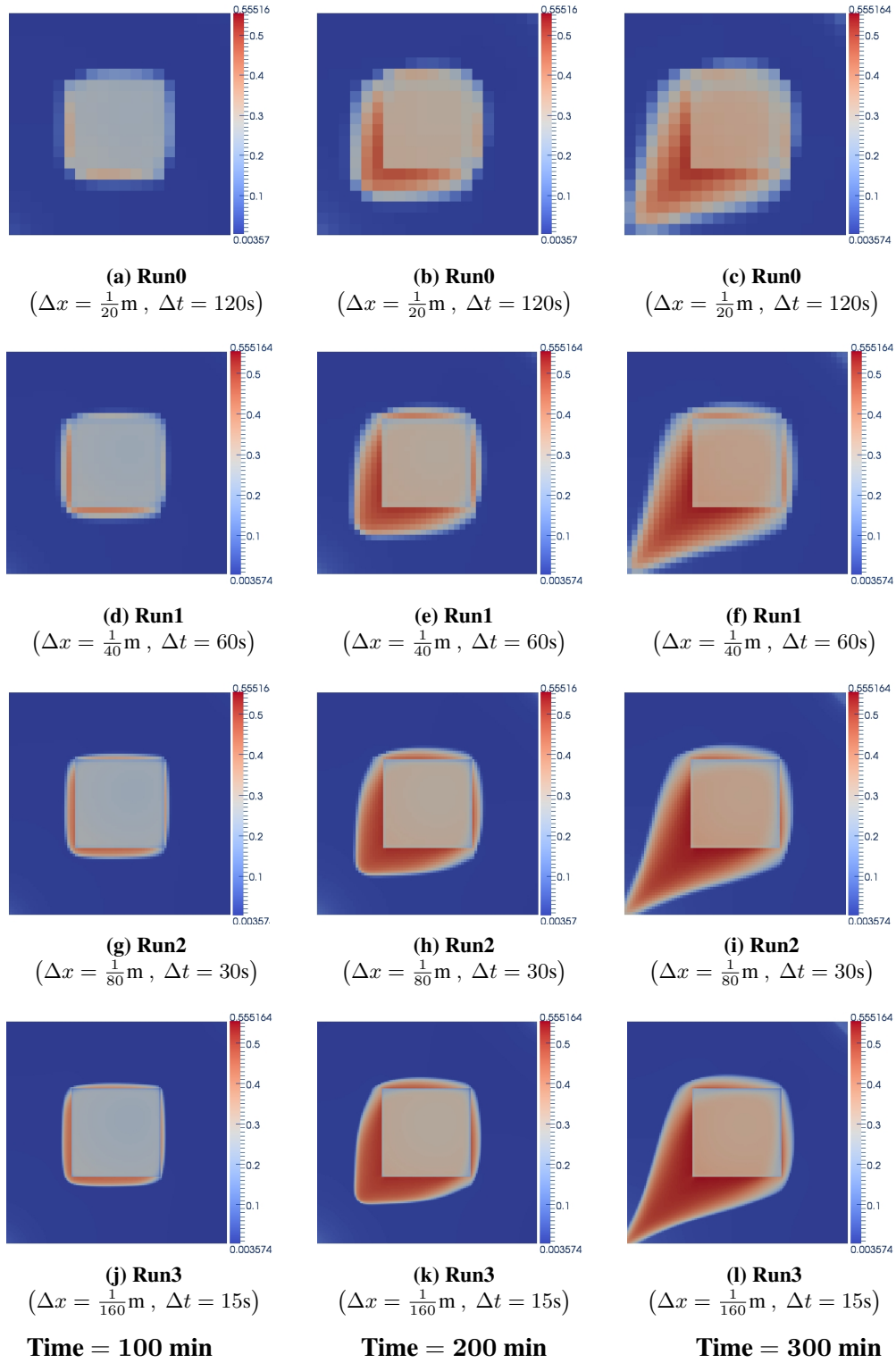
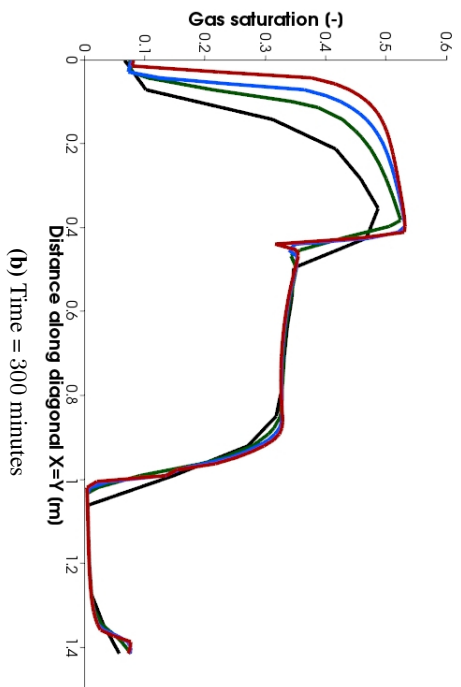
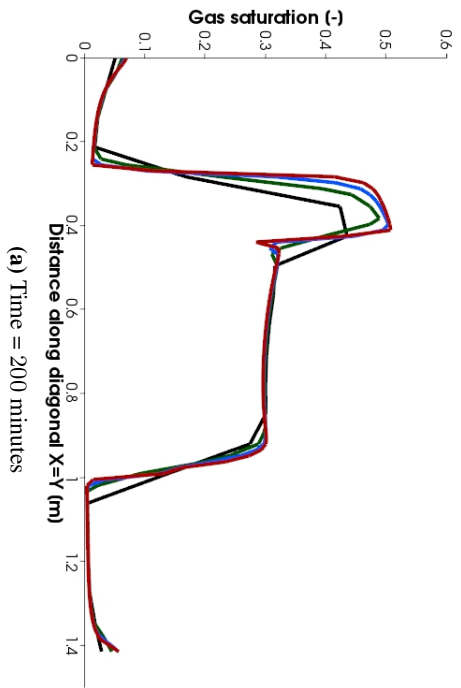


Figure 4.6: Test 2 - S_g profile



Legend:

- ref=1, — ref=2, — ref=4, — ref=8

Figure 4.7: Test 2 - S_g profile along diagonal line $X = Y$.

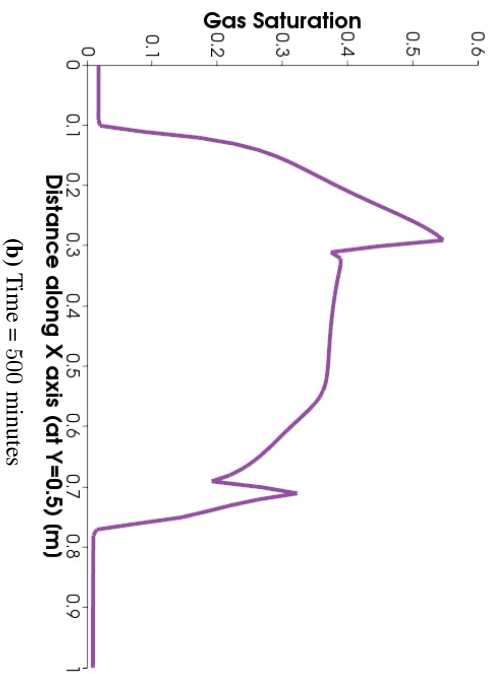
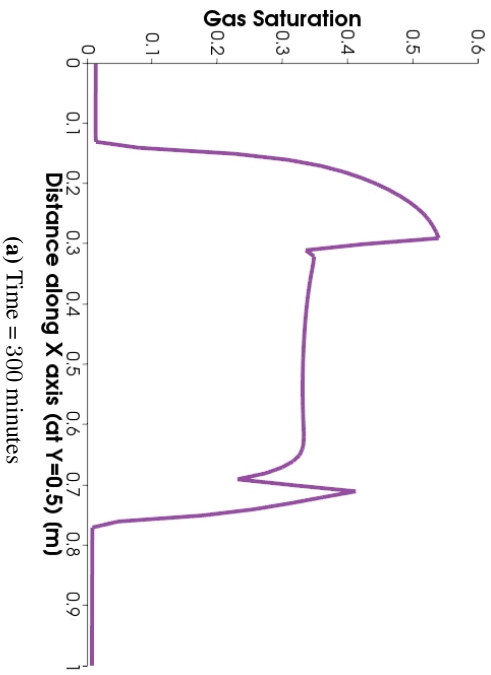


Figure 4.8: Test 2 - S_g profile along X-axis (at $Y = 0.5$ m)

4.3 Test 3: Verification of poroelasticity coupling

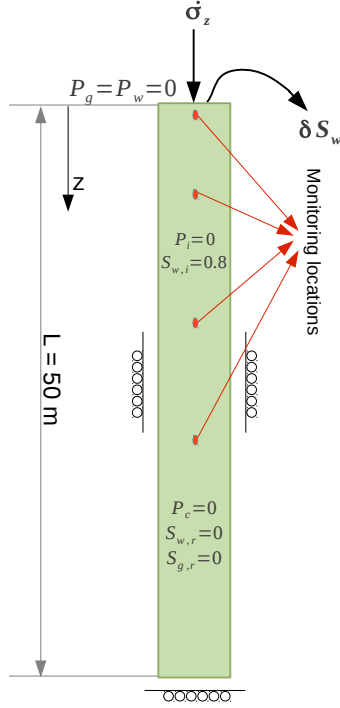


Figure 4.10: Test 3 - Terzaghi problem Schematic

In this example we ignore the methane hydrates in the medium, thus reducing the model to a simple two-phase hydro-mechanical system. We consider the classical 1D consolidation problem by Terzaghi [104] to test the fluid pressure response generated by the mechanical compression of the soil. This test was originally formulated by Terzaghi for analyzing the time delay observed when compressing clay layers and is now considered as a standard benchmark test for the coupling relationships between fluid and mechanical systems.

Problem statement

The problem set-up consists of a confined soil sample surrounded by a circular ring and placed in a container filled with water. The sample is loaded by a constant or ramped vertical stress at its upper surface, and the deformation is measured. The lower boundary is impermeable, and the upper boundary is fully drained. This is called a *confined compression test* or an *oedometer test*. Fig. 4.10 shows a schematic for this problem. It is expected that the compression of a soil sample will be accompanied by an expulsion of pore fluids from

the sample. Also, if the soil permeability is low, this may take considerable time. In Terzaghi's original work, the pore fluid and the soil particles were both assumed to be incompressible, so that the only mechanism of deformation was a rearrangement of the particles. However, Biot's more generalized consolidation framework, which is also the basis of our poroelasticity model, accounts for both fluid and soil compressibilities. So, in the further discussion, the fluid and the soil are treated as compressible mediums.

The mathematical description of such a problem in 1D reduces to a fluid diffusion equation of hydrogeology,

$$\partial_t \bar{P} - c \frac{\partial^2 \bar{P}}{\partial z^2} = 0 \quad (4.1)$$

where, \bar{P} is the mean fluid pressure given by $\bar{P} = S_w P_w + S_{nw} P_{nw}$, and c is 1-D fluid diffusivity.

Table 4.6: Test 3 - Terzaghi problem
Solid-matrix properties

Property	Symbol	Unit	Value
Drained bulk modulus	B_s	GPa	8.0
Poisson ratio	ν	-	0.20
Porosity	ϕ	-	0.19
Permeability	K	m^2	1.9×10^{-13}
Biot constant	α	-	0.8

Table 4.7: Test 3 - Terzaghi problem
Fluid properties

Property	Symbol	Unit	Value
<i>Wetting fluid</i>			
Bulk modulus	B_w	GPa	2.933
Density	ρ_w	$\frac{kg}{m^3}$	997.05
Viscosity	μ_w	$Pa \cdot s$	8.9008×10^{-4}
<i>Non-wetting fluid</i>			
Bulk modulus	B_{nw}	GPa	1.187
Density	ρ_{nw}	$\frac{kg}{m^3}$	997.05
Viscosity	μ_{nw}	$Pa \cdot s$	8.9008×10^{-4}

For a vertical load σ_{zz} ramped linearly at the top boundary at a rate $d\sigma_{zz}/dt = \dot{\sigma}_z$, the analytical solution for the pore pressure response is given as,

$$\frac{\bar{P}(z,t)}{\bar{P}_0} = 1 - \left(\frac{L-z}{L}\right)^2 - \frac{32}{\pi^3} \sum_{m=0}^{\infty} \left(\frac{-1^m}{(2m+1)^3} e^{(-\psi^2 ct)} \cos[\psi(L-z)] \right) \quad (4.2)$$

where, \bar{P}_0 is the total pressure generation given as,

$$\bar{P}_0 = \frac{L^2}{2c} (H_v \dot{\sigma}_z) . \quad (4.3)$$

$\psi = (2m+1)\pi/(2L)$, L is the total column length, and z is the location in the column downward from the applied stress. H_v is the 1-D Skempton coefficient given by,

$$H_v = - \left. \frac{\delta \bar{P}}{\delta \sigma_{zz}} \right|_{\epsilon_{xx}=\epsilon_{yy}=\zeta=0} = \frac{\alpha}{B_{sv} S_v} \quad (4.4)$$

where, B_{sv} is the uniaxial drained bulk modulus, and S_v is the 1-D specific storage given by $S_v = K/(\mu c)$.

μ is the fluid mobility given as $\frac{1}{\mu} = \frac{1}{2} \left(\frac{1}{\mu_w} + \frac{1}{\mu_{nw}} \right)$

The complete derivation of the analytical solution (Eqn. 4.2) can be found in many of the textbooks on soil mechanics, for example, Verrujit (2013) [109].

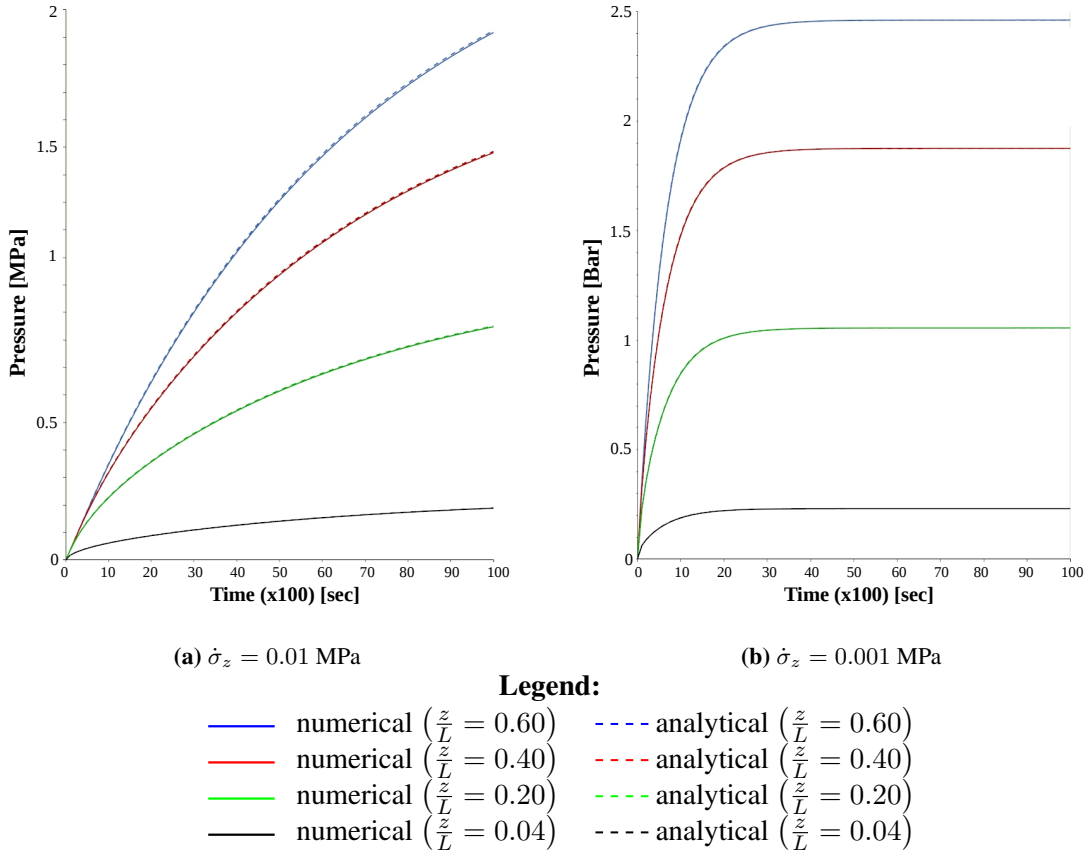


Figure 4.11: Test 3 - Terzaghi benchmark test results

Numerical simulation

For benchmarking, we use the test setting described by Kolditz et al. [48]. A soil column of 50 m is chosen. The properties of the rock material are listed in Table 4.6, and that of the two fluid phases are given in Table 4.7. The column is discretized uniformly into 200 grid cells. The initial fluid pressure in the column is null, and the initial fluid saturations are $S_w = 0.8$ and $S_{nw} = 0.2$. The hydraulic properties are chosen as $P_c = 0$ and $k_{r,w} = k_{r,nw} = 0.5$. As shown in Fig. 4.10, a load $\sigma_{zz} = 10$ MPa is applied at the top boundary at a loading rate of $\dot{\sigma}_z = 0.01$ and 0.001 MPa/s. The bottom boundary of the column is subjected to roller displacement BC and the top boundary is allowed to compress freely under the applied load $\dot{\sigma}_z$. The top boundary is a free-drainage boundary. All other boundaries are no-flow.

Results

The results of the numerical simulation for the two loading rates ($\dot{\sigma}_z = 0.01, 0.001$ MPa/s) are presented in Fig. 4.11a and Fig. 4.11b. Compression of the column leads to a rapid pressure

increase followed by dissipation of pressure over time from top of the column. It can also be observed that for a lower loading rate, the pore-pressure equilibrates faster, whereas, for a higher loading rate the pore-pressure takes longer to dissipate. The numerical results show a very good agreement with the analytical solution.

4.4 Test 4: Verification of kinetics-poroelasticity coupling

We now extend Terzaghi's 1D consolidation problem to include hydrate kinetics in the poroelastic coupling. We consider a confined soil sample which is uniformly hydrated and fully saturated with water. A constant vertical stress is applied at the top boundary while the lower boundary is held fixed. The upper boundary is fully drained, while at the lower boundary the initial pressure is maintained at all times. For time $t \leq 0^-$, the thermodynamic state of the sample lies on the hydrate stability curve, so that $P^{0-} = P_e^{0-}$, and the hydrate in the sample is stable (see Fig. 4.12). Here, P indicates the phase pressure, and P_e indicates the equilibrium pressure for hydrate stability. At time $t = 0$, the hydrate stability curve experiences an instantaneous shift such that $P_e^0 > P_e^{0-}$ (while $P^0 = P^{0-}$). The hydrate becomes unstable and begins to dissociate. This generates excess pore-pressure which prevents the *full consolidation* of the sample. The schematic for this problem is shown in Fig. 4.13. Although highly simplified, this problem helps us to isolate the *poroelastic-kinetic coupling*, thus providing a framework for validating the numerical implementation of our hydro-mechanical code for the hydrate reservoir model.

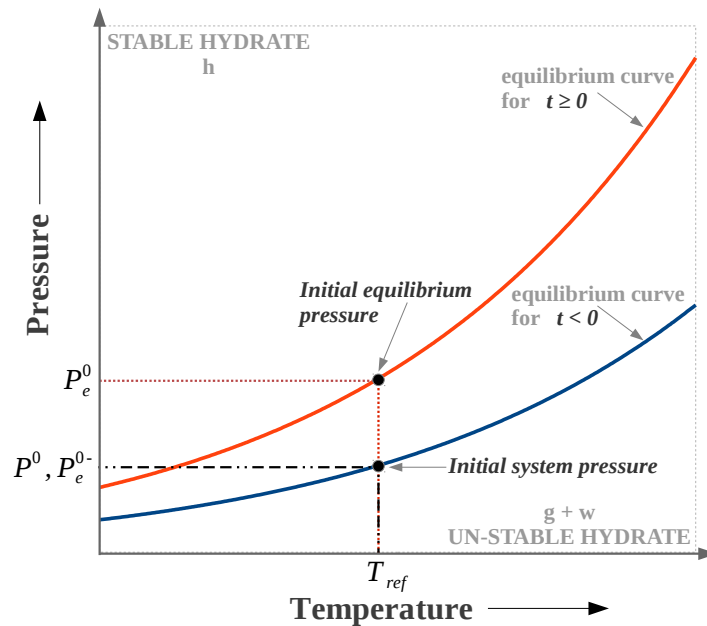


Figure 4.12: Test 4 - Hydrate stability curve shift at $t = 0$

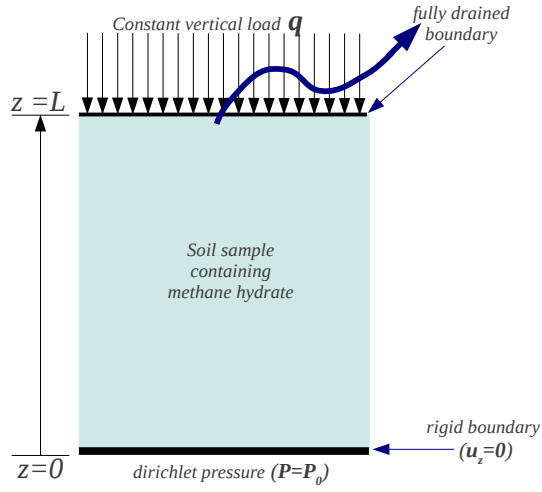


Figure 4.13: Test 4 - Problem schematic

Problem statement

For this problem we make the following additional assumptions:

- Gas does not dissolve in water phase, and water vapor is not formed, i.e., $\chi_g^{CH_4} = 1$, and $\chi_w^{H_2O} = 1$. Based on this assumption, we rewrite the mass balance equations for water and methane in Chapter 2 phase-wise instead of component-wise.
- All the processes, including hydrate phase change, are isothermal.
- There is no suction pressure between the two mobile phases, so that $P_g - P_w = 0$. Since the phase pressures are now equal, we drop the subscript and assign the symbol P to the phase pressures throughout this section.
- Relative permeabilities are $k_{r,g} = k_{r,w} = 0.5$.
- Effect of gravity is neglected.
- Effect of porosity and hydrate saturation on intrinsic permeability K is neglected, i.e. K is constant.

Further, we simplify the hydrate reaction kinetics model as,

$$\begin{aligned} \dot{q}_g &= k_0 A_s M_g (P_e - P) \\ A_s &= A_{s,0} S_h \end{aligned} \quad (4.5)$$

where k_0 is the rate of hydrate dissociation, and $A_{s,0}$ is the specific surface area of the hydrate free sample. Both k_0 and $A_{s,0}$ are assumed to be constant.

Using these assumptions, we can reduce the mathematical model described in Chapter 2 to an ODE for the pressure P , given by

$$\alpha \frac{d}{dt} \epsilon_v + S \frac{d}{dt} P = \nabla \cdot \frac{K}{\mu_f} \nabla P + C S_h (P_e - P) . \quad (4.6)$$

A detailed derivation is given in Appendix A.

The term S , called the *Storativity*, is given as,

$$S = \phi_e \left(\frac{S_{w,e}}{B_w} + \frac{S_{g,e}}{B_g} \right) + \frac{(\alpha - \phi_e)}{B_{sh}} ,$$

the term C lumps the volumetric source terms, as,

$$C = \left(N_h \frac{M_w}{\rho_w} + \frac{M_g}{\rho_g} - \frac{M_h}{\rho_{sh}} \right) k_0 A_{s,0} ,$$

ϵ_v is the volumetric strain given as $\epsilon_v = \nabla \cdot \mathbf{u}$, α is Biot's constant, and, μ_f is the fluid mobility given as,

$$\frac{1}{\mu_f} = \frac{1}{2} \left(\frac{1}{\mu_g} + \frac{1}{\mu_w} \right) .$$

Eqn. (4.6) is the *storage equation*. In this form it can be interpreted as: on the REV scale, the compression of the soil consists of compression of the pore-fluids and the compression of the solid particles, plus the total volume of fluid expelled from the REV and the fluid generated in the REV.

Further, in Eqn. (4.6), the term $\left[\alpha \frac{d}{dt} \epsilon_v \right]$ is the *mechanical* part, and the term $\left[\nabla \cdot \frac{\kappa}{\mu_f} \nabla P \right]$ is the *flow* part. The terms $\left[S \frac{d}{dt} P \right]$ and $[C S_h (P_e - P)]$ are the *coupling* terms, the former for the coupling between the flow and the mechanical models, and the latter for the coupling between the flow and the reaction kinetics models.

For the 1D problem under consideration, we can rewrite Eqn. (4.6) as

$$\alpha \frac{d}{dt} \epsilon_v + S \frac{d}{dt} P = \frac{K}{\mu_f} \frac{d^2}{dz^2} P + C S_h (P_e - P) . \quad (4.7)$$

In case of 1D deformation, the volumetric strain equals the vertical strain and is induced by the vertical stress σ'_{zz} ,

$$\frac{d}{dt} \epsilon_v = -C_m \frac{d}{dt} \sigma'_{zz} = -C_m \left(\frac{d}{dt} \sigma_{zz} - \alpha \frac{d}{dt} P \right) , \quad (4.8)$$

where, C_m is the compressibility of bulk porous material, such that $C_m = \frac{1}{B_m}$.

Thus, we eliminate $\frac{d}{dt}\epsilon_v$ in Eqn. (4.7) using Eqn. (4.8), which gives

$$\frac{d}{dt}P = \frac{\alpha C_m}{\alpha^2 C_m + S} \frac{d}{dt}\sigma_{zz} + \frac{\kappa}{\mu_f (\alpha^2 C_m + S)} \frac{d^2}{dz^2}P + \frac{C S_h}{\alpha^2 C_m + S} (P_e - P) . \quad (4.9)$$

At time $t = 0$, an external load q is instantaneously applied, and the equilibrium pressure of hydrates is instantaneously changed from P_e^{0-} to P_e^0 . Since both these processes are instantaneous, no fluid is mobilized at $t = 0$, i.e., in Eqn. (4.9), $\frac{d^2}{dz^2}P = 0$. So, from Eqn. (4.9), we get the initial condition of the sample as

$$t = 0 : P = P^0 = \frac{\alpha C_m}{\alpha^2 C_m + S + C S_h} q + \frac{C S_h}{\alpha^2 C_m + S + C S_h} P_e^0 . \quad (4.10)$$

For $t > 0$, the external load remains constant, so $\frac{d}{dt}\sigma_{zz} = 0$. The equilibrium pressure also remains constant, i.e., $P_e^{0+} = P_e^0 = P_e$. Thus, from Eqn. (4.9),

$$\begin{aligned} t > 0 : \frac{d}{dt}P &= \underbrace{\frac{\kappa}{\mu_f (\alpha^2 C_m + S)}}_{C_v} \frac{d^2}{dz^2}P + \underbrace{\frac{C S_h}{\alpha^2 C_m + S}}_{C_r} (P_e - P) \\ \implies t > 0 : \frac{d}{dt}P &= C_v \frac{d^2}{dz^2}P + C_r (P_e - P) . \end{aligned} \quad (4.11)$$

C_v is the *consolidation parameter* which comes from the Terzaghi's classical theory of consolidation. C_r is the *reaction parameter*. It is indicative of the damping of the normal consolidation due to dissociation kinetics.

The boundary conditions at the top and bottom of the sample are

$$\begin{aligned} t > 0, z = L : \frac{d}{dz}P &= 0 \\ t > 0, z = 0 : P &= P^0 . \end{aligned} \quad (4.12)$$

The ODE in Eqn. (4.11) is a non-homogeneous ODE. We can homogenize it by choosing a new primary variable \bar{P} such that $\bar{P} = P_e - P$. Then the initial-boundary-value problem (IBVP)

can be formally summarized as

$$\begin{aligned}
 0 \leq z \leq L, t > 0 & : \frac{d}{dt} \bar{P} = C_v \frac{d^2}{dz^2} \bar{P} - C_r \bar{P} \\
 z = 0, t > 0 & : \bar{P} = P_e - P^0 \\
 z = L, t > 0 & : \frac{d}{dz} \bar{P} = 0 \\
 0 \leq z \leq L, t = 0 & : \bar{P} = P_e - P^0
 \end{aligned} \tag{4.13}$$

$$\text{where, } P^0 = \frac{\alpha C_m^0}{\alpha^2 C_m^0 + S^0 + C S_h^0} q + \frac{C S_h^0}{\alpha^2 C_m^0 + S^0 + C S_h^0} P_e$$

which is a homogeneous ODE with non-homogeneous boundary conditions. An analytical solution can be obtained for this problem using any of the standard techniques for solving ODEs. The final solution for P can be written as,

$$\begin{aligned}
 \frac{P_e - P(z, t)}{P_e - P^0} &= \frac{\cosh(\theta(L - z))}{\cosh(\theta L)} \\
 &+ \frac{2}{L} \sum_{n=1}^{\infty} \left(\frac{1}{\lambda_n} \left[1 - \frac{\lambda_n^2}{\lambda_n^2 + \theta^2} \right] \sin(\lambda_n z) \exp[-C_v (\lambda_n^2 + \theta^2) t] \right). \tag{4.14}
 \end{aligned}$$

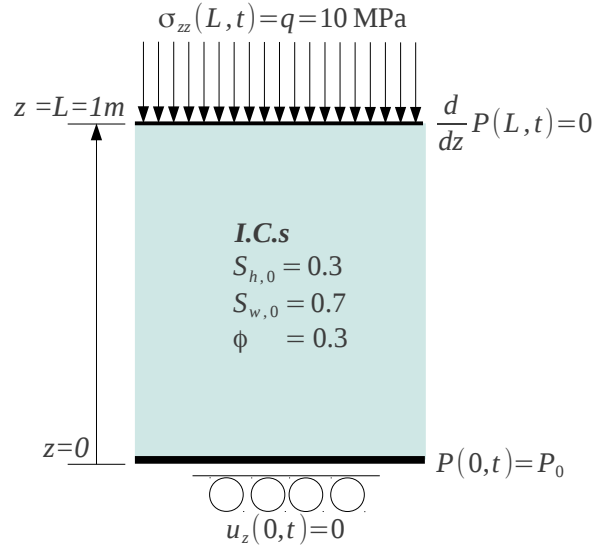
The details of the solution for the IBVP are included in Appendix B.

Computational domain and test setting

We chose a sample of length $L = 1$ m containing 30% hydrate by volume. The sample is initially fully water saturated and is contained in a pressure vessel at $P^0 = 6$ MPa. A constant external load $q = 10$ MPa is applied at the top boundary, i.e., at $z = L = 1$. At the bottom boundary, i.e., $z = 0$, the pressure is held constant at the initial value.

Fig. 4.14 shows the domain specifications, the initial conditions, and the boundary conditions. The material properties are listed in Table 4.8.

The storage equation governing this problem, Eqn. (4.13), contains two parameters: C_v and C_r . To test the numerical implementation, we chose three different values of C_v and C_r , each with a different order of magnitude. Therefore, we run nine tests with all combinations of the chosen C_v and C_r . We control the parameter C_v by varying the sample permeability κ and the parameter C_r by varying the dissociation rate constant k_0 . For each test, the value of P_e is chosen such that the initial condition of no-drainage is satisfied. The control parameters for each of the nine tests are listed in Table 4.9. It can be observed in Table 4.9 that as the reaction rate constant k_0 increases the value of equilibrium pressure P_e decreases. This is due to the

**Figure 4.14:** Test 4 - Computational domain settings**Table 4.8:** Test 4 - Material properties

Property	Symbol	Unit	Value	Property	Symbol	Unit	Value
Water phase				Hydrate phase			
Density	ρ_w	$kg \cdot m^{-3}$	997.05	Density	ρ_h	$kg \cdot m^{-3}$	900
Molar mass	M_w	$kg \cdot mol^{-1}$	0.018	Molar mass	M_h	$kg \cdot mol^{-1}$	0.119
Dynamic viscosity	μ_w	$Pa \cdot s$	8.9008×10^{-3}	Hydration number	N_h	—	5.75
Bulk modulus	B_w	GPa	2.933	Young's modulus	E_h	GPa	1.35
Gas phase				Soil phase			
Density	ρ_g	$kg \cdot m^{-3}$	0.717	Density	ρ_s	$kg \cdot m^{-3}$	700
Molar mass	M_g	$kg \cdot mol^{-1}$	0.016	Surface area	$A_{s,0}$	m^2	10^5
Dynamic viscosity	μ_g	$Pa \cdot s$	1.0245×10^{-5}	Young's modulus	E_s	GPa	0.3
Bulk modulus	B_g	GPa	0.1013	Solid composite			
				Poisson ratio	ν_{sh}	—	0.2
				Biot constant	α	—	0.8

Table 4.9: Test 4 - Control parameters

test ID	κ [mD]	$k_0 \times a^*$ [$\frac{mol}{m^2 Pa s}$]	C_v	C_r	P_e [MPa]
1	0.1	360	1.53755	0.289504	19.151
2	0.01	360	0.153755	0.289504	19.151
3	0.001	360	0.0153755	0.289504	19.151
4	0.1	3600	1.53755	2.89504	7.315
5	0.01	3600	0.153755	2.89504	7.315
6	0.001	3600	0.0153755	2.89504	7.315
7	0.1	36000	1.53755	28.9504	6.132
8	0.01	36000	0.153755	28.9504	6.132
9	0.001	36000	0.0153755	28.9504	6.132

$$*a = \exp(-\Delta E_a/(RT)), \text{ where, } \Delta E_a/R = 9400 \text{ K and } T = 283.15 \text{ K}$$

no-drainage condition at $t = 0$. The faster the dissociation, the more the generated fluids will mobilize. Conversely, the slower the dissociation reaction, the higher margin we get for raising P_e without instantaneously mobilizing the fluids.

Simulation and results

The domain is discretized into 400 cells in z-direction, and the problem is solved in 1D. The time-step is kept constant at $t = 0.1$ s and the simulation is run until $t_{end} = 60$ s.

In Fig. 4.15, the numerically computed pressure values for each test case 1 – 9 are compared with the analytical pressure $P(z, t)$ obtained from Eqn. (B.11). For each test case, the pressure solutions are plotted over time at the observation points $z = 1$ m, 0.8 m, 0.6 m, 0.4 m and 0.2 m. The plots show a good agreement between the numerical and the analytical solutions signifying that the poroelastic - reaction kinetics coupling terms are correctly handled in the numerical code.

testID-3 The pressure build-up along the length of the sample is plotted for *testID 3* in Fig. 4.17. Also, for *testID 3* a grid-convergence study is performed. The mesh is refined from $n = 25$ cells up to $n = 800$ cells, and correspondingly, the time-step size is reduced from $\delta t = 2$ s down to $\delta t = 0.0625$ s such that the ratio $\frac{\delta z}{\delta t}$ remains constant. The L2 error is calculated at $t = 10$ s for each refinement and is plotted against the number of grid-cells n on a log-log graph in Fig. 4.16. It can be seen that the error decays linearly with refinement. This is in line with the finite volume discretization technique.

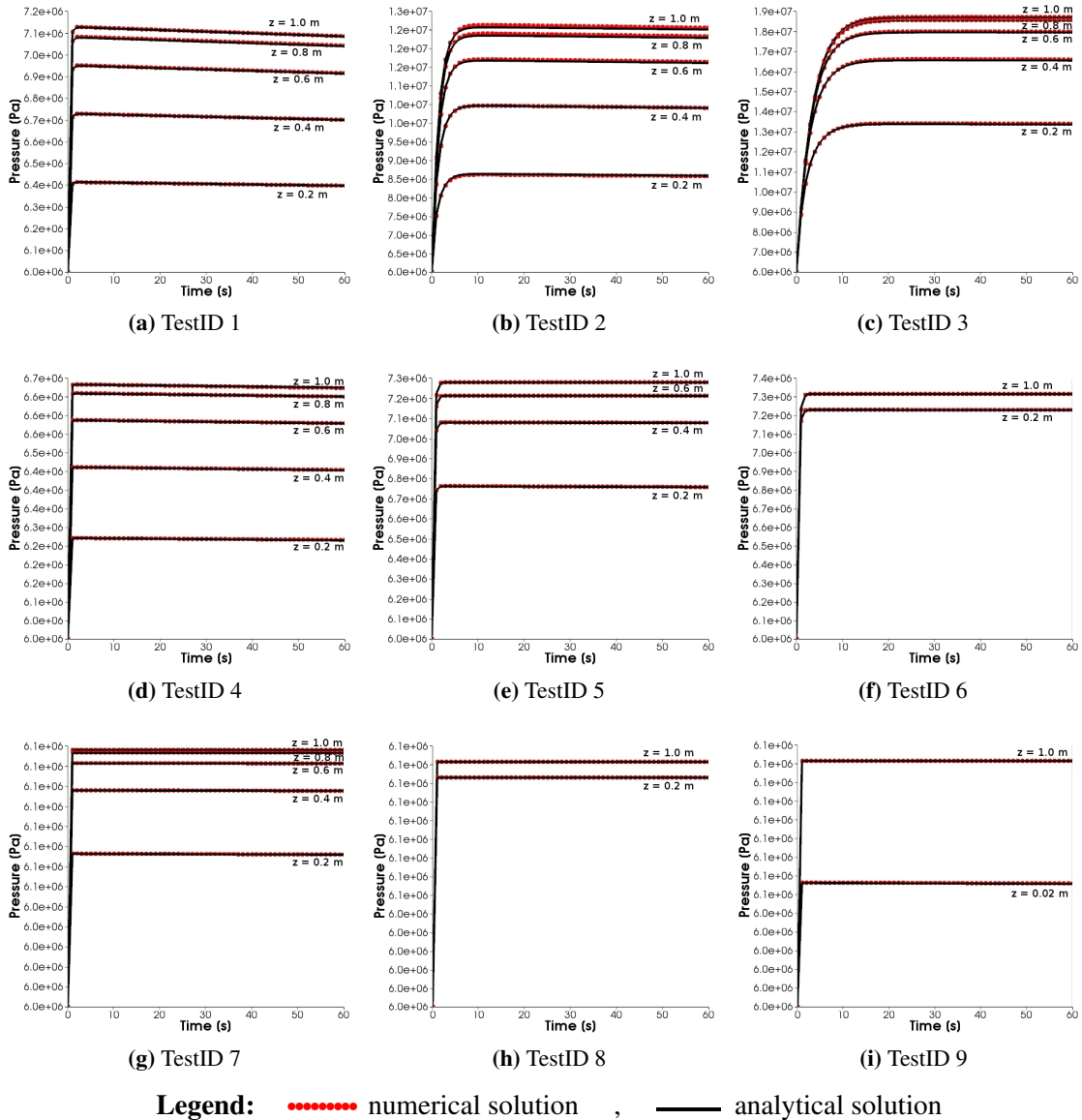


Figure 4.15: Test 4 - Comparison of numerical and analytical solutions

Note: For *TestID 5*, pressure profiles at $z = 1$ m and 0.8 m are equal, for *TestID 6* and *TestID 8*, pressure profile at $z = 1$ m, 0.8 m, 0.6 m, and 0.4 m are equal, and for *TestID 9* pressure profile at $z = 1$ m, 0.8 m, 0.6 m, 0.4 m, and 0.2 m are equal.

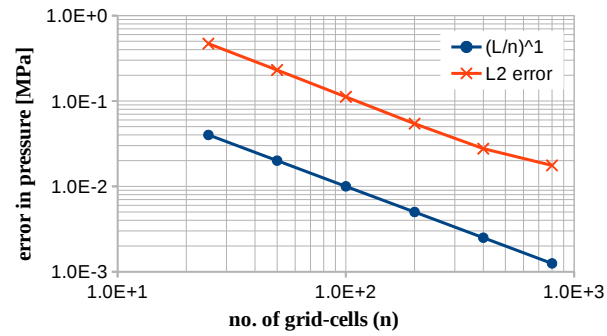


Figure 4.16: Test 4 - testID 3: L2-error vs n

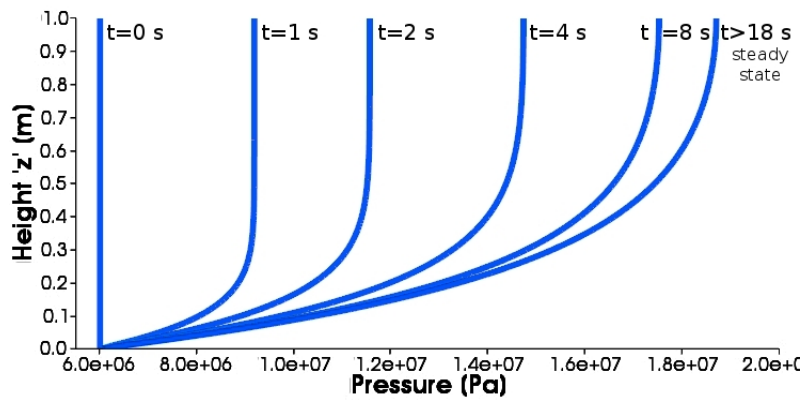


Figure 4.17: Test 4 - testID 3: Time-evolution of the numerical solution of P along the height of the sample

Performance evaluation of the MRT methods

In this chapter, we test the performance of the two MRT algorithms presented in Section 3.3. We consider a 1D consolidation in a depressurized methane hydrate sample as our test problem. The test setting is described in Section 5.1. This problem is numerically simulated using the semi-implicit and the compound-fast MRT methods. For comparison, the problem is also simulated using the iterative block Gauss-Seidel scheme. The performance of the MRT methods is evaluated in terms of accuracy and speedup as compared to the iterative solution scheme, which are defined in Section 5.2. The errors and the speedup obtained for both the MRT methods are presented in Section 5.3, and some conclusions are drawn in Section 7.3 on the advantages and disadvantages of each of the MRT method in terms of their applicability to our hydrate reservoir model. In particular, we discuss the factors which affect the choice of a particular MRT method for a given problem.

5.1 Test problem

The problem set-up consists of a confined soil sample of height 1m. The sample has a uniformly distributed hydrate saturation of $S_h = 0.4$ and is fully saturated with water. The porosity and the permeability of the hydrate free soil are $\phi = 0.3$ and $\kappa = 10^{-12} \text{ m}^2$ respectively. A constant vertical stress of 1 MPa is applied at the top boundary while the lower boundary is held fixed. At the upper boundary the pressure is kept constant at the initial value of 10 MPa, while at the lower boundary a low pressure of 6 MPa is maintained at all times.

The schematic for this problem is shown in Fig. 5.1. The selected material properties and model parameters are listed in Table 5.1.

Table 5.1: Material properties and model parameters

Thermal conductivities		
k_g^c	$-0.886 \times 10^{-2} + 0.242 \times 10^{-3} T - 0.699 \times 10^{-6} T^2 + 0.122 \times 10^{-8} T^3$	$\frac{W}{m \cdot K}$
k_w^c	$0.3834 \ln(T) - 1.581$	$\frac{W}{m \cdot K}$
k_h^c	2.1	$\frac{W}{m \cdot K}$
k_s^c	1.9	$\frac{W}{m \cdot K}$
Specific heat capacities		
Cp_w	4186	$\frac{J}{kg \cdot K}$
Cv_w	$Cp_w + R_{H_2O}$	$\frac{J}{kg \cdot K}$
Cv_h	2700	$\frac{J}{kg \cdot K}$
Cv_s	800	$\frac{J}{kg \cdot K}$
Dynamic viscosities		
μ_g	$10.4 e^{-6} \left(\frac{273.15 + 162}{T + 162} \right) \left(\frac{T}{273.15} \right)^{1.5}$	$Pa \cdot s$
μ_w	$0.001792 \exp \left[-1.94 - 4.80 \left(\frac{273.15}{T} \right) + 6.74 \left(\frac{273.15}{T} \right)^2 \right]$	$Pa \cdot s$
Densities		
ρ_g	$\frac{P_g}{zR_gT}$	$\frac{kg}{m^3}$
ρ_w	1000	$\frac{kg}{m^3}$
ρ_h	900	$\frac{kg}{m^3}$
ρ_s	2100	$\frac{kg}{m^3}$
Hydraulic properties		
Brooks-Corey parameters		
λ_{BC}	1.2	
P_{entry}	50	kPa
Hydrate kinetics		
k^r	$3.6 \times 10^4 \exp \left(-\frac{9752.73}{T} \right)$	$\frac{mol}{m^2 \cdot Pa \cdot s}$
N_h	5.75	
P_{eqb}	$A_1 = 1000, A_2 = 14.17, A_3 = 1886.79$	Pa
\dot{Q}_h	$B_1 = 56599, B_2 = 16.744$	$\frac{W}{m^3}$
Poroelectricity parameters		
α_{biot}	0.8	
ν_{sh}	0.15	
E_{sh}	$160 + 250 S_h$	MPa

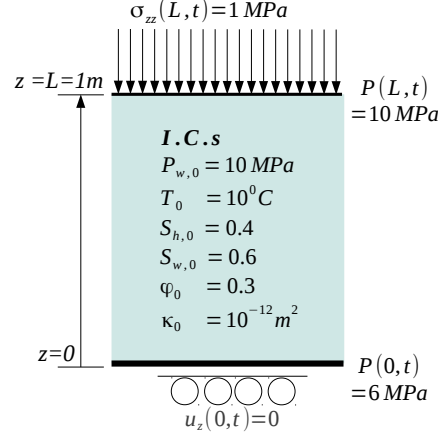


Figure 5.1: Schematic of the 1D test problem

5.2 Numerical simulation

We discretize the space domain into 200 cells along the Z-axis, and run the simulation up to $T = 18000$ sec. For simplicity, we assume uniform, non-adaptive micro and macro time-grids. The time step size for the micro grid is fixed at $h_{n,k} = h = 60$ sec for all n and k . This time-step satisfies the CFL condition for the flow model to ensure stability of the active system. We chose different values of the multirate factor, as,

$$m = [1, 2, 5, 10, 20, 30],$$

so that the macro grid is m times coarser than the micro grid, i.e. $H_n = H = mh$ for all n .

We evaluate the performance of the two MRT methods in terms of 1) Speed up, and 2) Relative error. Speed up is calculated as,

$$\text{speed-up} = \frac{\text{CPU-time for } m\text{-step MRT method}}{\text{CPU-time for iteratively coupled scheme}} \quad (5.1)$$

The time step size of $h = 60$ sec is used for the iteratively coupled scheme. The relative error is calculated as,

$$\text{relative error} = \frac{\text{L2-error by } m\text{-step MRT method}}{\text{L2-error by iteratively coupled scheme}} \quad (5.2)$$

where, to compute the error in the solution from the iteratively coupled scheme and the MRT schemes, the solution from a fully coupled fully implicit scheme is used as the reference solution. The time step size used for the fully coupled fully implicit scheme is also $h = 60$ sec.

For the solution of the active system on the micro grid, a minimum error reduction of 10^{-8} is prescribed for the Newton solver. For the predictor step of the Compound-fast MRT method, the minimum error reduction for the Newton solver is relaxed to 10^{-3} .

5.3 Results

5.3.1 Semi-implicit MRT method

Relative error

In Fig. 5.2, the relative error in P_g is plotted over m for the semi-implicit MRT method using polynomials of order $p = 0, 1, 2, 3$ in the extrapolation steps. The scheme with polynomial of order $p = 0$ is the most stable, but gives only $\approx 80\%$ accuracy as compared to the iteratively coupled solution scheme, while the polynomial of order $p = 2$ gives an accuracy of $\approx 99\%$ compared to the iteratively coupled scheme for $m \leq 5$, but becomes increasingly unstable for higher m . The polynomial of order $p = 3$ does not give any significant advantage in terms of accuracy but makes the scheme highly unstable.

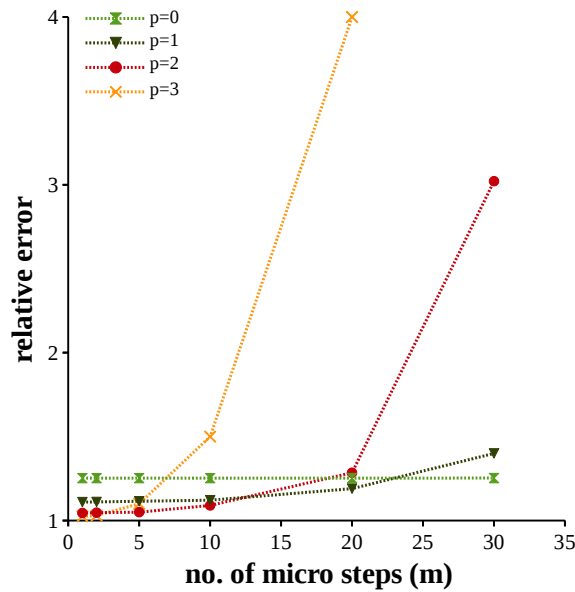


Figure 5.2: Relative error in P_g over m at $t = 18000$ sec for the semi-implicit fast-first MRT method using polynomials of order $p = 0, 1, 2, 3$ to approximate \mathbf{X}_G in the extrapolation steps.

Speed up

Consider integration by the iteratively coupled and the semi-implicit MRT schemes between the synchronization level $n - 1$ to n . There are m uniform micro steps of size h and one macro step of size $H = mh$ between $n - 1$ and n . The iteratively coupled scheme solves both the flow and the geomechanical systems on the micro grid, while the semi-implicit MRT solves the flow system on the micro grid and the geomechanical system on the macro grid.

Let W_g be the time required to solve the geomechanical system, and w_f be the time required for executing one Newton step in the flow system. If the iterative scheme requires n_{it} Newton

steps to converge, then time required to solve the flow system per step is $W_f = n_{it}w_f$. Further, if n_{fp} fixed-point iteration steps are required to get the solution, then the total time required for integration from $n - 1$ to n using the iteratively coupled scheme is,

$$(\text{CPU-time})_{it} = m n_{fp} (W_f + W_g) .$$

Similarly, if the semi-implicit MRT scheme takes n_{mrt1} Newton steps to converge, then time required to solve the flow system per micro step is,

$$W_{f,mrt1} = n_{mrt1}w_f = n_{s1}W_f ,$$

where, $n_{s1} = \frac{n_{mrt1}}{n_{it}}$.

The total time required for integration from $n - 1$ to n using the semi-implicit MRT scheme is, thus,

$$(\text{CPU-time})_{mrt1} = m n_{s1} W_f + W_g$$

Therefore, the speed up is given as,

$$\begin{aligned} \text{speed-up} &= \frac{(\text{CPU-time})_{it}}{(\text{CPU-time})_{mrt1}} = \frac{m n_{fp} (W_f + W_g)}{m n_{s1} W_f + W_g} \\ &= \frac{n_{fp} m}{n_{s1} (1 - C) m + C} \end{aligned} \quad (5.3)$$

where, $C = \frac{W_g}{W_f + W_g}$.

In Eqn. (5.3), $0 < C < 1$, $n_{fp} \geq 1$, and $n_{s1} = 1$ for a stable system and $n_{s1} > 1$ for an unstable system.

We can identify the following two special cases:

1. For a stable system, for the case of $m = 1$ (i.e. decoupled sequential scheme) we get the minimum value of speed-up,

$$(\text{speed-up})_{min} = n_{fp} . \quad (5.4)$$

2. For infinitely large m (i.e. the limiting case of $m \rightarrow \infty$) we get the maximum value of speed-up,

$$(\text{speed-up})_{max} = \frac{n_{fp}}{n_{s1} (1 - C)} . \quad (5.5)$$

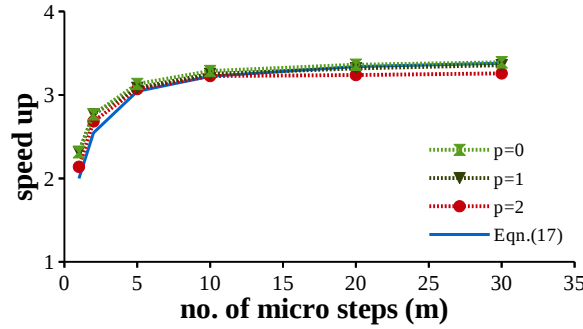


Figure 5.3: Speed up in P_g over m for the semi-implicit fast-first MRT method using polynomials of order $p = 0, 1, 2$ to approximate \mathbf{X}_C in the extrapolation steps.

The speed-up curves for the extrapolation based semi-implicit MRT schemes using polynomials of order $p = 0, 1, 2$ are plotted in Fig. 5.3. For comparison, the speed-up curve from Eqn. (5.3) is also plotted in Fig. 5.3 using $W_g = 0.9$ sec, $W_f = 1.21$ sec, $n_{fp} = 2$ and $n_{s1} = 1$. We can see that our numerical results for the speed-up reflect very well the behaviour expected from Eqn. (5.3). The speed up curves for polynomial order $p = 0, 1, 2$ coincide for those values of m where the respective schemes are stable. The maximum speed-up for polynomial order $p = 2$ is slightly lower due to instabilities at higher m , as predicted.

It can be further inferred that the higher the value of C , the higher is the speed-up. This implies that for problems where the solution of the latent system is more time-consuming, for example in the non-linear case or the $3D$ case, a higher speed-up can be expected from the extrapolation based semi-implicit MRT schemes.

Stability of the scheme with extrapolation polynomial of order $p = 2$

For problems where a high accuracy is desired, we usually use an extrapolation polynomial of order $p = 2$, but this results in instabilities. In Fig. 5.4a and Fig. 5.4b showing the P_g and the u_z profiles, we can see that the solutions deviate from the reference solution very much for $m > 10$ for this example. This implies that we cannot choose any arbitrary value of m . The value of m should be small enough so that the extrapolation error does not dominate, but it should be large enough so that we can take advantage of the speed up optimally, thus making the choice of m an important consideration.

Choice of m : Consider the non-dimensional numbers C_v and C_r . C_v is the consolidation coefficient which comes from Terzaghi's consolidation theory, and is given by,

$$C_v = \frac{\kappa \left(\frac{k_{r,w}}{\mu_w} + \frac{k_{r,g}}{\mu_g} \right)}{\alpha_{biot}^2 K_m + S}.$$

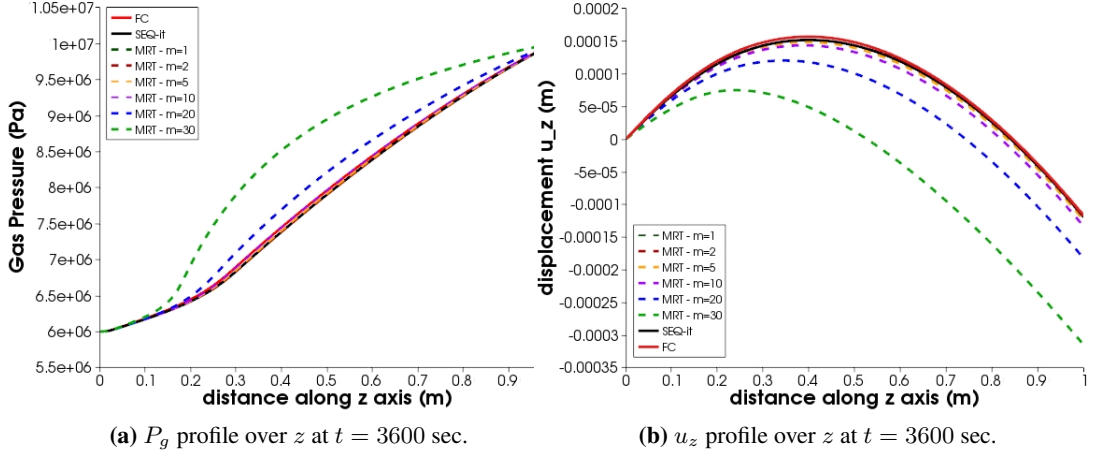


Figure 5.4: P_g and u_z profiles for fully-coupled (FC) scheme, iteratively-coupled (SEQ-it) scheme, and m -step semi-implicit MRT schemes using polynomial of order $p = 2$ for extrapolation.

C_r is the reaction coefficient indicative of the damping of the normal consolidation due to dissociation kinetics, and is given by,

$$C_r = \frac{\left(\frac{M_g}{\rho_g} + N_h \frac{M_w}{\rho_w} - \frac{M_h}{\rho_h} \right) k^r A_{r,s}}{\alpha_{biot}^2 K_m + S},$$

where, $\phi_e = \phi(1 - S_h)$ is the effective porosity, S is the bulk storativity of the system given by, $S = \phi_e(K_w S_{w,e} + K_g S_{g,e}) + (\alpha - \phi_e) K_{sh}$, K_γ is the compressibility of material γ , and $K_m = \frac{K_{sh}}{1 - \alpha_{biot}}$ is the compressibility of the bulk porous material.

The derivation of C_r can be found in Test problem 4 in Section 4.4 for a simplified 1D consolidation problem with hydrate dissociating in the sample due to depressurization.

The rate of consolidation is directly proportional to C_v and inversely proportional to C_r . Thus, the C_v/C_r ratio can be seen as the relative activity of the latent component.

In Fig. 5.5, we show the errors in P_g plotted over m for a broad range of C_v/C_r ratio. We observe that the higher the relative activity of the latent component, the more dominating is the extrapolation error. For the case of a non-dominating extrapolation error, the values of m can be chosen very large. However, in the absence of a priori estimate of the relative activity, the value of m must be kept small in order to keep the relative error close to 1. In our hydrate reservoir simulator we choose $m \leq 5$.

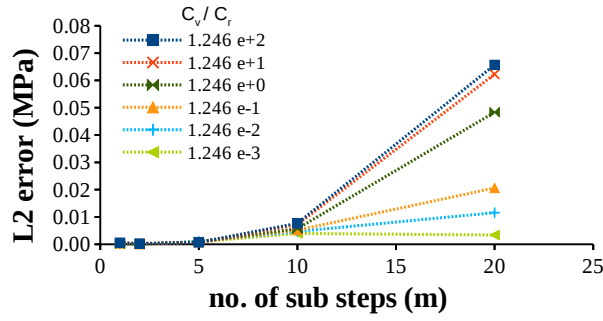


Figure 5.5: Error in P_g plotted over m for different values of the C_v/C_r ratios for m -step semi-implicit MRT schemes using polynomial of order $p = 2$ for extrapolation.

5.3.2 Compound-fast MRT method

Relative error

In Fig. 5.6a and Fig. 5.6b, we show the relative errors in P_g and u_z plotted over m , respectively, for the compound fast MRT method. For comparison, we have also plotted the errors in P_g and u_z for the semi-implicit MRT method using extrapolation polynomials of order $p = 2$. We can see that the relative errors for this scheme remain close to 1 and do not depend on m significantly.

In this example, the active ODE becomes unsolvable in the predictor step at $m \geq 60$ for the minimum error reduction of 10^{-3} that is prescribed for the Newton solver.

Speed-up

Fig. 5.6c shows the speed up obtained from this scheme as compared to the speed up from the semi-implicit scheme. We can see that this scheme gives lower speed up, especially at smaller values of m .

The speed-up curve can be derived for the compound-fast method using similar arguments as in the case of the semi-implicit MRT method. The compound-fast method solves the flow system once on the macro-grid (during the predictor step) and once on the micro grid (m micro-steps), and the geomechanical system twice on the macro grid (once during the predictor step, and once during the corrector-macro step). If the compound-fast scheme takes $n_{mrt2,p}$ and n_{mrt2} Newton steps to converge for the predictor-step and for each micro-step, respectively, then the time required to integrate the flow system per micro step is,

$$W_{f,mrt2} = n_{mrt2} w_f = n_{s2} W_f ,$$

and the time required to solve the flow system for the predictor step is,

$$W_{f,p} = n_{mrt2,p} w_f = n_{s2,p} W_f ,$$

where, $n_{s2,p} = \frac{n_{mrt2,p}}{n_{it}}$, and $n_{s2} = \frac{n_{mrt2}}{n_{it}}$. Furthermore, since the scheme is stable, $n_{s2} = 1$.

The total time required for integration from $n - 1$ to n using the compound-fast MRT scheme is, thus,

$$(\text{CPU-time})_{mrt2} = W_{g,p} + (n_{s2,p} + m) W_f + W_g$$

where, $W_{g,p}$ is the time required to solve the geomechanical system in the predictor step.

Therefore, the speed-up is given as,

$$\begin{aligned} \text{speed-up} &= \frac{(\text{CPU-time})_{it}}{(\text{CPU-time})_{mrt2}} \\ &= \frac{m n_{fp} (W_f + W_g)}{W_{g,p} + (n_{s2,p} + m) W_f + W_g} \\ &= \frac{n_{fp} m}{(1 - C) m + C + \Delta_p} \end{aligned} \quad (5.6)$$

where, $\Delta_p = n_{s2,p} (1 - C) + C_p$, s.t., $C_p = \frac{W_{g,p}}{W_f + W_g}$.

In Eqn. (5.6), $\Delta_p > 0$ because $n_{s2,p} > 0$, $C_p > 0$ and $0 < C < 1$.

Comparing equations (5.3) and (5.6), we can conclude that for any given $m \geq 1$, the speed-up obtained from the compound-fast MRT method is always smaller than that obtained from corresponding semi-implicit MRT method. However, for the limiting case of $m \rightarrow \infty$, the speed-up from compound-fast method approaches the speed-up from a stable semi-implicit method.

5.4 Discussion

5.4.1 Semi-implicit MRT method

Advantages

- This scheme gives a higher speed up for a given m , especially if the natural time scale of the latent component is comparable to that of the active component.
- This scheme is more attractive when the solution of the latent system is more time-consuming, for example in case of a 3D problem where the matrix assembly times are larger, or when the latent AE system is non-linear.

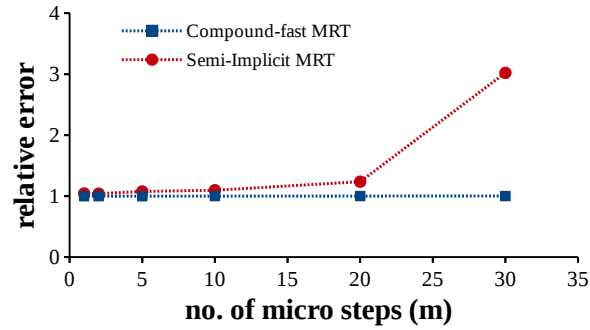
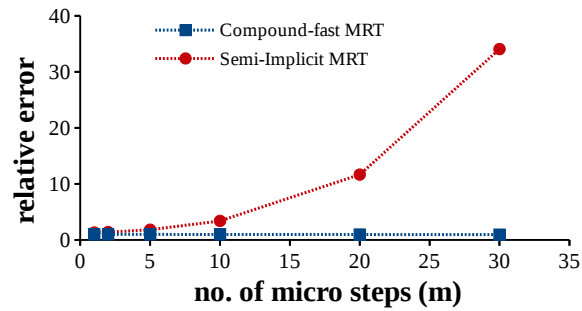
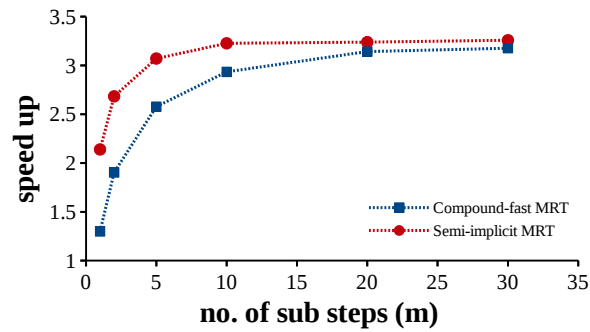
(a) Relative error in P_g over m (b) Relative error in u_z over m (c) Speed-up over m

Figure 5.6: Relative error and speed-up curves for the compound-fast MRT method and the semi-implicit MRT method using polynomial of order $p = 2$ for extrapolation.

Disadvantages

- The scheme with lower order polynomials for extrapolation shows high stability but low accuracy. The use of higher order polynomial extrapolation improves the accuracy significantly, but introduces errors which grow exponentially with m , thus, making the scheme unstable at large m values.
- With the use of higher order polynomials, the choice of m becomes strongly dependent on the actual activity of the latent components.
- For problems where relative activities of the components are expected to fluctuate over time, one must use an MRT scheme which is relatively insensitive to the component activities. Therefore, for such problems the semi-implicit scheme can only be used with lower order polynomial extrapolation, thus compromising the accuracy of the solution.

5.4.2 Compound-fast MRT method**Advantages**

- This scheme is stable for arbitrarily large values of m , provided that the active system is stable and solvable upto the prescribed error reduction in the predictor-step [107].
- The errors in solution are comparable to that of the iteratively coupled solution scheme and do not grow with increasing m . The time-mesh for the latent component can be made quite coarse irrespective of the actual activity of the latent component.
- It is easier to handle problems where the activity of latent system fluctuates in time because the stability of the scheme is insensitive to the refinement of the macro-grid.

Disadvantages

- It gives lower speed-up as compared to the semi-implicit scheme, especially for lower values of m . If the natural time scale of the latent system is large, then this increase in computation time due to predictor steps can be compensated by using a very coarse macro grid. If, however, the natural time scale of the latent system is small and/or the time-evolution of the latent component is desired at a finer resolution, then this method may prove computationally more intensive.

To conclude, for multi time-scale hydro-geomechanical subsurface flow problems the multi-rate time stepping methods provide a significant speed up as compared to fully coupled or decoupled (iterative or sequential) schemes, provided the model can be partitioned into sufficiently weakly coupled subsystems having distinctly different time-scales. In our case, we deal with subsurface hydrate reservoirs where the mathematical model is naturally partitioned into active flow system and latent geomechanical system. In this chapter, we have shown that the stability of the extrapolation based semi-implicit method is sensitive to the relative activity of the latent component, while the compound-fast method is fairly independent of the relative activity of the

latent component. If the difference in time-scale between the active and latent components is comparable, then the semi-implicit MRT is very attractive as it gives a higher speed up. It must, however, be kept in mind that this method is only conditionally stable for higher order extrapolation and extrapolation errors tend to pile up with increasing m . It is therefore necessary to keep the choice of m small. On the other hand, if the difference in time-scale between the active and latent components is large, then the compound fast MRT method is more suitable as it is stable for arbitrarily large values of m , provided that the active system is solvable in the predictor step. Another important consideration is whether the relative activities are expected to vary over time. For problems where the activity of the latent component in particular fluctuates in time, it is important that the MRT method be insensitive to the relative activity of the latent component, thus making compound-fast MRT methods very attractive in such cases.

Numerical study of a 3D hydrate reservoir problem

In Chapter 4, we considered examples which focussed on systematically isolated couplings and model components. In this chapter, we present a more complex example where we simulate the hydro-geomechanical processes in a subsurface hydrate reservoir which is destabilized by depressurization using a low pressure gas well. This example puts together all the important components of our model including dissociation kinetics, non-isothermal effects, multi-phase multi-component fluid flow, and geo-mechanics, and qualitatively shows the effects and counter effects of various physical processes occurring in the hydrate reservoir. The objective of this example is to give an insight into the capabilities of our hydrate reservoir model. A detailed quantitative analysis of the problem and parameter sensitivity study is, however, beyond the scope of this thesis.

6.1 Test setting

We consider a scaled down 3D reservoir with dimensions $10m \times 10m \times 5m$, as shown in Fig. 6.1. The hydrate is homogeneously distributed in a $4m$ thick layer lying between $0.5m \leq z \leq 4.5m$, and has a saturation of 40% by volume. The reservoir is fully saturated with water and has an initial pressure of 10 MPa. The reservoir is depressurized through a low pressure gas well located at $(0, 0, z)$. The pressure in the gas well is maintained at $P_{well} = 4$ MPa. A constant vertical load of 10 MPa is acting on the top boundary of the reservoir (i.e. at $z = 10$ m).

The initial and the boundary conditions are listed in Table 6.1 and Table 6.2, respectively. The material properties and other model parameters are listed in Table 6.3.

Table 6.1: Initial conditions for depressurized 3D-reservoir example

Hydrate layer	
at $t = 0$, for	$P_{eff,i} = 10$ MPa
$0 \leq x, y \leq 10, 0.5 \leq z \leq 4.5$	$S_{h,i} = 0.4$
	$S_{g,i} = 0$
	$T_i = 10$ °C
	$K_i = 0.0198$ mD
	$\phi_{eff,i} = 0.18$
Hydrate-free layers	
at $t = 0$, for	$P_{eff,i} = 10$ MPa
$0 \leq x, y \leq 10, z < 0.5$	$S_{h,i} = 0$
and	$S_{g,i} = 0$
$0 \leq x, y \leq 10, z > 4.5$	$T_i = 10$ °C
	$K_i = 0.1$ mD
	$\phi_{eff,i} = 0.3$

Table 6.2: Boundary conditions for depressurized 3D-reservoir example

FLOW model	
Gas well at	$P_g = 4$ MPa
$x = 0, y = 0, 0 \leq z \leq 5$	$S_w = 0$
	$\nabla \cdot T = 0$
Pressure constraint at	$P_{eff} = P_{eff,i}$
$x = 10, y = 10, 0 \leq z \leq 5$	$S_w = S_{w,i}$
	$T = T_i$
No-flow and adiabatic conditions	$\mathbf{v}_g \cdot \hat{n} = 0$
on remaining boundaries, i.e.,	$\mathbf{v}_w \cdot \hat{n} = 0$
	$\nabla \cdot T = 0$
GEOMECHANICAL model	
Top boundary	
$0 \leq x \leq 10, 0 \leq y \leq 10, z = 5$	$\sigma_{zz} = 10$ MPa ,
	$\sigma_{xy} = \sigma_{yx} = 0$
Bottom boundary	
$0 \leq x \leq 10, 0 \leq y \leq 10, z = 0$	$u_z = 0,$
	$\sigma_{xy} = \sigma_{yx} = 0$
Remaining boundaries	
	$u_x = u_y = 0,$
	$\sigma_{zz} = 0$

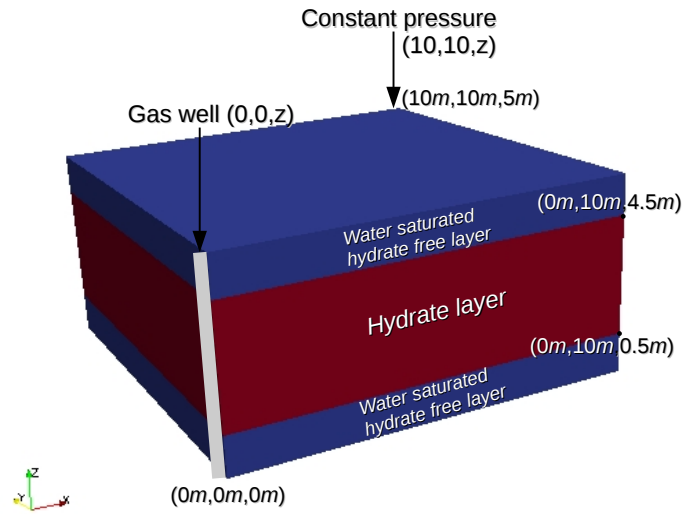


Figure 6.1: Schematic of depressurized 3D-reservoir example

Table 6.3: Material properties and model parameters for 3D-reservoir problem

Thermal conductivities		
k_g^c	$-0.886 \times 10^{-2} + 0.242 \times 10^{-3} T$ $-0.699 \times 10^{-6} T^2 + 0.122 \times 10^{-8} T^3$	$W \cdot m^{-1} \cdot K^{-1}$
k_w^c	$0.3834 \ln(T) - 1.581$	$W \cdot m^{-1} \cdot K^{-1}$
k_h^c	2.1	$W \cdot m^{-1} \cdot K^{-1}$
k_s^c	1.9	$W \cdot m^{-1} \cdot K^{-1}$
Specific heat capacities		
Cp_w	4186	$J \cdot kg^{-1} \cdot K^{-1}$
Cv_w	$Cp_w + R_{H_2O}$	$J \cdot kg^{-1} \cdot K^{-1}$
Cv_h	2700	$J \cdot kg^{-1} \cdot K^{-1}$
Cv_s	800	$J \cdot kg^{-1} \cdot K^{-1}$
Dynamic viscosities		
μ_g	$10.4 e-6 \left(\frac{273.15+162}{T+162} \right) \left(\frac{T}{273.15} \right)^{1.5}$	$Pa \cdot s$
μ_w	$0.001792 \exp \left[-1.94 - 4.80 \frac{273.15}{T} + 6.74 \left(\frac{273.15}{T} \right)^2 \right]$	$Pa \cdot s$
Densities		
ρ_g	$\frac{P_g}{zR_gT}$	$kg \cdot m^{-3}$
ρ_w	vapour: $0.0022 \frac{P_g}{T}$	$kg \cdot m^{-3}$

Continued on next page

Table 6.3 – Material properties and model parameters for 3D-reservoir problem (continued)

	liquid:	1000	$kg \cdot m^{-3}$
ρ_h	$900 \left[1 + \left(\frac{\alpha_{biot} - \phi}{1 - \phi} \right) \frac{\Delta P_{eff}}{B_{sh}} - \left(\frac{\lambda_{sh} + (2/3)G_{sh}}{B_{sh}} \right) \frac{\nabla \cdot \mathbf{u}}{1 - \phi_{eff}} \right]$		$kg \cdot m^{-3}$
ρ_s	$2100 \left[1 + \left(\frac{\alpha_{biot} - \phi}{1 - \phi} \right) \frac{\Delta P_{eff}}{B_{sh}} - \left(\frac{\lambda_{sh} + (2/3)G_{sh}}{B_{sh}} \right) \frac{\nabla \cdot \mathbf{u}}{1 - \phi_{eff}} \right]$		$kg \cdot m^{-3}$
Hydraulic properties			
λ_{BC}		1.2	
P_{entry}		50	kPa
m, a (Eqn. (2.12))		3, 2	
Hydrate kinetics			
k_{reac}^0		3.6×10^4	$mol \cdot m^{-2} \cdot Pa^{-1} \cdot s^{-1}$
$\Delta E_a/R$		9752.73	K
N_{Hyd}		5.75	
A_1, A_2, A_3 (Eqn. (2.21))		1000, 38.98, 8533.8	
B_1, B_2 (Eqn. (2.22))		56599, 16.744	
Γ_r (Eqn. (2.20))		ϕS_h	
Poroelasticity parameters			
α_{biot}		0.6	
ν_{sh}		0.2	
E_{s0}		0.3	GPa
E_h		1.35	GPa
b, c, d (Eqn. (2.26))		0, 1, 1	

6.2 Numerical simulation and results

The domain is discretized into $30 \times 30 \times 15$ cells. Full hydro-geomechanical model is solved. The decoupling strategy and iterative block Gauss-Seidel solution scheme described in Section 3.2 is used. The primary variables being solved for are: gas phase pressure P_g , aqueous phase saturation S_w , hydrate phase saturation S_h , temperature T , total porosity ϕ , and displacements \mathbf{u} . Some of the other important secondary variables which are calculated as post process include gas saturation S_g , effective porosity ϕ_{eff} , intrinsic permeability K , stresses $\tilde{\sigma}'$, strains $\tilde{\epsilon}$, etc. The simulation is run until $t_{end} = 24 \text{ hrs}$ with a time step size of $dt = 200 \text{ s}$.

Selected profiles showing the state of the reservoir at t_{end} are shown in Fig. 6.3. The low pressure in the gas well destabilizes the methane hydrate, which dissociates into methane gas and water. The pressure gradient draws the fluids towards the gas well. Fig. 6.3a shows the melted hydrate, and Fig. 6.3b shows the accumulated gas in the vicinity of the gas well. Fig. 6.3c shows the temperature distribution in the reservoir. The temperature drops in the zone where the hydrate is dissociating, due to the endothermic nature of hydrate dissociation. Fig. 6.3d shows the stress built up in the region around the well where the hydrate is dissociating. The model predicts that

the stresses are highest around the hydrate dissociation front. Fig. 6.3e and Fig. 6.3e show the change in effective porosity and intrinsic permeability as a result of hydrate dissociation and soil deformation. It can be seen that the effect of soil deformation on effective porosity and intrinsic permeability is quite significant. The vectors in Fig. 6.3 show the displacements \mathbf{u} . The domain is warped with respect to displacement to show the ground subsidence around the well clearly. The warping of the domain is achieved through post-processing using PARAVIEW [3].

6.3 Numerical solution using multirate time stepping

We now simulate this problem using the compound fast MRT method, and the semi-implicit MRT method with $p0$ polynomial extrapolation, and show the speed-up obtained in our calculations. We assume uniform, non-adaptive micro and macro time-grids, and chose the following values of the multirate factor,

$$m = [1, 2, 5, 10, 15, 30] .$$

The micro grid size is chosen as $h = 200$ s, and the macro grid size as $H = m h$.

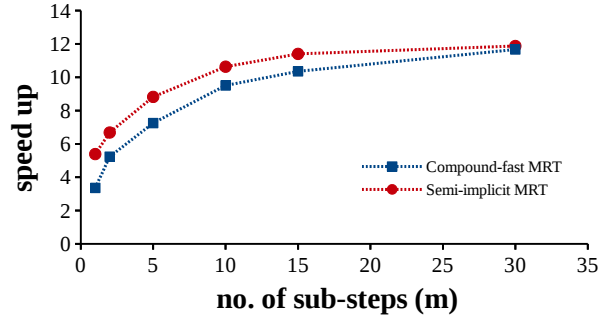


Figure 6.2: 3D hydrate reservoir problem

Speed up over m for the compound-fast MRT method, and the semi-implicit MRT method using $p0$ polynomial for extrapolation.

The speed-up is evaluated using Eqn. (5.1). Fig. 6.2 shows the *speed – up* vs. m curves obtained for the semi-implicit and the compound-fast MRT methods. We can see that, by using the MRT methods for time-integration we can get a significantly large speed up for the 3D case. For this problem, the CPU-time required to obtain the solution at t_{end} using compound-fast MRT method with $m = 30$ was approximately 12 hrs. In comparison, the CPU-time required by the iterative Gauss-Seidel scheme to obtain the solution with comparable accuracy was approximately 144 hrs.

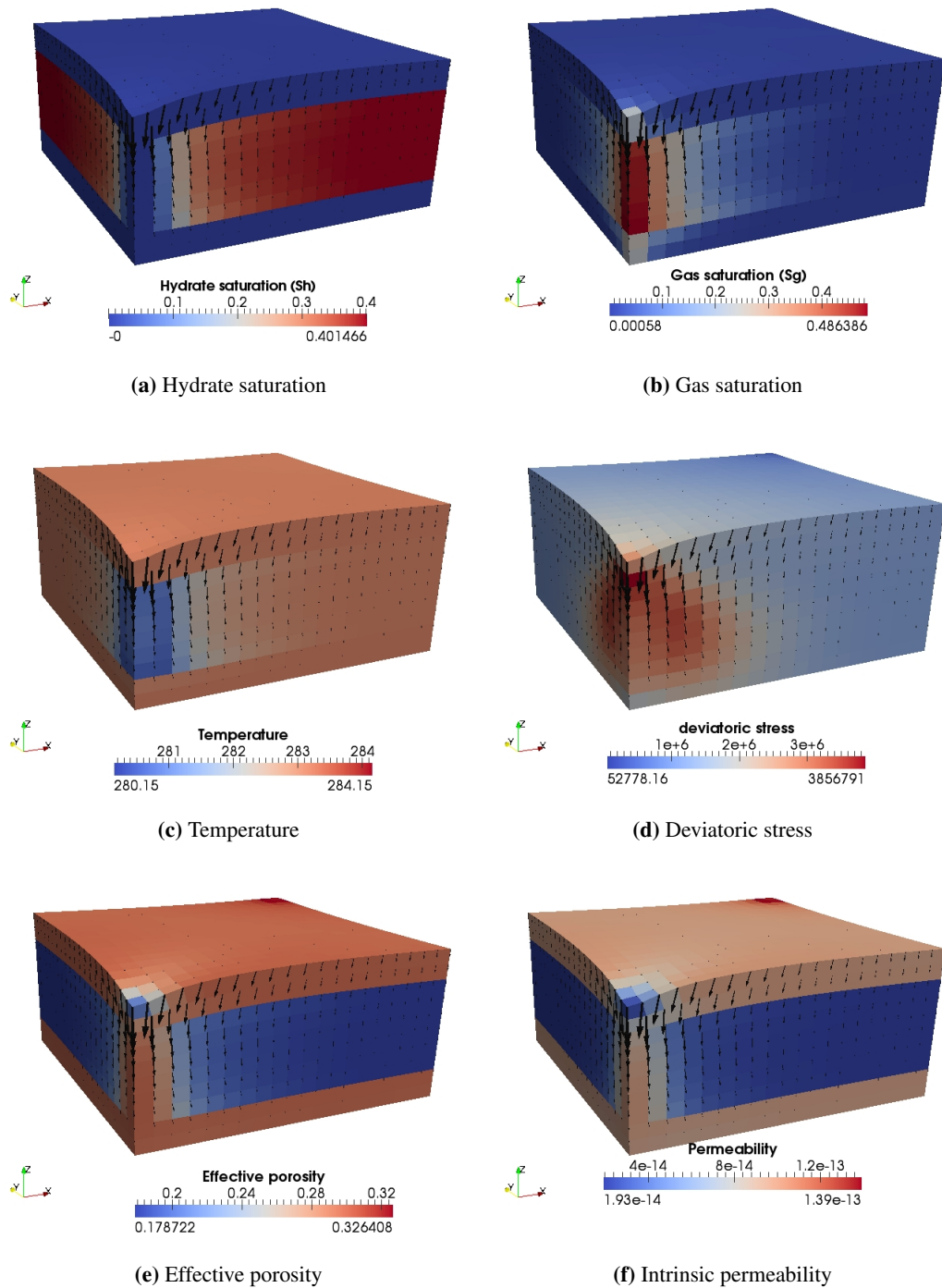


Figure 6.3: 3D hydrate reservoir problem
Selected profiles at t_{end}

Model verification using triaxial compression lab experiments

To reliably predict the mechanical behavior of gas hydrate-bearing sediments during gas production, numerical tools must be sufficiently calibrated against data from controlled experiments or field tests, and the capability of the hydrate reservoir model in handling the dynamic couplings observed in the lab/field scales must be thoroughly tested. To this effect, a combined experimental-numerical study was performed with the objective of testing the developed hydrate reservoir model against data from lab-scale experiments on methane hydrate formation and dissociation combined with high-pressure triaxial testing.

The experiments were performed by Christian Deusner at GEOMAR in Kiel, Germany. The experiments involved a controlled triaxial volumetric strain test on a sand sample in which methane hydrate was first formed under controlled effective stress and then dissociated via depressurization under controlled total stress. It has been assumed that this is realistic for natural settings where the gas hydrates form at increased hydrostatic pressure in relatively shallow, unconsolidated sediments at low effective stress, and depressurize under drained conditions without changing the sediment and bulk fluid overburden, thus, assuming gas hydrates being located in a highly permeable formation, which is confined by sediment regions of much lower permeability. In the experiment, the gas hydrate was initially formed by pressurizing partially water-saturated sand with gaseous methane to reach a gas hydrate saturation of 0.4, and remaining methane gas was replaced with seawater before the sample was depressurized stepwise. Confining and axial loads in triaxial testing were applied isotropically and controlled in a suitable manner to keep the deformation of the sample small; shear loads were not applied. Under these constraints, the concepts of poro-elasticity are assumed to be essentially valid.

In this chapter, we present a numerical simulation study for the above experiment using the hydro-geomechanical hydrate reservoir model and the numerical framework developed in Chapter 2 and Chapter 3, respectively. The focus of this numerical study is laid on testing how well

the linear elastic model can capture the dynamic coupling between the transport, chemical reaction, and mechanical processes observed during methane hydrate formation and dissociation in sandy soil under isotropic loading. The details of the experiment are summarized in Section 7.1. The test-setting, including the computational domain, material properties, and model parameters are detailed in Section 7.2.1, and the simulation results are presented in Section 7.2.2. Finally, in Section 7.3, we present a discussion on the results of our simulation. In particular, we take a closer look at the parameterization for composite Young's modulus, which showed a much stronger dependency on bulk gas hydrate saturation during gas hydrate formation. We also briefly analyze the differences of apparent stress-strain behavior observed during gas hydrate formation and dissociation periods, indicating that the gas hydrate-sediment structure and bulk hydrate distribution were largely different during these periods.

7.1 Materials and methods

7.1.1 Experimental set-up and components

Experiments were carried out in the custom-made high pressure apparatus NESSI (Natural Environment Simulator for Sub-seafloor Interactions, Deusner et al. 2012 [26]), which was equipped with a high-pressure triaxial cell mounted in a 40 L stainless steel vessel (APS GmbH Wille Geotechnik, Rosdorf, Germany). All wetted parts of the setup are made of stainless steel. Salt water medium was supplied from reservoir bottles (DURAN, Wertheim, Germany) using a HPLC pump S1122 (SYKAM, Fürstfeldbruck, Germany). Pressure was adjusted with a back-pressure regulator valve (TESCOM Europe, Selmsdorf, Germany). Experiments were carried out in upflow mode with injection of CH_4 gas and seawater medium at the bottom of the sample prior and after gas hydrate formation (Fig.7.1a), and fluid discharge at the top of the sample during depressurization (Fig.7.1b). Axial and confining stresses, and sample volume changes were monitored throughout the overall experimental period. Pore pressure was measured in the influent and the effluent fluid streams close to sample top and bottom. The experiment was carried out at constant temperature conditions. Temperature control was achieved with a thermostat system (T1200, Lauda, Lauda-Königshofen, Germany). Produced gas mass flow was analyzed with mass flow controllers (EL FLOW, Bronkhorst, Kamen, Germany). For control purposes, bulk effluent fluids were also collected inside 100 L gas tight TEDLAR sampling bags (CEL Scientific, Santa Fe Springs CA, USA). The sampling bags were mounted inside water filled containers. After expansion of the effluent fluids at atmospheric pressure, overall volume was measured as volume of water displaced from these containers.

7.1.2 Sample preparation and mounting

The sediment sample was prepared from quartz sand (initial sample porosity: 0.35, grain size: 0.1 – 0.6 mm, G20TEAS, Schlingmeier, Schwülper, Germany), which was mixed with deionized water to achieve a final water saturation of 0.4 relative to initial sample porosity. The partially water saturated and thoroughly homogenized sediment was filled into the triaxial sample cell equipped with a Viton sleeve to obtain final sample dimensions of 380 mm in height and 80 mm in diameter. Sample geometry was assured using a sample forming device. The sample

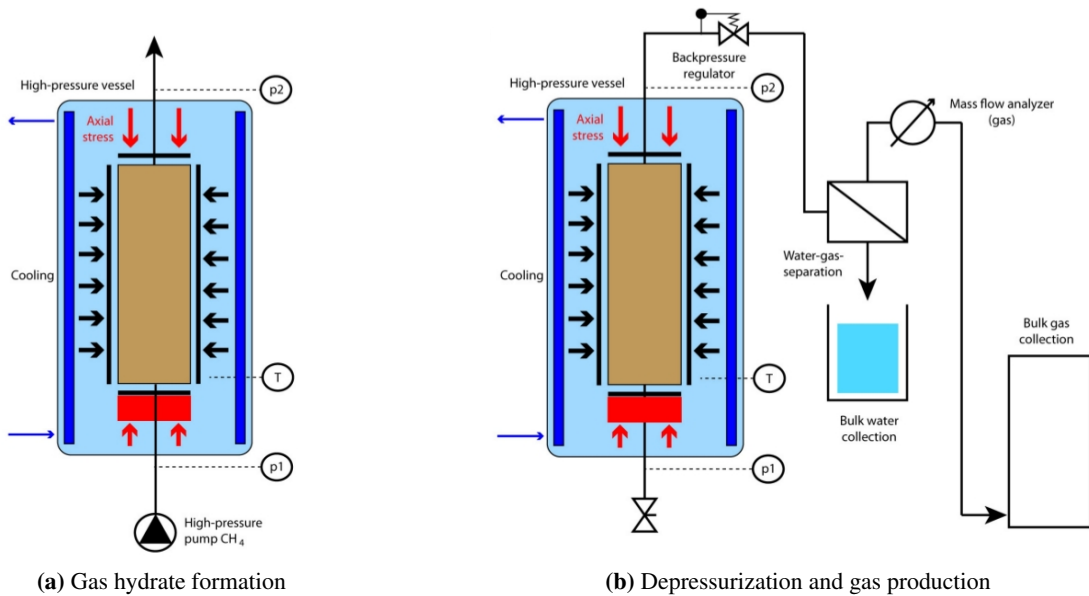


Figure 7.1: Simplified flow schemes for relevant experimental periods

was cooled to 2°C after the triaxial cell was mounted inside the pressure vessel. Initial water permeability of gas hydrate-free sediment was $5 \times 10^{-10} \text{ m}^2$.

7.1.3 Experimental procedure

Gas hydrate formation

Prior to gas hydrate formation the sediment sample was isotropically consolidated to 2 MPa effective stress under drained conditions. The sample was flushed with CH_4 gas and, subsequently, pressurized with CH_4 gas to approximately 12.5 MPa (Fig.7.1a). During pressurization with CH_4 gas and throughout the overall gas hydrate formation period, formation stress conditions of 2 MPa effective stress were maintained using an automated control algorithm. The formation process was continuously monitored by logging the CH_4 gas pressure. Mass balances and volume saturations were calculated based on CH_4 gas pressure and initial mass and volume values. Gas hydrate formation was terminated after 1.84 mol of CH_4 -hydrates had been formed after approximately 6 days, corresponding to CH_4 -hydrate saturation of 0.39. The sample was cooled to -5°C and stress control was switched to constant total isotropic stress control at approximately 9 MPa before the sample pore space was de-pressurized to atmospheric pressure and remaining CH_4 gas in the pore space was released. System re-pressurization and water saturation of pore space was achieved by instant filling and re-pressurization with pre-cooled (-1°C) saltwater medium according to seawater composition. Hydrate dissociation during the brief period of depressurization was minimized by taking advantage of the anomalous self-preservation effect, which reaches an optimum close to the chosen temperature (Stern et al. 2003 [98]). After completion of gas - water fluid exchange, the sample temperature was re-adjusted to 2°C .

Depressurization and gas production

The sample pore space was de-pressurized and gas produced by stepwise decrease of back pressure at constant isotropic total stress (Fig.7.1b). Overall fluid production (water and CH_4 gas) was monitored after de-pressurization at ambient pressure after temperature equilibration.

7.2 Numerical simulation

To simulate the hydrate formation and dissociation processes in the lab-scale triaxial compression experiment described in Section 7.1.3, we use the mathematical model and the numerical solution strategy developed in Chapter 2 and Chapter 3, respectively. The model considers kinetic hydrate phase change and non-isothermal, multi-phase, multi-component flow through poro-elastic porous medium, and accounts for the effect of hydrate phase change on the mechanical properties of the sediment, and also for the effect of sediment deformation on the fluid-solid interaction properties relevant to reaction and transport processes (e.g., reaction surface area, permeability, capillary pressure).

7.2.1 Computational domain and test-setting

Assuming that the sand sample is axially symmetric, a $2D$ radial plane of dimensions $360 \text{ mm} \times 40 \text{ mm}$ is chosen as the computational domain. The dimensions correspond to the physical size of the sample. The domain is discretized into 72×8 cells.

The overall experiment was carried out in four steps, viz. 1) *pre-consolidation*, 2) *gas hydrate formation*, 3) *pore-fluid exchange*, and 4) *depressurization*, as described in section 7.1.3. During steps 1 and 2, the sample was maintained under a defined effective loading with the confining and the axial stresses controlled to remain 10 bar above the pore pressure. However, during steps 3 and 4, the total isotropic stress was controlled to remain at a constant level. (See Fig. 7.2.) The experiment was performed over a total period of about 16.8 days. The *periods of interest* for the simulation in this study are: 1) from *Day* – 3 to *Day* – 10, corresponding to gas hydrate formation, and 2) from *Day* – 12.8 to *Day* – 13.8, corresponding to depressurization and gas production. We simulate both of these periods separately.

Gas hydrate formation period

The schematic of the hydrate formation test is shown in Fig.7.3. The schematic also shows the initial and boundary conditions. The simulation is run until $t_{end} = 604800 \text{ s}$ (i.e. 7 days) using a maximum time step size of 120 s.

Depressurization and gas production period

The schematic of the depressurization test is shown in Fig.7.4. The schematic also shows the initial and boundary conditions. The simulation is run until $t_{end} = 86400 \text{ s}$ (i.e. 1 day) using a maximum time step size of 120 s.

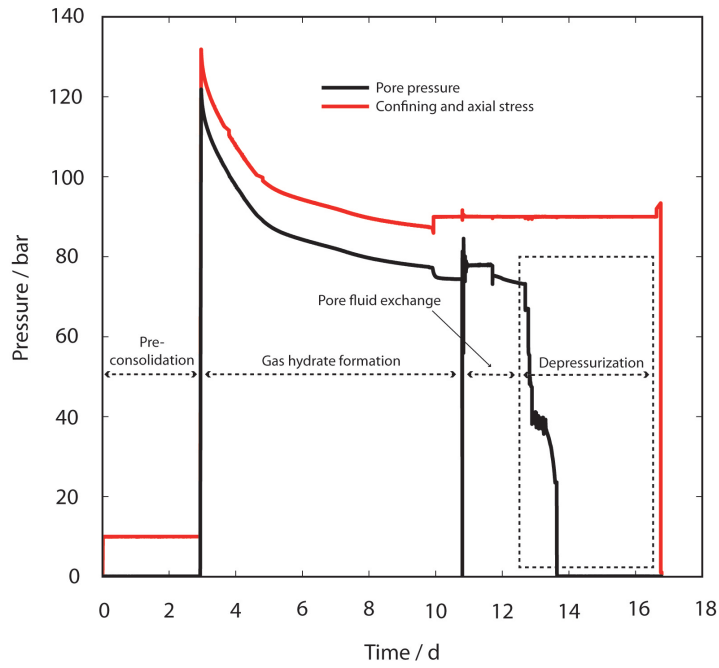


Figure 7.2: Overview of the *measured* pressure and stresses over time.

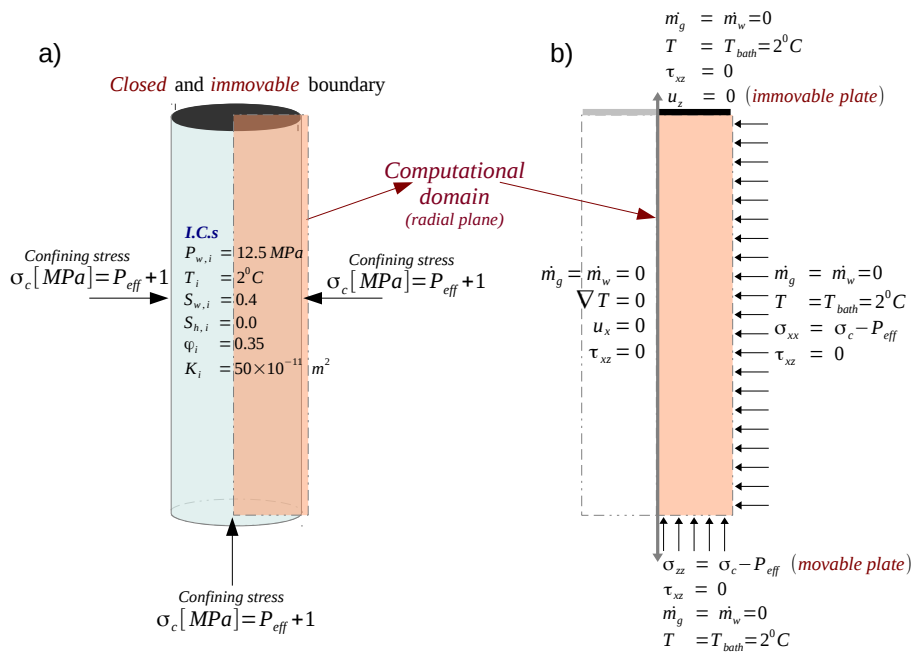


Figure 7.3: Test setting for the **gas hydrate formation** period.

a) shows the sample and the initial conditions, and b) shows the 2D computational domain and the boundary conditions.

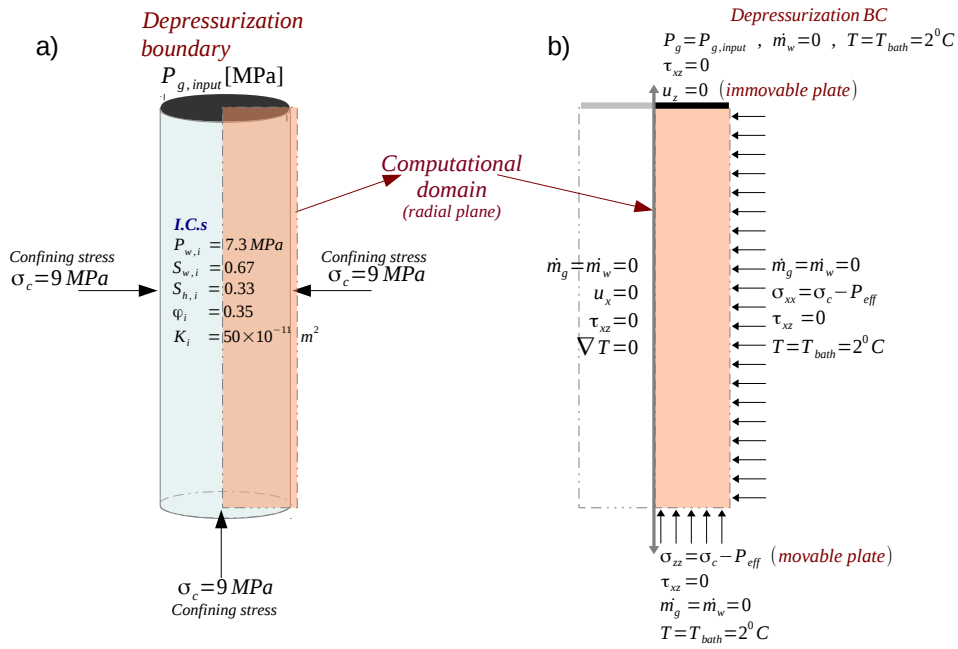


Figure 7.4: Test setting for the **depressurization and gas production** period. a) shows the sample and the initial conditions, and b) shows the 2D computational domain and the boundary conditions.

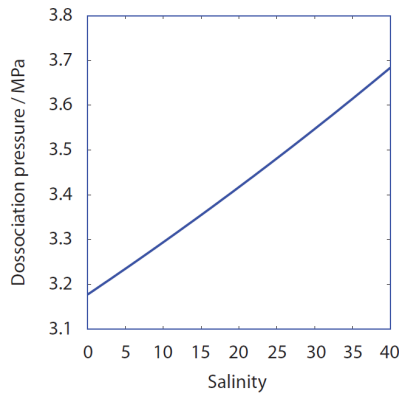


Figure 7.5: Effect of salinity on hydrate stability curve at $T_{bath} = 2^0 \text{ C}$

The important material properties and model parameters are listed in Table 7.1. The values of the thermal conductivities, specific heat capacities, dynamic viscosities, and densities for each phase are chosen from standard literature, the references to which are included in the table. The Brooks-Corey parameters are chosen from the range of typically expected values for sand samples. The most important properties/parameters relevant to the simulation of the experimental data arise from 1) the hydrate-phase-change kinetics, and 2) the poro-elastic behaviour of the hydrate bearing sediments.

The hydrate phase-change is modelled by Eqns. (2.17,2.18, and 2.22), described in Section 2.4.4. The hydrate-phase equilibrium pressure P_e in Eqn. (2.17) is modelled in accordance with the findings of Kamath et al. (1984) [44]. For hydrates in pure water, the equilibrium pressure depends only on the temperature. However, for hydrates in sea water (which is the case for our sample), the equilibrium pressure also depends on the salinity, as shown in Fig.7.5. We account for effect of salinity on the hydrate equilibrium pressure through linear curve fitting on dissociation pressure vs. salinity curve of Fig.7.5, as,

$$P_e[\text{MPa}] = P_{e,0} - 0.5 + \frac{0.5}{40} s^0, \quad (7.1)$$

where, $P_{e,0}$ is hydrate stability curve for pure water with no salinity given by Eqn. (2.21), s_i^0 is the initial salinity of the sea-water in our sample, i.e., $s_i^0 = 35$, and s^0 is the salinity of the sea-water in the sample after dilution as a result of production of pure water from the dissociation of hydrate. Salinity s^0 at any given time is derived using the following argument: The production of pure water reduces the salinity of the sea water in the sample. Assuming perfect mixing, for x amount of salt dissolved in the sea water,

$$x = s_i^0 V_{wi} = s^0 (V_{wi} + \Delta V_w)$$

where, V_{wi} is the initial volume of water in the sample, and ΔV_w is the volume of water produced due to hydrate dissociation. Using the hydrate kinetics and rearranging, we get the expression for salinity s^0 as,

$$s^0 = s_i^0 \left[1 + N_h \frac{\rho_h M_w}{\rho_w M_h} \left(\frac{S_{hi} - S_h}{S_{wi}} \right) \right]^{-1}$$

The reaction surface area, A_{rs} , in Eqn. (2.17), describes the surface area available for the kinetic-reaction, and puts a limit on the mass transfer during hydrate formation and dissociation. As the hydrate saturation in the pore-space increases, the availability of free surface for the hydrate formation to occur decreases, and vice versa. Additionally, for hydrate formation to occur, availability of both gas and water in sufficient quantities in the pore-space is a necessary condition. This behaviour of A_{rs} is modelled using the parameterization proposed by Sun and Mohanty (2006) [100], given by Eqn. (2.20). The rate of reaction, k_{reac} , is a *free parameter* in our simulation which is used to calibrate the hydrate-kinetics model with respect to the experimental data. In the table we can see that the values of k_{reac} , for both hydrate formation as well as dissociation periods, lie well within the range reported in the literature.

The poro-elastic behaviour of the hydrate-bearing sediment is characterized by three parameters, viz., Biot's constant α_{biot} , Poisson ratio ν_{sh} , and Young's modulus E_{sh} . Biot's constant is chosen from a range of typically expected values. The Poisson's ratio is assumed to be a constant independent of the hydrate saturation following the experimental studies by Miyazaki et al. (2011) [59]. The Young's modulus is modelled using the parameterization proposed by Santamarina and Ruppel (2010) [87], given by Eqn. (2.26). This parameterization is simplified to,

$$E_{sh} = E_s + S_h^d E_h ,$$

by assuming that the effects of confining stress and the pore-habit are implicitly contained in the choice of the Young's moduli E_s and E_h for this simulation.

The Young's moduli E_s and E_h are *free parameters* which are used to calibrate the poro-elasticity model with respect to the experimental data. For the formation period, E_s and E_h are chosen such that the simulated volumetric strain in the sample at the end of the formation period matches the experimentally measured value. For the dissociation period, E_s is chosen such that the simulated volumetric strain in the sample at the end of the dissociation period (i.e., when $S_h = 0$) matches the experimentally measured value, and E_{sh} is chosen such that the simulated volumetric strains in the sample at the end of the first and second depressurization steps matches the experimentally measured value. The choice of the exponent d is described in more detail in Section 7.3.

Table 7.1: Material properties and model parameters

Thermal conductivities			Ref.
k_g^c	$-0.886 \times 10^{-2} + 0.242 \times 10^{-3}T - 0.699 \times 10^{-6}T^2 + 0.122 \times 10^{-8}T^3$	$W \cdot m^{-1} \cdot K^{-1}$	[80]
k_w^c	$0.3834 \ln(T) - 1.581$	$W \cdot m^{-1} \cdot K^{-1}$	[1]
k_h^c	2.1	$W \cdot m^{-1} \cdot K^{-1}$	[94]
k_s^c	1.9	$W \cdot m^{-1} \cdot K^{-1}$	[29]
Specific heat capacities			
Cp_g	$\Delta Cp_g^{res} (1238 + 3.13T + 7.9 \times 10^{-4}T^2 - 6.86 \times 10^{-7}T^3)$	$J \cdot kg^{-1} \cdot K^{-1}$	[72, 29]
Cv_g	$Cp_g + R_{CH_4}$	$J \cdot kg^{-1} \cdot K^{-1}$	
Cp_w	4186	$J \cdot kg^{-1} \cdot K^{-1}$	[1]
Cv_w	$Cp_w + R_{H_2O}$	$J \cdot kg^{-1} \cdot K^{-1}$	

Continued on next page

Table 7.1 – Material properties and model parameters (*continued*)

Cv_h	2700	$J \cdot kg^{-1} \cdot K^{-1}$	[94]
Cv_s	800	$J \cdot kg^{-1} \cdot K^{-1}$	[29]
Dynamic viscosities			
μ_g	$10.4 \times 10^{-6} \left(\frac{273.15 + 162}{T + 162} \right) \left(\frac{T}{273.15} \right)^{1.5}$	$Pa \cdot s$	[30]
μ_w	$0.001792 \exp \left[-1.94 - 4.80 \left(\frac{273.15}{T} \right) + 6.74 \left(\frac{273.15}{T} \right)^2 \right]$	$Pa \cdot s$	[1]
Densities			
ρ_g	$\frac{P_g}{zR_gT}$	$kg \cdot m^{-3}$	[72]
ρ_w	vapour: $0.0022 \frac{P_g}{T}$ liquid: 1000	$kg \cdot m^{-3}$	[1]
ρ_h	900	$kg \cdot m^{-3}$	[94]
ρ_s	2100	$kg \cdot m^{-3}$	
Hydraulic properties			
λ_{BC}	1.2		[37]
P_{entry}	50	kPa	[37]
Hydrate kinetics			
k_{rec}	formation: 0.2×10^{-11} dissociation: 3.2×10^{-10}	$mol \cdot m^{-2} \cdot Pa^{-1} \cdot s^{-1}$	
N_{Hyd}	5.75		
$P_{e,0}$	$A_1 = 10^6, A_2 = 38.98, A_3 = 8533.8$	Pa	[43]
\dot{Q}_h	$B_1 = 56599, B_2 = 16.744$	$W \cdot m^{-3}$	[29]
Poroelasticity parameters			
α_{biot}	0.8		[108]
ν_{sh}	0.15		[59]
	formation	dissociation	
E_s	32	160	MPa
E_h	250	360	MPa
d	1	3	

7.2.2 Simulation results

As discussed in Sec. 7.2.1, we essentially chose *one* free parameter in kinetics, i.e., k_{reac} , and *one* free parameter in linear-elasticity, which is E_{sh} , to calibrate the kinetics and the mechanical models separately. With these calibrated models, we simulate numerically the coupled hydro-mechanical response of the sand sample in triaxial test-setting using our gas hydrate reservoir model. The numerical results, together with the corresponding experimental data, are plotted in Fig. 7.7 for the gas hydrate formation period, and in Fig. 7.8 for the hydrate dissociation period.

In the gas hydrate formation period, methane gas in the free pore space is continuously consumed and average bulk gas pressure is decreased. (See Fig. 7.7a.) The gas pressure recorded during the experiments was influenced by additional free volume space in inflow / outflow pipelines. During the hydrate formation, a substantial volume of gas (≈ 180 mL) was trapped in the dead spaces (e.g., in pipes and manifolds). This gas interacted with the sample and significantly damped the pressure decay during to hydrate formation. We account for this effect in our simulation by introducing an additional source term for methane gas, $S_{ext}^{CH_4}$, in the mass balance PDE for CH_4 . The rationale behind adding this source term is the following:

- The dead space has a fixed volume of $V_{ext} = 180$ ml, and at the start of the experiment it is filled with methane gas.

Mass of methane in the dead space is $m_{g,ext} = \rho_g(P_{ext}, T_{ext}) V_{ext}$, and the rate of change of gas mass is $\frac{\partial}{\partial t} m_{g,ext} = V_{ext} \frac{\partial}{\partial t} \rho_g(P_{ext}, T_{ext})$.

- Assuming that the pressure and temperature in the system (sample+dead space) equilibrate very fast, we can say $P_{ext} = P_g$ and $T_{ext} = T$. So, the rate of change of mass of methane gas in the dead space can be expressed as,

$$\frac{\partial}{\partial t} m_{g,ext} = V_{ext} \frac{\partial}{\partial t} \rho_g(P_g, T) = V_{ext} \frac{\rho_g(P_g, T)}{B_g} \frac{\partial}{\partial t} P_g$$

where, B_g is the bulk modulus of methane gas.

- Since the dead space+sample together form a closed system, any change of mass in the dead space must be due to transport of gas from dead space into the sample. Assuming that this transport is very fast, we can introduce a volumetric source term $S_{ext}^{CH_4}$ s.t.,

$$S_{ext}^{CH_4} = \frac{1}{V_s} \frac{\partial}{\partial t} m_{g,ext} = \frac{V_{ext}}{V_s} \frac{\rho_g(P_g, T)}{B_g} \frac{\partial}{\partial t} P_g$$

where, V_s is the sample volume.

In Fig. 7.6, the average gas pressure in the domain which is simulated without accounting for the gas in the dead spaces has been plotted. We can see clearly that the dead volume of the gas damped the gas pressure decay significantly, and could not be ignored.

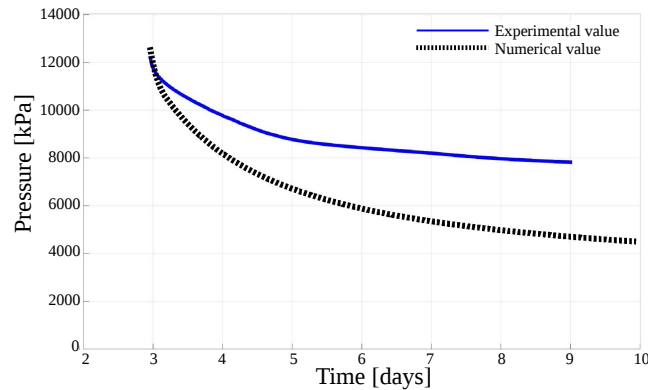


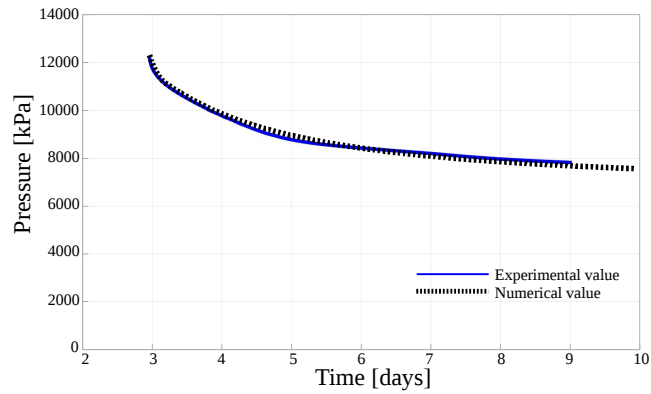
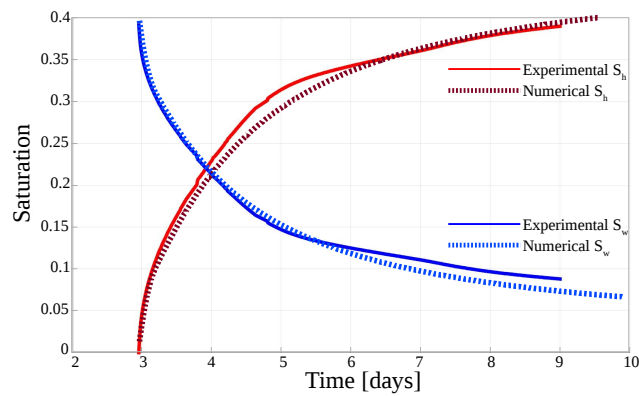
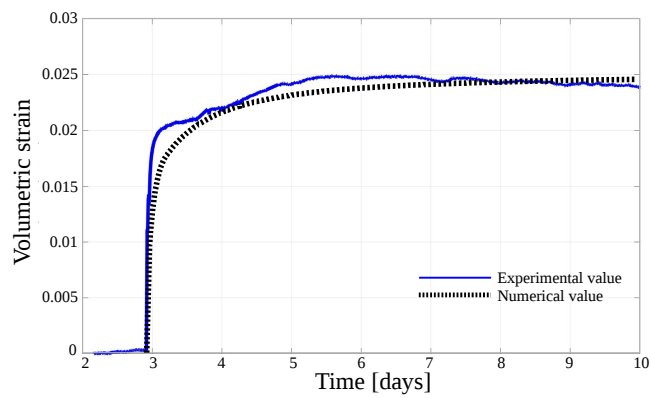
Figure 7.6: Average gas pressure for the **gas hydrate formation** period **without** accounting for the gas trapped in the dead spaces.

In Fig. 7.7b, the numerically computed and experimentally recorded values of average hydrate and water phase saturations are plotted over the hydrate formation period. Clearly, the rate of gas hydrate formation is not constant. In the beginning, after the sample is pressurized at constant isotropic effective stress, gas hydrate formation from free methane gas and pore water is fast, but the rate of formation steadily decreases due to mass transfer limitations and shrinking reaction surfaces. In accordance to that, after pressurization the gas hydrate saturation increases rapidly and the water saturation decreases proportionally. In Fig. 7.7c, the volumetric strain is plotted over the hydrate formation period. The volumetric strain at constant effective stress shows a fast positive response during early gas hydrate formation at relatively low gas hydrate saturation, and sample stiffness increases at higher gas hydrate saturation.

During the gas hydrate dissociation period, pressure is decreased step-wise until methane hydrates become unstable at the respective P-/T-conditions. Fig. 7.8a shows the numerically computed gas phase pressure in the sample. The gas production is plotted in Fig. 7.8b. With the onset of gas hydrate dissociation after reaching the hydrate stability boundary, pressure is maintained at a relatively constant level because hydrate dissociation and gas production equilibrate dependent on experimental and technical conditions.

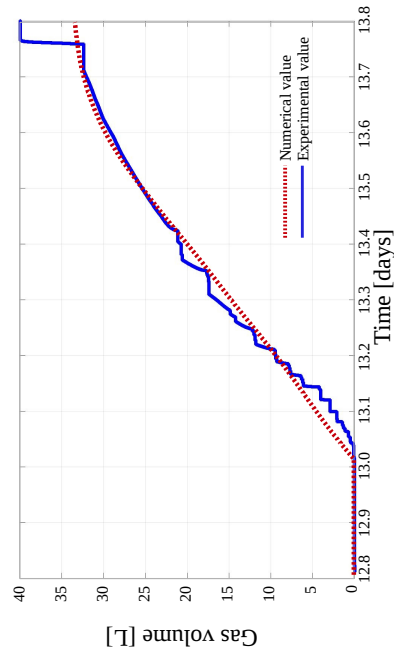
Volumetric strain during gas hydrate dissociation, plotted in Fig. 7.8c, is dependent on effective stress and gas hydrate saturation through the sample stiffness, which decreases with the ongoing gas hydrate dissociation and gas production.

To show the thermal aspect of the simulation, the numerically computed temperature profile of the sample during dissociation is plotted in Fig. 7.8d. The model predicts that sub-cooling from gas hydrate dissociation occurs, but is negligibly small on the sample scale due to isothermal temperature control.

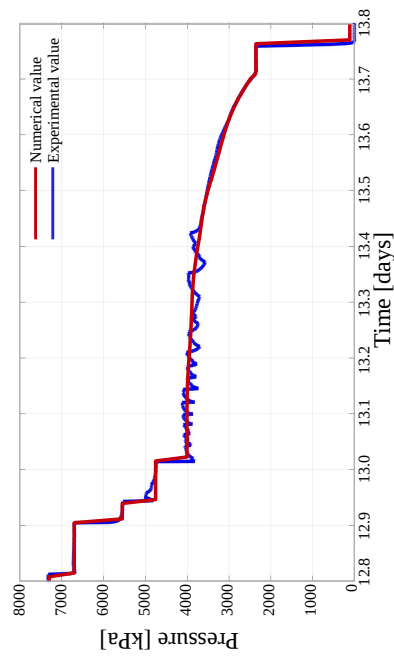
(a) Average P_g in the domain over time(b) Average S_w and S_h in the domain over time

(c) Total volumetric strain in the sample over time

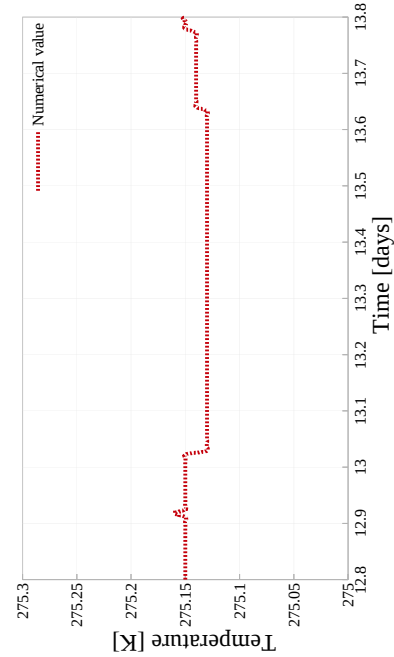
Figure 7.7: Comparison of the simulation results with the experimental results for the **gas hydrate formation** period.



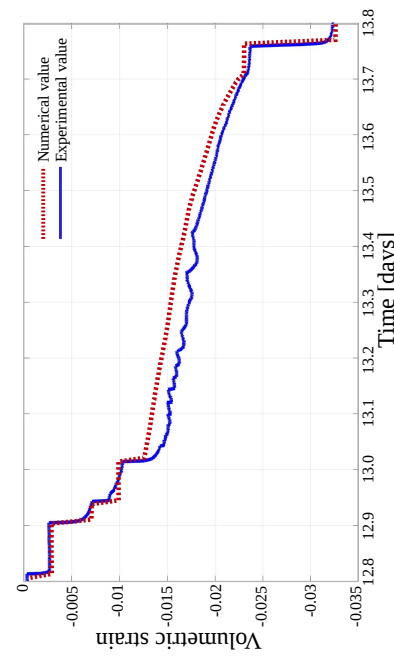
(a) P_g at depressurization boundary (at $z = 0$)



(b) Total volumetric strain in the sample over time



(c) P_g at depressurization boundary (at $z = 0$)



(d) Temperature in the sample over time

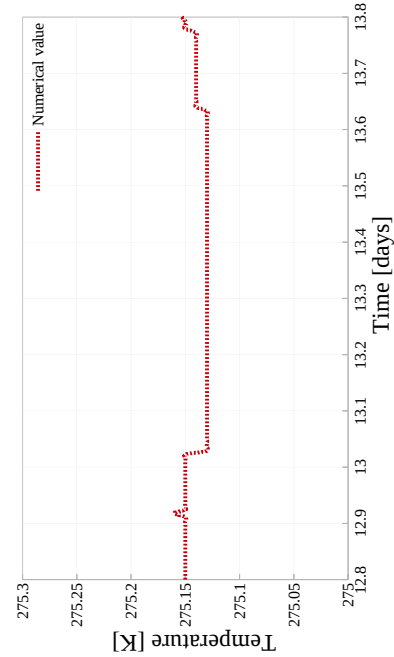


Figure 7.8: Comparison of the simulation results with the experimental results for the depressurization and gas production period.

7.3 Discussion

From the results presented above, we can see that the developed model is capable of reproducing the dynamic thermo-hydro-chemo-mechanical behavior of methane hydrate-bearing sandy sediments. The key behaviors include gas hydrate formation and gas production rates and yields, pressure and temperature response, and bulk volumetric yielding observed in our triaxial compression experiments during gas hydrate formation in partially water-saturated sediment, as well as hydrate dissociation via depressurization.

Overall, the experimental and simulation results on stress-strain behavior and elastic properties of gas hydrate-bearing sands are in accordance with earlier experimental and numerical studies, which reported Young's modulus or secant stiffness in a wide range of approximately 100 to 400 MPa for relevant gas hydrate concentrations (Brugada et al. 2010 [15], Miyazaki et al. 2010 [58], Santamarina et al. 2010 [53], Yun et al. 2007 [119]). Stiffness measured in the presence of THF hydrates appears to be higher than for CH_4 -hydrates in sediments. Young's modulus in our simulations tends to relatively low values compared to the published experimental and numerical data, and approaches values for dense soils. This limited absolute contribution of gas hydrates to overall stiffness might be due to different sample preparation and consolidation schemes, relatively low gas hydrate saturations, or due to using CH_4 instead of THF, which was frequently used in published studies. It was recently concluded that CH_4 -hydrate in soils does not reveal soil-cementing capabilities (Chaouachi et al. 2015 [18]), thus sediment stiffness can be expected to remain relatively unaffected at low gas hydrate saturations. However, this stress-strain behavior might also reflect differences in gas hydrate distribution and gas hydrate-soil fabrics. This aspect needs further evaluation in upcoming studies. We used a simple approach to describe composite Young's modulus E_{sh} , as being dependent on additive contributions of sand stiffness and gas hydrate stiffness, respectively. We have not included a contribution of effective stress conditions on the stiffness of gas hydrate-bearing sediment. Instead, we assume that during gas hydrate formation the effective stress is essentially constant, and during gas hydrate dissociation the stiffness of the sand is dominated by over-consolidation during gas-water exchange. Thus, effective stress effects on stiffness were assumed to be captured by adjusting Young's modulus of the soil matrix during gas hydrate formation and dissociation, respectively. Although the Young's modulus was treated as a free fitting parameter and initialized based on apparent stress-strain behavior during intervals of known and constant gas hydrate saturations, physically meaningful values for individual moduli E_s and E_h were obtained. The Young's modulus E_s for the sediment without gas hydrate reflected stiffness behavior typical for loose soil during gas hydrate formation while the sample was normally consolidated at low effective stress. In contrast, during the period of gas hydrate dissociation, gas hydrate-free sediment behaved like dense soil. This apparent step-like change of E_{sh} from 132 MPa to 183 MPa between gas hydrate formation and depressurization periods was presumably caused by over-consolidation during gas-water exchange at the end of the gas hydrate formation period. Thus, the gas hydrate-sand composite became stiffer without formation of additional gas hydrate.

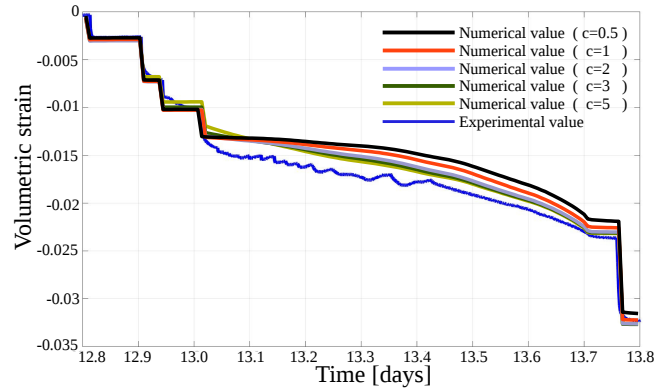


Figure 7.9: Volumetric strain curves for different functional dependences of E_{sh} on S_h (i.e. $d = 1, 2, 3, 5$) for the **depressurization and gas production** period.

The composite modulus E_{sh} depends almost linearly on S_h during gas hydrate formation, while during the hydrate dissociation period the dependence of E_{sh} on S_h is smaller. Fig. 7.9 shows the volumetric-strain plotted over time for the depressurization period for different functional dependences of E_{sh} on S_h (i.e. $d = 0.5; 1; 2; 3; 5$). Our simulation results indicate that an exponent $d = 3$ is a reasonable approximation. Santamarina and Ruppel (2010) [87] suggest that S_h tends to be raised to a power larger than 1, which reduces the impact on stiffness at low gas hydrate saturations relative to that for high gas hydrate saturations. Since we expect that gas hydrates formed in our procedure are predominantly located in the pore throats rather than in the free pore space, the linear and relatively strong dependence of E_{sh} on S_h appears reasonable. Under the initial conditions of only partial water saturation of the soil, the formed CH_4 -hydrate is assumed to contribute to the stiffness of the soil skeleton even at low gas hydrate saturations. This effect is further enhanced in weakly consolidated sediments, in which stiffness of the soil itself is low. The weak dependence of E_{sh} on gas hydrate saturation during dissociation appears also reasonable, since after exchanging gas with water in the pore space, gas hydrate-sediment fabrics will be steadily altered, and also during dissociation the grain-scale hydrate-sand structure is presumably changed. The mechanical implications of these structural transitions in gas hydrate-bearing sands during gas hydrate aging and dissociation are important issues. Any prediction of such dynamic changes in gas hydrate structure or its transient effects on geomechanics is yet not explicitly accounted for in our model, and needs further investigation.

For this experiment we have also ignored the effects of pore pressure and confining stresses on E_{sh} and other elastic material properties of the composite matrix. We have assumed that mechanical behavior of gas hydrate-bearing sands is dominated by gas hydrate saturation and effective stress conditions rather than by pore or cell pressure which is in accordance to earlier findings (Miyazaki et al. 2011 [59]). However, contrasting results showing strengthening effects of high pore or confining pressures have also been reported (Song 2014 [96], Hyodo 2013 [40]).

Poisson ratio is treated as a constant in our study, and its value chosen for gas hydrate-bearing sediments is in accordance with earlier studies (Miyazaki et al. 2011 [59], Lee et al. 2010 [54]). The Poisson ratio is of particular importance for the mechanical behavior under shear load and will be evaluated in more detail in upcoming studies by considering axial and lateral deformations along with bulk volume yielding.

Outlook

The presence of gas hydrates influences the stress-strain behavior and increases the load-bearing capacity of sub-marine sediments. This stability is reduced or completely lost when gas hydrates become unstable. Since natural gas hydrate reservoirs are considered as potential resources for gas production on industrial scales, there is a very strong need for numerical simulators with geomechanical capabilities. To reliably predict the mechanical behavior of gas hydrate-bearing sediments during gas production, numerical tools must be sufficiently calibrated against data from controlled experiments or field tests, and the models must consider thermo-hydro-chemo-mechanical process coupling in a suitable manner. In this thesis, we have presented a multiphysics hydro-geomechanical model for subsurface methane hydrate systems, with a focus on the gas production application. The model considers kinetic hydrate phase change and non-isothermal, multi-phase, multi-component flow in elastically deforming soils. The model accounts for the effect of hydrate phase change and pore pressure changes on the mechanical properties of the soil. It also accounts for the effect of soil deformation on the fluid-solid interaction properties relevant to reaction and transport processes (e.g., permeability, capillary pressure, reaction surface area). We have developed a numerical solution framework, and validated the numerical implementation of the model. We have also validated the model against experimental data from a controlled triaxial volumetric strain test on a sediment sample in which methane hydrate is first formed under controlled isotropic effective stress and then dissociated via depressurization under controlled total stress. The numerical results show that the dynamic coupling between transport, reaction, and mechanical processes during methane hydrate formation and dissociation in sandy sediment is captured well, and experimental gas production, dynamic volumetric strain and pressure response were closely reproduced. The model, however, has certain limitations and constraints which need to be addressed in the future to improve the quality and reliability of its predictions.

We have assumed that the sediment matrix behaves as a *linear* elastic material. This assumption holds true only for relatively stiff soils under small loads. In the triaxial volumetric strain test used for model validation, the sample deformations were kept small such that the concepts of poro-elasticity were essentially valid. For more realistic settings, however, we must include

rate-independent plasticity models emanating from Mohr-Coulomb and critical state plasticity theories in our hydrate reservoir model to model the mechanical behaviour of the sediment matrix.

One of the key assumptions in our hydrate reservoir model is that the methane hydrate perfectly coats the sand grain and the load is borne by sand-hydrate composite matrix. The recent experimental studies on the microstructure of the natural gas hydrates by Chaouachi et al. (2015) [18], however, show that a fluid phase film of up to several micron thickness appears between gas hydrates and the surface of the sand grains. These microstructural findings suggest that the assumption of grain-coating hydrates is not completely valid, and new modelling concepts must be developed to account for these findings in our hydrate reservoir model.

A serious flow assurance and wellbore stability issue that has emerged with regard to the field applicability of the depressurization method is the production of sand and fine particles that accompany the production of gas and water by hydrate dissociation in sedimentary layers. In Canada's Mallik field in the Alaskan permafrost, the test had to be stopped because of uncontrolled sand production. The test was resumed after well completion system was redesigned to consider the control of sand production. In the marine test in the Nankai Trough of Japan too, a significantly large sand production was observed at the end of the test. The production of sands and fines is detrimental to the productivity of the production wells as it increases the maintenance and operational costs. To design effective sand control methods, it is imperative to develop modelling approaches that predict the sand flow and production behaviour in relation to the production conditions. The flow behavior of sands is typically modelled using constitutive theories amenable to viscous flow, e.g., Bingham fluid. The modelling concepts that bridge the critical state behaviour and the viscous flow behaviour of sands (e.g., Andrade et al. (2012) [5], and Pailha and Pouliquen (2009) [70]) are of particular interest for our hydrate reservoir model.

There is also a large scope for improving the quality of the numerical solution and the efficiency of the computations in our hydrate reservoir simulator. For instance, in the cell centered finite volume (FV) approximation used for the spatial discretization of the flow model, we have used the linear two-point flux approximation (TPFA) to evaluate the diffusive fluxes across the cell boundaries. The TPFA schemes are, in general, more appealing than the MPFA (multi-point flux approximation) schemes due to the compact stencil of the FV discretization. The linear TPFA, however, does not provide an approximation for the case of non-orthogonal grids or for full anisotropic permeability tensors. It would, therefore, be of interest to consider non-linear TPFA schemes (e.g., Nikitin et al. (2013) [67],) which are less sensitive to grid distortions and provide approximations for fully anisotropic permeability fields. It would also be attractive, in terms of savings in computational work, to extend the multirate time-stepping (MRT) algorithms developed in Section 3.3 by considering space and time adaptive meshes similar to the methods developed by Osher and Sanders (1983) [69], Sandu and Constantinescu (2007) [21], Savcenco (2008) [91], etc.

An exhaustive parameter sensitivity analysis and model calibration for kinetic rates of dissociation and formation, and parameterization for apparent linear elasticity parameters, viz. E_{sh} and ν_{sh} , are also in line to improve the reliability of the predictions on field scale using our hydrate reservoir model in future.

Appendix A

Derivation of storage Eqn. (4.6)

We re-write the mass conservation equations for gas and water phase-wise, i.e., for each fluid-phase $\alpha = g, w$,

$$\frac{\partial}{\partial t} (\phi \rho_\alpha S_\alpha) + \nabla \cdot (\phi \rho_\alpha S_\alpha \mathbf{v}_{\alpha,t}) = \dot{q}_\alpha \quad (\text{A.1})$$

where, \dot{q}_α is the volumetric source term for phase α given as $\dot{q}_\alpha = \sum_\alpha (\chi_\alpha^\kappa \dot{g}^\kappa)$.

Expanding the partial derivatives in Eqn. (A.1) and rearranging gives

$$\begin{aligned} \phi S_\alpha \underbrace{\left(\frac{\partial}{\partial t} \rho_\alpha + \mathbf{v}_{\alpha,t} \cdot \nabla \rho_\alpha \right)}_{\frac{d}{dt} \rho_\alpha} + \rho_\alpha \frac{\partial}{\partial t} (\phi S_\alpha) + \rho_\alpha \nabla \cdot (\phi S_\alpha \mathbf{v}_{\alpha,t}) &= \dot{q}_\alpha \\ \Rightarrow \phi S_\alpha \frac{d}{dt} \rho_\alpha + \rho_\alpha \frac{\partial}{\partial t} (\phi S_\alpha) + \rho_\alpha \nabla \cdot (\phi S_\alpha \mathbf{v}_{\alpha,t}) &= \dot{q}_\alpha . \end{aligned} \quad (\text{A.2})$$

The rate of change of the fluid density is defined as $\frac{d}{dt} \rho_\alpha = \frac{\rho_\alpha}{B_\alpha} \frac{d}{dt} P_\alpha$, where, B_α is the fluid-phase bulk modulus. Using this definition in Eqn. (A.2) and dividing by ρ_α , we get

$$\frac{\phi S_\alpha}{B_\alpha} \frac{d}{dt} P_\alpha + \frac{\partial}{\partial t} (\phi S_\alpha) + \nabla \cdot (\phi S_\alpha \mathbf{v}_{\alpha,t}) = \frac{\dot{q}_\alpha}{\rho_\alpha} . \quad (\text{A.3})$$

Since we assume $P_c = 0$, the phase pressures are equal. So we drop the subscript and assign the symbol P to the phase pressures.

Next, we sum Eqn. (A.3) over $\alpha = g, w$, which gives

$$\phi \left(\frac{S_w}{B_w} + \frac{S_g}{B_g} \right) \frac{d}{dt} P + \frac{\partial}{\partial t} [\phi (S_w + S_g)] + \nabla \cdot (\phi S_w \mathbf{v}_{w,t}) + \nabla \cdot (\phi S_g \mathbf{v}_{g,t}) = \frac{\dot{q}_w}{\rho_w} + \frac{\dot{q}_g}{\rho_g} . \quad (\text{A.4})$$

We define the effective fluid-phase saturation $S_{\alpha,e}$ as the volume of fluid phase $\alpha = g, w$ in the *effective pore space* which is characterized by the effective porosity ϕ_e . So, $S_{\alpha,e} = \frac{S_\alpha}{1 - S_h}$, and $\phi_e = \phi(1 - S_h)$. Also, by the summation relationship, $S_w + S_g = 1 - S_h$, or $\frac{S_w}{1 - S_h} + \frac{S_g}{1 - S_h} = 1$.

Substituting these definitions in Eqn. (A.4), we get Eqn. (A.5) which we will call the *fluid mass balance equation*.

$$\phi_e \left(\frac{S_{w,e}}{B_w} + \frac{S_{g,e}}{B_g} \right) \frac{d}{dt} P + \frac{\partial}{\partial t} \phi_e + \nabla \cdot (\phi_e S_{w,e} \mathbf{v}_{w,t}) + \nabla \cdot (\phi_e S_{g,e} \mathbf{v}_{g,t}) = \frac{\dot{q}_w}{\rho_w} + \frac{\dot{q}_g}{\rho_g}. \quad (\text{A.5})$$

For the hydrate and the soil phases, the mass conservation equations (Eqn. (2.2) and Eqn. (2.3)) described in Section 2.3 are used. Adding Eqn. (2.2) and Eqn. (2.3), we get

$$\begin{aligned} & \frac{\partial}{\partial t} [\phi S_h \rho_h + (1 - \phi) \rho_s] + \nabla \cdot [\phi S_h \rho_h + (1 - \phi) \rho_s] \mathbf{v}_s = \dot{q}_h \\ \implies & \frac{\partial}{\partial t} (1 - \phi_e) \rho_{sh} + \nabla \cdot [(1 - \phi_e) \mathbf{v}_s] = \dot{q}_h. \end{aligned} \quad (\text{A.6})$$

Eqn. (A.6) is the mass balance relationship for the *hydrate-soil-composite* matrix. Expanding the derivatives in Eqn. (A.6) and rearranging gives

$$\begin{aligned} & (1 - \phi_e) \underbrace{\left[\frac{\partial}{\partial t} \rho_{sh} + \mathbf{v}_s \cdot \nabla \rho_{sh} \right]}_{\frac{d}{dt} \rho_{sh}} - \rho_{sh} \frac{\partial}{\partial t} \phi_e + \rho_{sh} \nabla \cdot [(1 - \phi_e) \mathbf{v}_s] = \dot{q}_h \\ \implies & (1 - \phi_e) \frac{d}{dt} \rho_{sh} - \rho_{sh} \frac{\partial}{\partial t} \phi_e + \rho_{sh} \nabla \cdot [(1 - \phi_e) \mathbf{v}_s] = \dot{q}_h. \end{aligned} \quad (\text{A.7})$$

Using the expression for rate of change of density of the composite matrix from Eqn. (2.27) in Eqn.(A.7), we get

$$\frac{\partial}{\partial t} \phi_e = \frac{1}{B_{sh}} \frac{d}{dt} \sigma - \frac{\phi_e}{B_{sh}} \frac{d}{dt} P + \nabla \cdot [(1 - \phi_e) \mathbf{v}_s] - \frac{\dot{q}_h}{\rho_{sh}} \quad (\text{A.8})$$

where, B_{sh} is bulk modulus of the composite solid.

Eqn. (A.8) describes the rate of change of the effective porosity due to external stress σ and internal fluid pore-pressure P . Finally, substituting Eqn. (A.8) in Eqn. (A.5), we obtain

$$\begin{aligned} & \phi_e \left[\left(\frac{S_{w,e}}{B_w} - \frac{S_{w,e}}{B_{sh}} \right) + \left(\frac{S_{g,e}}{B_g} - \frac{S_{g,e}}{B_{sh}} \right) \right] \frac{d}{dt} P + \frac{1}{B_{sh}} \frac{d}{dt} \sigma \\ & + \nabla \cdot [\phi_e S_{w,e} (\mathbf{v}_{w,t} - \mathbf{v}_s)] + \nabla \cdot [\phi_e S_{g,e} (\mathbf{v}_{g,t} - \mathbf{v}_s)] \\ & + \nabla \cdot \mathbf{v}_s = \frac{\dot{q}_w}{\rho_w} + \frac{\dot{q}_g}{\rho_g} + \frac{\dot{q}_h}{\rho_{sh}}. \end{aligned} \quad (\text{A.9})$$

Table A.1: Simplified constitutive relationships

Hydrate reaction kinetics	$\dot{q}_g = k_0 A_s M_g (P_e - P)$ $A_s = A_{s,0} \times S_h$ $\dot{q}_w = N_h \frac{M_w}{M_g} \dot{q}_g, -\dot{q}_h = \frac{M_h}{M_g} \dot{q}_g$
Darcy velocity	$\mathbf{v}_{\alpha,r} = -K \frac{k_{r,\alpha}}{\mu_\alpha} \nabla P$ $k_{r,g} = k_{r,w} = 0.5$
Effective stress principle	$\tilde{\sigma} = \tilde{\sigma}' + \alpha P \tilde{I}$ isotropic stress $\rightarrow \sigma = \sigma' + \alpha P$
Linear elastic stress-strain law	$\tilde{\sigma}' = -2G_{sh} \tilde{\epsilon} - \lambda_{sh} (tr \tilde{\epsilon}) \tilde{I}$ $\tilde{\epsilon} = \frac{1}{2} (\nabla \mathbf{u} + \nabla^T \mathbf{u})$ isotropic strain $\rightarrow \epsilon = \nabla \cdot \mathbf{u} = - \left(B_{sh} - \frac{4}{3} G_{sh} \right)^{-1}$ $\sigma = -(1/B_m) \sigma'$

Eqn. (A.9) expresses the *total mass balance* for the whole porous medium consisting of phases $\gamma = g, w, h, s$. We now substitute the simplified constitutive relationships listed in Table A.1 in Eqn. (A.9),

$$\begin{aligned}
& \phi_e \left[\left(\frac{S_{w,e}}{B_w} - \frac{S_{w,e}}{B_{sh}} \right) + \left(\frac{S_{g,e}}{B_g} - \frac{S_{g,e}}{B_{sh}} \right) \right] \frac{d}{dt} P + \frac{d}{dt} \epsilon \\
& + \frac{1}{B_{sh}} \left(\frac{d}{dt} \sigma' + \alpha \frac{d}{dt} P \right) - \nabla \cdot \left[K \left(\frac{k_{r,w}}{\mu_w} + \frac{k_{r,g}}{\mu_g} \right) \nabla P \right] \\
& = \left(N_h \frac{M_w}{\rho_w} + \frac{M_g}{\rho_g} - \frac{M_h}{\rho_{sh}} \right) k_0 A_{s,0} S_h (P_e - P) \\
\Rightarrow & \underbrace{\left[\phi_e \left(\frac{S_{w,e}}{B_w} + \frac{S_{g,e}}{B_g} \right) + \left(\frac{\alpha - \phi_e}{B_{sh}} \right) \right]}_{\text{Storativity } S} \frac{d}{dt} P + \underbrace{\left(1 - \frac{B_m}{B_{sh}} \right)}_{\alpha} \frac{d}{dt} \epsilon - \nabla \cdot \underbrace{\left(\frac{K}{2} \left(\frac{1}{\mu_w} + \frac{1}{\mu_g} \right) \right)}_{\frac{K}{\mu_f}} \nabla P \\
& = \underbrace{\left(N_h \frac{M_w}{\rho_w} + \frac{M_g}{\rho_g} - \frac{M_h}{\rho_{sh}} \right)}_C k_0 A_{s,0} S_h (P_e - P). \tag{A.10}
\end{aligned}$$

Eqn. (A.10) can be rewritten in a condensed form as

$$\alpha \frac{d}{dt} \epsilon + S \frac{d}{dt} P = \nabla \cdot \frac{K}{\mu_f} \nabla P + C S_h (P_e - P). \tag{A.11}$$

This is the *storage equation* describing the pressure response in a poroelastic hydrate soil.

Analytical solution for the Initial-Boundary-Value Problem (4.13)

This problem described in (4.13) is a homogeneous ODE with non-homogeneous boundary conditions. It can be transformed into two equivalent but simpler problems, viz., a steady state non homogeneous problem and a transient homogeneous problem.

To do this, we introduce new functions $v(z)$ and $w(z, t)$ such that

$$\bar{P}(z, t) = v(z) + w(z, t) \quad (\text{B.1})$$

We substitute (B.1) in (4.13), and get

$$\text{ODE 1: } C_v \frac{d^2}{dz^2} v(z) - C_r v(z) = 0 \quad (\text{B.2})$$

$$\text{and, ODE 2: } \frac{d}{dt} w(z, t) - C_v \frac{d^2}{dz^2} w(z, t) + C_r w(z, t) = 0 \quad (\text{B.3})$$

The transient ODE 2 is subjected to following boundary and initial conditions

$$w(0, t) = \bar{P}(0, t) - v(0) = (P_e - P^0) - v(0) \quad (\text{B.4})$$

$$\frac{d}{dz} w(L, t) = \frac{d}{dz} \bar{P}(L, t) - v(L) = -v(L) \quad (\text{B.5})$$

$$w(z, 0) = \bar{P}(z, 0) - v(z) = (P_e - P^0) - v(z) \quad (\text{B.6})$$

The function $v(z)$ is chosen such that the boundary conditions for the function $w(z, t)$ become homogeneous, i.e.,

$$\begin{aligned} \text{if, } w(0, t) = 0 \quad \text{and, } \frac{d}{dz} w(L, t) = 0 \\ \implies v(0) = P_e - P^0 \quad \text{and, } \frac{d}{dz} v(L) = 0 \end{aligned} \quad (\text{B.7})$$

To summarize,

ODE 1:

$$\begin{aligned} C_v \frac{d^2}{dz^2} v(z) - C_r v(z) &= 0 \\ v(0) &= P_e - P^0 \\ \frac{d}{dz} v(L) &= 0 \end{aligned}$$

ODE 2:

$$\begin{aligned} \frac{d}{dt} w(z, t) - C_v \frac{d^2}{dz^2} w(z, t) + C_r w(z, t) &= 0 \\ w(0, t) &= 0 \\ \frac{d}{dz} w(L, t) &= 0 \\ w(z, 0) &= (P_e - P^0) - v(z) \end{aligned}$$

Solution of ODE 1 gives

$$v(z) = (P_e - P^0) \frac{\cosh\left(\sqrt{\frac{C_r}{C_v}}(L - z)\right)}{\cosh\left(\sqrt{\frac{C_r}{C_v}}L\right)} \quad (\text{B.8})$$

Solution of ODE 2 gives

$$\begin{aligned} w(z, t) &= \sum_{n=1}^{\infty} C_n \sin(\lambda_n z) \exp[-C_v(\lambda_n^2 + \theta^2)t] \\ \text{where, } \lambda_n &= \left(n - \frac{1}{2}\right) \frac{\pi}{L}, \quad \text{and, } \theta = \sqrt{\frac{C_r}{C_v}} \end{aligned} \quad (\text{B.9})$$

The constant C_n is evaluated as

$$\begin{aligned} C_n &= \frac{2}{L} \int_0^L w(z, 0) \sin(\lambda_n z) dz \\ \implies C_n &= \frac{2}{L} (P_e - P^0) \frac{1}{\lambda_n} \left[1 - \frac{\lambda_n^2}{\lambda_n^2 + \theta^2}\right] \end{aligned} \quad (\text{B.10})$$

Therefore, the final solution for P can be written as

$$\begin{aligned} \frac{P_e - P(z, t)}{P_e - P^0} &= \frac{\cosh(\theta(L - z))}{\cosh(\theta L)} \\ &+ \frac{2}{L} \sum_{n=1}^{\infty} \left(\frac{1}{\lambda_n} \left[1 - \frac{\lambda_n^2}{\lambda_n^2 + \theta^2}\right] \sin(\lambda_n z) \exp[-C_v(\lambda_n^2 + \theta^2)t] \right) \end{aligned} \quad (\text{B.11})$$

List of Figures

1.1	Gas production methods from methane hydrates	2
2.1	Property averaged over different volumes.	8
2.2	Pore-scale to REV-scale	10
2.3	Methane hydrate P-T phase curve	16
3.1	'Cause-effect' based interaction between flow and geomechanical models.	22
3.2	Block Gauss-Seidel <i>outer</i> iterative solution loop	34
3.3	Time-mesh for active and latent components	36
4.1	Test 1 - Test setting for 1D experiment	41
4.2	Test 1 - Cumulative gas production curves for 1D experiment	42
4.3	Test 1 - Test setting for 2D experiment	43
4.4	Test 1 - Results for 2D experiment	44
4.5	Test 2 - Test setting	45
4.9	Test 2 - v_g profile (at $t = 30$ minutes)	46
4.6	Test 2 - S_g profile	47
4.7	Test 2 - S_g profile along diagonal line $X = Y$	48
4.8	Test 2 - S_g profile along X-axis (at $Y = 0.5$ m)	48
4.10	Test 3 - Terzaghi problem Schematic	49
4.11	Test 3 - Terzaghi benchmark test results	51
4.12	Test 4 - Hydrate stability curve shift at $t = 0$	52
4.13	Test 4 - Problem schematic	53
4.14	Test 4 - Computational domain settings	57
4.15	Test 4 - Comparison of numerical and analytical solutions	59
4.16	Test 4 - testID 3: L2-error vs n	60
4.17	Test 4 - testID 3: Time-evolution of the numerical solution of P along the height of the sample	60
5.1	Schematic of the 1D test problem	63

5.2	Relative error in P_g over m at $t = 18000$ sec for the semi-implicit fast-first MRT method using polynomials of order $p = 0, 1, 2, 3$ to approximate \mathbf{X}_G in the extrapolation steps.	64
5.3	Speed up in P_g over m for the semi-implicit fast-first MRT method using polynomials of order $p = 0, 1, 2$ to approximate \mathbf{X}_G in the extrapolation steps.	66
5.4	P_g and u_z profiles for fully-coupled (FC) scheme, iteratively-coupled (SEQ-it) scheme, and m -step semi-implicit MRT schemes using polynomial of order $p = 2$ for extrapolation.	67
5.5	Error in P_g plotted over m for different values of the C_v/C_r ratios for m -step semi-implicit MRT schemes using polynomial of order $p = 2$ for extrapolation.	68
5.6	Relative error and speed-up curves for the compound-fast MRT method and the semi-implicit MRT method using polynomial of order $p = 2$ for extrapolation.	70
6.1	Schematic of depressurized 3D-reservoir example	75
6.2	3D hydrate reservoir problem: Speed up over m for the compound-fast and the semi-implicit MRT methods	77
6.3	3D hydrate reservoir problem: Selected profiles at t_{end}	78
7.1	Simplified flow schemes for relevant experimental periods	81
7.2	Overview of the <i>measured</i> pressure and stresses over time.	83
7.3	Test setting for the gas hydrate formation period	83
7.4	Test setting for the depressurization and gas production period	84
7.5	Effect of salinity on hydrate stability curve at $T_{bath} = 2^0C$	84
7.6	Average gas pressure for the gas hydrate formation period <i>without</i> accounting for the gas trapped in the dead spaces	89
7.7	Comparison of the simulation results with the experimental results for the gas hydrate formation period	90
7.8	Comparison of the simulation results with the experimental results for the depressurization and gas production period	91
7.9	Volumetric strain curves for different functional dependences of E_{sh} on S_h for the depressurization and gas production period	93

List of Tables

3.1	Mass and Energy balance equations in terms of the generic conservation law, Eqn. (3.2)	25
4.1	Test 1 - Initial conditions for $1D$ experiment	41
4.2	Test 1 - Boundary conditions for $1D$ experiment	41
4.3	Test 1 - Kinetic parameters for $1D$ experiment	42
4.4	Test 1 - Kinetic parameters for $2D$ experiment	43
4.5	Test 2 - Model parameters	46
4.6	Test 3 - Solid-matrix properties	50
4.7	Test 3 - Fluid properties	50
4.8	Test 4 - Material properties	57
4.9	Test 4 - Control parameters	58
5.1	Material properties and model parameters	62
6.1	Initial conditions for depressurized $3D$ -reservoir example	74
6.2	Boundary conditions for depressurized $3D$ -reservoir example	74
6.3	Material properties and model parameters for $3D$ -reservoir problem	75
7.1	Material properties and model parameters	86
A.1	Simplified constitutive relationships	101

Bibliography

- [1] Iapws industrial formulation 1997 for the thermodynamic properties of water and steam. In *International Steam Tables*, pages 7–150. Springer Berlin Heidelberg, 2008.
- [2] G. Ahmadi, C. Ji, and H.S. Duane. Numerical solution for natural gas production from methane hydrate dissociation. *J. Pet. Sci. Eng.*, 41:169–185, 2004.
- [3] J. Ahrens, B. Geveci, and C. Law. chapter ParaView: An End-User Tool for Large Data Visualization. Elsevier, 2005.
- [4] B. Anderson, R. Boswell, Collett T.S., H. Farrell, S. Ohtsuki, M. White, and M. Zyrianova. Review of the findings of the ignik sikumi co₂-ch₄ gas hydrate exchange field trial. In *Proceedings of the 8th International Conference on Gas Hydrates*, Beijing, China, 2014. ICGH8.
- [5] JosÃ E. Andrade, Qiushi Chen, Phong H. Le, Carlos F. Avila, and T. Matthew Evans. On the rheology of dilative granular media: Bridging solid- and fluid-like behavior. *Journal of the Mechanics and Physics of Solids*, 60(6):1122–1136, 2012.
- [6] D. Archer, B. Buffett, and V. Brovkin. Ocean methane hydrates as a slow tipping point in the global carbon cycle. *Proc. Nat. Acad. Sci. USA*, 106:20596–20601, 2009.
- [7] P. Atkins and J. de Paula. *Physical Chemistry*. Oxford University Press, 8 edition, 2006.
- [8] Y. Bai, Q. Li, Y. Zhao, X. Li, and Y. Du. The experimental and numerical studies on gas production from hydrate reservoir by depressurization. *Transp. Porous Med.*, 79:443–468, 2009.
- [9] A. Bartel and M. Günther. A multirate w-method for electrical networks in state-space formulation. *Journal of Computational and Applied Mathematics*, 147:411–425, 2002.
- [10] P. Bastian, M. Blatt, A. Dedner, C. Engwer, R. Klöforn, R. Kornhuber, M. Ohlberger, and O. Sander. *A generic grid interface for parallel and adaptive scientific computing*. DFG Research Center MATHEON, 2007.

- [11] J. Bear. *Dynamics of fluids in porous media*. Elsevier, New York, 1972.
- [12] J. Bear and Y. Bachmat. *Introduction to Modeling of Transport Phenomena in Porous Media*. Theory and Applications of Transport in Porous Media. Springer Netherlands, 2012.
- [13] M.A. Biot and D.G. Willis. The elastic coefficients of the theory of consolidation. *J. Appl. Mech.*, 24:594–601, 1957.
- [14] R.H. Brooks and A.T. Corey. *Hydraulic Properties of Porous Media*. Colorado State University Hydrology Papers. Colorado State University, 1964.
- [15] J. Brugada, Y.P. Cheng, K. Soga, and J.C. Santamarina. Discrete element modelling of geomechanical behaviour of methane hydrate soils with pore-filling hydrate distribution. *Granular Matter*, 12(5):517–525, 2010.
- [16] N.T. Burdine. Relative permeability calculations from pore-size distribution data, technical report. Technical report, Petroleum Transactions, AIME, 1953.
- [17] E.B. Burwicz, L.H. Rüpke, and K. Wallmann. Estimation of the global amount of submarine gas hydrates formed via microbial methane formation based on numerical reaction-transport modeling and a novel parameterization of holocene sedimentation. *Geochim. Cosmochim. Acta*, 75:4562–4576, 2011.
- [18] Marwen Chaouachi, Andrzej Falenty, Kathleen Sell, Frieder Enzmann, Michael Kersten, David Haberth-Ajir, and Werner F. Kuhs. Microstructural evolution of gas hydrates in sedimentary matrices observed with synchrotron x-ray computed tomographic microscopy. *Geochemistry, Geophysics, Geosystems*, 16(6):1711–1722, 2015.
- [19] F. Civan. Predictability of porosity and permeability alterations by geochemical and geomechanical rock and fluid interactions. In *SPE 58746*, 2000.
- [20] T.P. Clement, B.S. Hooker, and R.S. Skeen. Macroscopic models for predicting changes in saturated porous media properties caused by microbial growth. *Ground Water*, 34:934–942, 1996.
- [21] E. Constantinescu and A. Sandu. Multirate timestepping methods for hyperbolic conservation laws. *Journal of Scientific Computing*, 33:239–278, 2007.
- [22] E. Constantinescu and A. Sandu. Extrapolated multirate methods for differential equations with multiple time scales. *Journal of Scientific Computing*, 56:28–44, 2013.
- [23] C. David. Japanese test coaxes fire from ice. *Nature*, 496, 409 (April 25, 2013), 2013.
- [24] C. Dawson and R. Kirby. High resolution schemes for conservation laws with locally varying time steps. *SIAM Journal on Scientific Computing*, 22:2256–2281, 2001.

- [25] J.W. Demmel, J.R. Gilbert, and X.S. Li. Superlu users' guide. Technical Report LBNL-44289, Lawrence Berkeley National Laboratory, September 1999. Last update: September 2007.
- [26] Christian Deusner, Nikolaus Bigalke, Elke Kossel, and Matthias Haeckel. Methane production from gas hydrate deposits through injection of supercritical CO_2 . *Energies*, 5(7):2112, 2012.
- [27] C. Engstler and C. Lubich. Multirate extrapolation methods for differential equations with different time scales. *Computing*, 58:173–185, 1997.
- [28] G. Ersland, J. Husebo, A. Graue, B. Baldwin, J.J. Howard, and J.C. Stevens. Measuring gas hydrate formation and exchange with CO_2 in bentheim sandstone using mri tomography. *Chem. Eng. J.*, 158:25–31, 2010.
- [29] F. Esmailzadeh, M. E. Zeighami, and J. Fathi. 1-d modeling of hydrate decomposition in porous media. *International Journal of Chemical, Molecular, Nuclear, Materials and Metallurgical Engineering*, 2(5):45–51, 2008.
- [30] Daniel G. Friend, James F. Ely, and Hepburn Ingham. Thermophysical properties of methane. *Journal of Physical and Chemical Reference Data*, 18(2):583–638, 1989.
- [31] M.J. Gander and L. Halpern. Techniques for locally adaptive time stepping developed over the last two decades domain. In R. Bank, M. Holst, O. Widlund, and J. Xu, editors, *Decomposition Methods in Science and Engineering XX*, volume 91 of *Lecture Notes in Computational Science and Engineering*. Springer, Berlin Heidelberg, 2013.
- [32] C. Gear and D. Wells. Multirate linear multistep methods. *BIT*, 24:484–502, 1984.
- [33] H. Ghiassian and J.L.H. Grozic. Strength behavior of methane hydrate bearing sand in undrained triaxial testing. *Marine and Petroleum Geology*, 43:310 – 319, 2013.
- [34] Itasca Consulting Group. *FLAC3D: Fast Lagrangian Analysis of Continua in 3 Dimensions*. Itasca Consulting Group, Minneapolis, Minnesota, 1997. Version 4,0, edited in 2009.
- [35] M. Günther and P. Rentrop. Multirate row-methods and latency of electric circuits. *Applied Numerical Mathematics*, 13:83–102, 1993.
- [36] M. Hassanizadeh. Derivation of basic equations of mass transport in porous media, part 2: generalized darcy's and fick's laws. *Advances in Water Resources*, 9:207–222, 1986.
- [37] R. Helmig. *Multiphase Flow and Transport Processes in the Subsurface: A Contribution to the Modeling of Hydrosystems*. Springer-Verlag, Berlin, 1997.
- [38] D. M. Himmelblau. Diffusion of dissolved gases in liquids. *Chem. Rev.*, 64(5):527–550, 1964.

- [39] M. Hyodo, Y. Li, J. Yoneda, Y. Nakata, N. Yoshimoto, and A. Nishimura. Effects of dissociation on the shear strength and deformation behavior of methane hydrate-bearing sediments. *Marine and Petroleum Geology*, 51:52 – 62, 2014.
- [40] M. Hyodo, J. Yoneda, N. Yoshimoto, , and Y. Nakata. Mechanical and dissociation properties of methane hydrate-bearing sand in deep seabed. *Soils Found.*, 53(2):299–314, 2013.
- [41] N. Inada and K. Yamamoto. Data report: Pressure coring and shipboard core handling in the nankai project. *Marine and Petroleum Geology*, 2015.
- [42] G. Janicki, S. Schlüter, To. Hennig, H. Lyko, and G. Deerberg. Simulation of methane recovery from gas hydrates combined with storing carbon dioxide as hydrates. *Journal of Geological Research*, 2011, Article ID 462156:1–15, 2011.
- [43] V. A. Kamath and G. D. Holder. Dissociation heat transfer characteristics of methane hydrates. *AIChE J.*, 33:347–350, 1987.
- [44] V.A. Kamath. *Study of heat transfer characteristics during dissociation of gas hydrates in porous media*. PhD thesis, Univ. of Pittsburgh,Pittsburgh, PA, Jan 1984.
- [45] H.C. Kim, P.R. Bishnoi, R.A. Heidemann, and S.S.H. Rizvi. Kinetics of methane hydrate decomposition. *Chemical Engineering Science*, 42(7):1645–1653, 1987.
- [46] S. Kimoto, F. Oka, and T. Fushita. A chemo-thermo-mechanically coupled analysis of ground deformation induced by gas hydrate dissociation. *International Journal of Mechanical Sciences*, 52(2):365–376, 2010.
- [47] A. Klar, K. Soga, and Y.A. NG. Coupled deformation-flow analysis for methane hydrate extraction. *Geotechnique*, 60(10):765–776, 2010.
- [48] O. Kolditz, U.J. Görke, H. Shao, and W. Wang. *Thermo-Hydro-Mechanical-Chemical Processes in Porous Media: Benchmarks and Examples*. Lecture Notes in Computational Science and Engineering. Springer Berlin Heidelberg, 2012.
- [49] M. Kurihara, A. Sato, H. Ouchi, H. Narita, Y. Masuda, T. Saeki, and T. Fujii. Prediction of gas productivity from eastern nankai trough methane-hydrate reservoirs. *SPE125481, SPE Reservoir Eval. Eng.*, 12:477–499, 2009.
- [50] A. Kværnø and P. Rentrop. Low order multirate runge-kutta methods in electric circuit simulation. 1999.
- [51] K.A. Kvenvolden. Gas hydrates, geological perspective and global change. *Rev. Geophys.*, 31:173–187, 1993.
- [52] H. Lee, Y. Seo, Y.-T. Seo, I.L. Moudrakovski, and J.A. Ripmeester. Recovering methane from solid methane hydrate with carbon dioxide. *Angew. Chem. Int. Ed.*, 42:5048–5051, 2003.

- [53] J. Y. Lee, J. Carlos Santamarina, and C. Ruppel. Volume change associated with formation and dissociation of hydrate in sediment. *Geochemistry, Geophysics, Geosystems*, 11(3), 2010. Q03007.
- [54] J.Y. Lee, F.M. Francisca, J.C. Santamarina, and C. Ruppel. Parametric study of the physical properties of hydrate-bearing sand, silt, and clay sediments: 2. small-strain mechanical properties. *Journal of Geophysical Research*, 115(B11):11p, 2010.
- [55] X. Liu and P.B. Flemings. Dynamic multiphase flow model of hydrate formation in marine sediments. *J. Geophys. Res.*, 112, 2007.
- [56] A. Masui, H. Haneda, Y. Ogata, and K. Aoki. Triaxial compression test on submarine sediment containing methane hydrate in deep sea off the coast of japan (in japanese). In *41st Annual Conference*. Jpn. Geotech. Soc., 2006.
- [57] Alexei V. Milkov. Global estimates of hydrate-bound gas in marine sediments: how much is really out there? *Earth-Science Reviews*, 66(3-4):183–197, 2004.
- [58] K. Miyazaki, A. Masui, K. Aoki, Y. Sakamoto, T. Yamaguchi, and S. Okubo. Strain-rate dependence of triaxial compressive strength of artificial methane-hydrate-bearing sediment. *International Journal of Offshore and Polar Engineering*, 20(4):256–264, 2010.
- [59] K. Miyazaki, A. Masui, Y. Sakamoto, K. Aoki, N. Tenma, and T. Yamaguchi. Triaxial compressive properties of artificial methane-hydrate-bearing sediment. *J. Geophys. Res.-Solid Earth*, 116:B06102, 2011.
- [60] G.J. Moridis. Numerical studies of gas production from methane hydrates. *SPE 87330, SPE J.*, 32(8):359–370, 2003.
- [61] G.J. Moridis, T.S. Collett, R. Boswell, M. Kurihara, M.T. Reagan, C. Koh, and E.D. Sloan. Toward production from gas hydrates: Current status, assessment of resources, and simulation-based evaluation of technology and potential. *SPE Reserv. Eval. Eng.*, 12:745–771, 2009.
- [62] G.J. Moridis, T.S. Collett, M. Pooladi-Darvish, S. Hancock, C. Santamarina, R. Boswell, T. Kneafsey, J. Rutqvist, M.B. Kowalsky, and et al. Reagan, M.T. Challenges, uncertainties and issues facing gas production from gas hydrate deposits. *SPE Reserv. Eval. Eng.*, 14:76–112, 2011.
- [63] G.J. Moridis, M. Kowalsky, and K. Pruess. Depressurization-induced gas production from class-i hydrate deposits. *SPE J. Reservoir Evaluation Engng*, 10(5):458–481, 2007.
- [64] G.J. Moridis, M.B. Kowalsky, and K. Pruess. *TOUGH-Fx/HYDRATE v1.0 User's manual: A code for the simulation of system behaviour in hydrate-bearing geologic media*. Earth Sciences Division, Lawrence Berkeley National Laboratory, Berkeley, California, March 2008.

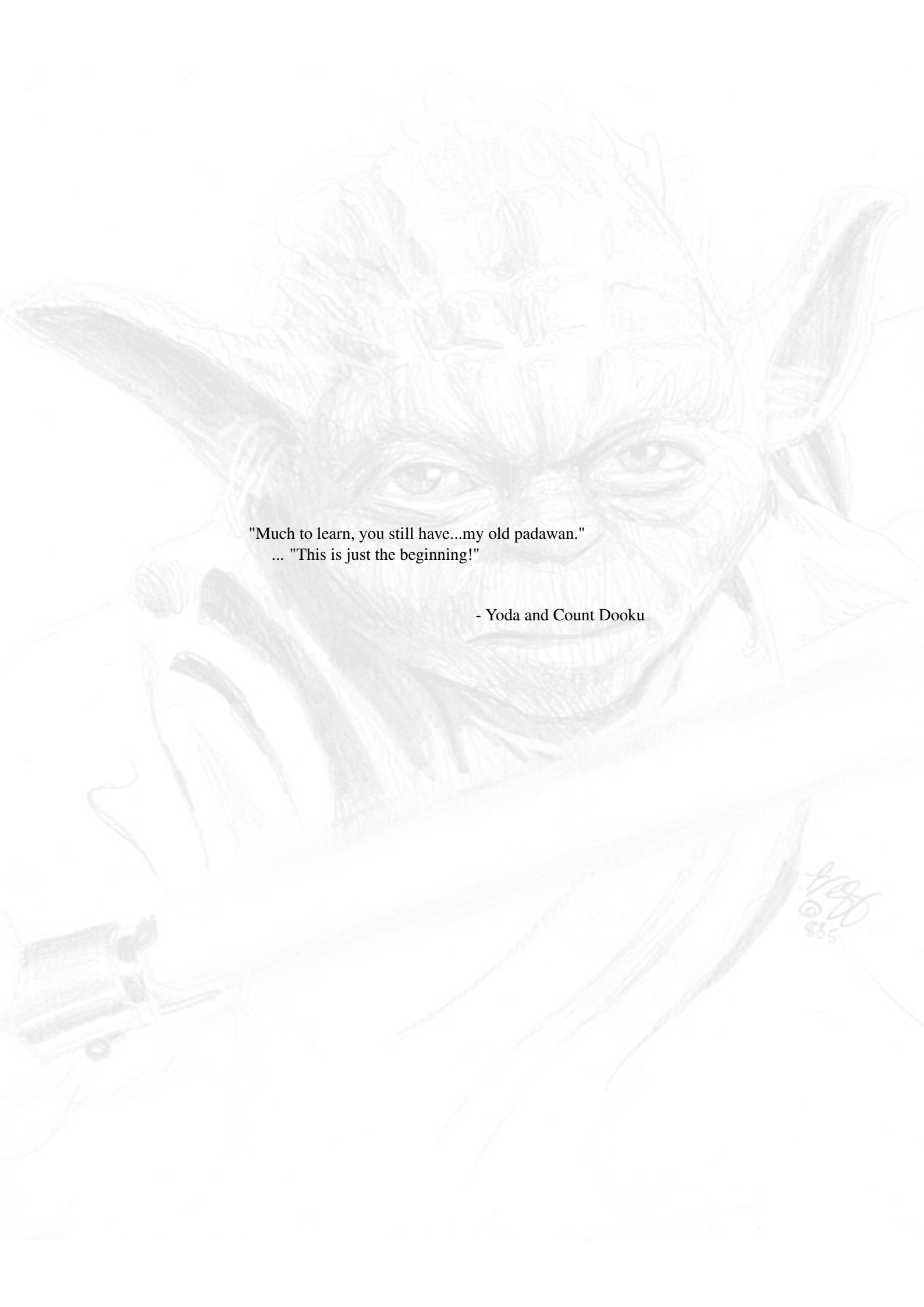
- [65] Y. Mualem. A new model for predicting the hydraulic conductivity of unsaturated porous media. *Water Resour. Res.*, 12(3):513–522, 1976.
- [66] S. Nemat-Nasser, M. Hori, and J.D. Achenbach. *Micromechanics: Overall Properties of Heterogeneous Materials*. North-Holland Series in Applied Mathematics and Mechanics. Elsevier Science, 2013.
- [67] Kirill Nikitin, Kirill Terekhov, and Yuri Vassilevski. A monotone nonlinear finite volume method for diffusion equations and multiphase flows. *Computational Geosciences*, 18(3):311–324, 2013.
- [68] F. Ning, Y. Yu, S. Kjelstrup, T. J. H. Vlught, and K. Glavatskiy. Mechanical properties of clathrate hydrates: status and perspectives. *Energy Environ. Sci.*, 5:6779–6795, 2012.
- [69] S. Osher and R. Sanders. Numerical approximations to nonlinear conservation laws with locally varying time and space grids. *Mathematics of Computation*, 41(164):321–336, 1983.
- [70] M. Pailha and O. Pouliquen. A two-phase flow description of the initiation of underwater granular avalanches. *J. Fluid Mech.*, 633:115–135, 2009.
- [71] Y. Park, D.-Y. Kim, J.-W. Lee, D.-G. Huh, K.-P. Park, J. Lee, and H. Lee. Sequestering carbon dioxide into complex structures of naturally occurring gas hydrates. *Proc. Nat. Acad. Sci. USA*, 103:12690–12694, 2006.
- [72] D. Y. Peng and D. B. Robinson. A new two-constant equation of state. *Industrial and Engineering Chemistry: Fundamentals*, 15:59–64, 1976.
- [73] D.Y. Peng and D.B. Robinson. A new two-constant equation of state. *Industrial & Engineering Chemistry Fundamentals*, 15:59–64, 1976.
- [74] E. Piñero, M. Marquardt, C. Hensen, M. Haeckel, and K. Wallmann. Estimation of the global inventory of methane hydrates in marine sediments using transfer functions. *Biogeosciences*, 10(2):959–975, 2013.
- [75] Jeffrey A. Priest, Angus I. Best, and Christopher R. I. Clayton. A laboratory investigation into the seismic velocities of methane gas hydrate-bearing sand. *Journal of Geophysical Research: Solid Earth*, 110(B4), 2005. B04102.
- [76] Jeffrey A. Priest, Emily V. L. Rees, and Christopher R. I. Clayton. Influence of gas hydrate morphology on the seismic velocities of sands. *Journal of Geophysical Research: Solid Earth*, 114(B11), 2009. B11205.
- [77] Matthew T. Reagan, George J. Moridis, Jeffery N. Johnson, Lehua Pan, Craig M. Freeman, Lehua Pan, Katie L. Boyle, Noel D. Keen, and Jarle Husebo. Field-scale simulation of production from oceanic gas hydrate deposits. *Transport in Porous Media*, 108(1):151–169, 2015.

- [78] J. Rice. Split runge-kutta methods for simultaneous equations. *Journal of Research of the National Institute of Standards and Technology*, 64:151–170, 1960.
- [79] M.L. Rockhold, R.R. Yarwood, M.R. Niemet, P.J. Bottomley, and J.S. Selker. Considerations for modelling bacterial-induced changes in hydraulic properties of variably saturated porous media. *Advances in Water Resources*, 25:477–495, 2002.
- [80] H.M. Roder. Thermal conductivity of methane for temperatures between 110 k and 310 k with pressures upto 70 mpa. *Journal of Thermophysics*, 6(2):119–142, 1985.
- [81] J. Rutqvist, L. Börgesson, M. Chijimatsu, A. Kobayashi, L. Jing, T.S. Nguyen, J. Noorishad, and C.-F. Tsang. Thermohydrmechanics of partially saturated geological media: governing equations and formulation of four finite element models. *International Journal of Rock Mechanics and Mining Sciences*, 38(1):105–127, 2001. Decovalex {II}.
- [82] J. Rutqvist and G.J. Moridis. Development of a numerical simulator for analyzing the geomechanical performance of hydrate-bearing sediments. In *Proceedings of the 42nd U.S. Rock Mechanics Symposium*, 39. American Rock Mechanics Association, ARMA, 2008.
- [83] J. Rutqvist, G.J. Moridis, T. Grover, and T. Collett. Geomechanical response of permafrost-associated hydrate deposits to depressurization-induced gas production. *J. Pet. Sci. Eng.*, 67:1–12, 2009.
- [84] J. Rutqvist, G.J. Moridis, T. Grover, S. Silpngarmert, T.S. Collett, and S.A. Holdich. Coupled multiphase fluid flow and wellbore stability analysis associated with gas production from oceanic hydrate-bearing sediments. *Journal of Petroleum Science and Engineering*, 92-93:65–81, 2012.
- [85] I. Rybak, J. Magiera, R. Helmig, and C. Rohde. Multirate time integration for coupled saturated/unsaturated porous medium and free flow systems. *Computational Geosciences*, 19(2):299–309, 2015.
- [86] R. Sander. Henry’s law constants. In P.J. Linstrom and W.G. Mallard, editors, *NIST Chemistry WebBook*, number 69 in NIST Standard Reference Database. National Institute of Standards and Technology, Gaithersburg MD, 20899, retrieved February 23, 2015.
- [87] J. C. Santamarina and C. Ruppel. The impact of hydrate saturation on the mechanical, electrical, and thermal properties of hydrate-bearing sand, silts, and clay in geophysical characterization of gas hydrates. *Geo-phys. Dev. Ser.*, edited by M. Riedel, C. Willoughby, and S. Chopra, *Soc. of Explor. Geophys.*, Tulsa, Okla, 14:373–384, 2010.
- [88] J.C. Santamarina, S. Dai, M. Terzariol, J. Jang, W.F. Waite, W.J. Winters, J. Nagao, J. Yoneda, Y. Konno, T. Fujii, and K. Suzuki. Hydro-bio-geomechanical properties of hydrate-bearing sediments from nankai trough. *Marine and Petroleum Geology*, pages –, 2015.

- [89] V. Savcenco, W. Hundsdorfer, and J. Verwer. A multirate time stepping strategy for parabolic pde. *Tech. Report MAS-E0516, Centrum voor Wiskunde en Informatica*, 2005.
- [90] V. Savcenco, W. Hundsdorfer, and J. G. Verwer. A multirate time stepping strategy for stiff ordinary differential equations. *BIT*, 47:137–155, 2007.
- [91] V. Savcenco and E. Savcenco. Multirate numerical integration for parabolic pdes. *AIP Conference Proceedings*, 1048:470–473, 2008.
- [92] M. Schlegel, O. Knoth, M. Arnold, and R. Wolke. Implementation of multirate time integration methods for air pollution modelling. *Geoscientific Model Development*, 5(6):1395–1405, 2012.
- [93] D. Schoderbek, H. Farrell, K. Hester, J. Howard, K. Raterman, S. Silpngarmert, K.L. Martin, B. Smith, and P. Klein. Conocophillips gas hydrate production test final technical report. Technical report, ConocoPhillips, October 1, 2008–June 30, 2013.
- [94] E.D. Sloan and C. Koh. *Clathrate Hydrates of Natural Gases, Third Edition*. Chemical Industries. CRC Press, 2007.
- [95] K. Soga, S.L. Lee, M.Y.A. Ng, and A. Klar. Characterisation and engineering properties of methane hydrate soils. In et al. Tan, T.S., editor, *Characterization and Engineering Properties of Natural Soils*, pages 2591–2642. Taylor and Francis, London, 4 edition, 2006.
- [96] Y.C. Song, F. Yu, Y.H. Li, W.G. Liu, and J.F. Zhao. Mechanical property of artificial methane hydrate under triaxial compression. *Journal of Natural Gas Chemistry*, 19:246–250, 2014.
- [97] J.C. Statterry and R.B. Bird. Calculation of diffusion coefficient of dilute gases and of the self diffusion coefficient of dense gases. *AIChE J.*, 4(2):137–142, June 1958.
- [98] L A Stern, S Circone, S H Kirby, and W B Durham. Temperature, pressure, and compositional effects on anomalous or "self" preservation of gas hydrates. *Canadian Journal of Physics*, 81(1-2):271–283, 2003.
- [99] N. Sultan and S. Garziglia. Geomechanical constitutive modelling of gas-hydrate-bearing sediments. In *The 7th International Conference on Gas Hydrates (ICGH 2011)*, 2011.
- [100] F.X. Sun and K.K. Mohanty. Kinetic simulation of methane hydrate formation and dissociation in porous media. *Chemical Engineering Science*, 61:3476–3495, 2006.
- [101] F.X. Sun, K.K. Mohanty, and N. Nanchary. 1-d modelling of hydrate depressurization in porous media. *Transp. Porous Med.*, 58:315–338, 2005.
- [102] H.Z. Tang and G. Warnecke. A class of high resolution schemes for hyperbolic conservation laws and convection-diffusion equations with varying time and space grids. *Journal on Computational Mathematics*, 24:121–140, 2006.

- [103] L.G. Tang, X.S. Li, Z.P. Feng, G. Li, and S.-S. Fan. Control mechanisms for gas hydrate production by depressurization in different scale hydrate reservoirs. *Energy Fuels*, 21(1):227–233, 2007.
- [104] K. Terzaghi. *Erdbaumechanik auf bodenphysikalischer Grundlage*. F. Deuticke, Wien, 1925.
- [105] G.G. Tsytkin. Effect of liquid phase mobility on gas hydrate dissociation in reservoirs. *Izvestiya Akad. Nauk SSSR. Mekh. Zhidkosti i Gaza.*, 4:105–114, 1991.
- [106] A.H. van Zuijlen and H. Bijl. Implicit and explicit higher order time integration schemes for structural dynamics and fluid-structure interaction computations. *Computers & Structures*, 83(2-3):93–105, 2005.
- [107] A. Verhoeven, E.J.W. ter Maten, R.M.M. Mattheij, and B. Tasić. Stability analysis of the bdf slowest first multirate methods. *International Journal of Computer Mathematics*, 84(6):895–923, 2007.
- [108] A. Verruijt. chapter Consolidation of soils. Wiley, Chichester, UK, 2008.
- [109] A. Verruijt. *Theory and problems of poroelasticity*. 2013.
- [110] W. F. Waite, J. C. Santamarina, D. D. Cortes, B. Dugan, D. N. Espinoza, J. Germaine, J. Jang, J. W. Jung, T. J. Kneafsey, H. Shin, K. Soga, W. J. Winters, and T. S. Yun. Physical properties of hydrate-bearing sediments. *Reviews of Geophysics*, 47(4), 2009.
- [111] M.D. White and B.P. McGrail. Stomp-hyd: A new numerical simulator for analysis of methane hydrate production from geologic formations. In JJ Bahk A Reedman, YS Park and N Chaimanee, editors, *Proceedings of 2nd International Symposium on Gas Hydrate Technology*, pages 77–86. CCOP, 2006.
- [112] W.J. Winters, W.F. Waite, D.H. Mason, L.Y. Gilbert, and I.A. Pecher. Methane gas hydrate effect on sediment acoustic and strength properties. *Journal of Petroleum Science and Engineering*, 56(1-3):127–135, 2007. Natural Gas Hydrate / Clathrate The Major Organic Carbon Reserve of the Earth.
- [113] R. Wolke, M. Schlegel, E. Filaus, O. Knoth, and E. Renner. North atlantic treaty organization. In *AIR POLLUTION MODELING AND ITS APPLICATION*, volume 20 of *NATO/CCMS International Technical Meeting on Air Pollution Modeling and Its Application*, pages 475–478. Springer, Dordrecht, London, 2010.
- [114] K. Yamamoto. Japan completes first offshore methane hydrate production test - methane successfully produced from deepwater hydrate layers. fire in the ice: Department of energy, office of fossil energy, national energy technology laboratory. *Methane Hydrate News Letter*, 13(1-2), 2013.
- [115] K. Yamamoto. Overview and introduction: pressure core-sampling and analyses in the 2012-2013 mh21 offshore test of gas production from methane hydrates in the eastern nankai trough. *Marine and Petroleum Geology*, 2015.

- [116] J. Yoneda, A. Masui, Y. Konno, Y. Jin, K. Egawa, M. Kida, T. Ito, J. Nagao, and N. Tenma. Mechanical properties of hydrate-bearing turbidite reservoir in the first gas production test site of the eastern nankai trough. *Marine and Petroleum Geology*, 2015.
- [117] M.H. Yousif. Experimental and theoretical investigation of methane-gas-hydrate dissociation in porous media. *SPE Reserv. Eng.*, pages 69–76, 1991.
- [118] T.S. Yun, G.A. Narsilio, J.C. Santamarina, and C. Ruppel. Instrumented pressure testing chamber for characterizing sediment cores recovered at in situ hydrostatic pressure. *Marine Geology*, 229:285–293, 2006.
- [119] T.S. Yun, J.C. Santamarina, and C. Ruppel. Mechanical properties of sand, silt, and clay containing tetrahydrofuran hydrate. *J. Geophys. Res.*, 112:B04106, 2007.
- [120] S. Zinatbakhsh, B. Markert, and W. Ehlers. Coupled multi-field and multi-rate problems - numerical solution and stability analysis. *PAMM, WILEY-VCH Verlag*, 13(1):241–242, 2013.



"Much to learn, you still have...my old padawan."
... "This is just the beginning!"

- Yoda and Count Dooku

fred
©
885